

Aus dem Institut für Molekular- und Zellbiologie
der Hochschule Mannheim
(Direktor: Prof. Dr. rer. nat. Mathias Hafner)

Microscopic study of RNA-lipoplex-mediated cell targeting
using 2D and 3D models

Inauguraldissertation
zur Erlangung des Doctor scientiarum humanarum (Dr. sc. hum.)
der
Medizinischen Fakultät Mannheim
der Ruprecht-Karls-Universität
zu
Heidelberg

vorgelegt von
Maximilian E. A. Schäfer
aus
Herrenberg
2022

Dekan: Prof. Dr. med. Sergij Goerd
Referent: Prof. Dr. rer. nat. Mathias Hafner

TABLE OF CONTENTS

	Page
ABBREVIATIONS	1
1 INTRODUCTION	4
1.1 RNA, progress towards therapy	4
1.2 Nanoparticles and their therapeutic use	7
1.3 mRNA Lipoplex vaccines	10
1.4 Targeting of nano-drug delivery systems	11
1.5 Potential of lipid nanoparticle-based mRNA drugs in cancer therapy.....	13
1.6 Immune system and its role for drug targeting	14
1.7 Spleen structure and function within the immune system.....	15
1.8 Advanced drug testing models for nanoparticle-based RNA therapeutics..	16
1.9 Fluorescence microscopic 3D tissue analysis	17
1.10 Aims of the project.....	21
2 MATERIAL AND METHODS	22
2.1 Statement on copyright and self-plagiarism	22
2.2 <i>In vitro</i> 2D and 3D cell culture study.....	22
2.2.1 Cell culture and lipoplex nanoparticle treatment.....	22
2.2.2 2D/3D mono- and cocultures.....	23
2.2.3 Live-cell imaging and optical clearing.....	23
2.3 Assembly of lipoplex.....	24
2.4 <i>In vivo</i> lipoplex treatment study	25

2.4.1	Animal treatment and dissection	25
2.4.2	Sectioning and immunofluorescence staining	26
2.4.3	List of antibodies for tissue sections and cell culture.....	27
2.5	LPX 3D <i>in vivo</i> study, optical tissue clearing for light sheet microscopy.....	27
2.5.1	MYOCLEAR.....	27
2.5.2	CUBIC 1/2.....	30
2.5.3	Visikol® HISTO-1/-2™	31
2.5.4	AbScale.....	32
2.5.5	DIMM α	34
2.5.6	List of whole mount labeling reagents	35
2.6	Data Acquisition and Analysis	36
2.6.1	Confocal microscopy.....	36
2.6.2	Light sheet microscopy	36
2.6.3	Image processing.....	36
2.6.4	Colocalization of 2D and 3D Data	37
2.6.5	Ring Analysis	37
2.6.6	Statistical Analysis	37
3	RESULTS.....	39
3.1	Local application <i>in vitro</i> study.....	39
3.1.1	Lipoplex-mediated eGFP expression in 2D mono- and coculture systems	39
3.1.2	3D multicellular culture specificity test.....	41
3.1.3	mRNA product distribution in 3D monocultures.....	43
3.1.4	RNA product distribution in melanoma tri-culture model	46
3.2	Systemic application for <i>in vivo</i> spleen targeting.....	49
3.2.1	2D spleen distribution analysis.....	53

3.2.2	3D tissue clearing for RNA-LPX <i>in vivo</i> targeting in the spleen.....	59
3.2.3	Development of a clearing method to detect mRNA reporters in spleen	61
3.2.4	3D analysis and colocalization of RNA-LPX expression in spleen	66
4	DISCUSSION	70
4.1	Local RNA-LPX application <i>in vitro</i> study	70
4.2	RNA-LPX <i>in vivo</i> treatment targeting antigen presenting cells in lymphoid organs	73
4.2.1	Systemic application for <i>in vivo</i> spleen targeting in 2D	73
4.2.2	3D tissue clearing for RNA-LPX <i>in vivo</i> targeting in the spleen.....	75
4.3	Conclusion	79
5	SUMMARY	80
6	ZUSAMMENFASSUNG.....	82
7	REFERENCES	84
8	PUBLICATIONS	106
9	LEBENS LAUF	107
10	ACKNOWLEDGEMENTS.....	108

ABBREVIATIONS

ADAR	Adenosine deaminase acting ribonucleic acid
ANOVA	Analysis of variance
APC	Antigen presenting cell
ASO	Antisense oligonucleotide
BCZ	B-cell zone
BnP	Blocking and permeabilization
BSA	Bovine albumin serum
Cas	CRISPR associated protein
CD	Cluster of differentiation
CK 14	Cytokeratin 14
CLSM	Confocal laser scanning microscopy
CMOS	Complementary metal-oxide-semiconductor
DC	Dendritic cell
cDC	Conventional dendritic cell
pDC	Plasmacytoid dendritic cell
ddH ₂ O	Double-distilled water
DLS	Digital light sheet system
DLSM	Digital scanned laser light sheet fluorescence microscopy
DNA	Deoxyribonucleic acid
pDNA	Plasmid deoxyribonucleic acid
DMEM	Dulbecco's modified eagle medium
DMSO	Dimethylsulfoxid
DOPE	1,2-Dioleoyl-sn-glycero-3-phosphoethanolamine
DOTMA	1,2-di-O-octadecenyl-3-trimethylammonium propane
eGFP	Enhanced green fluorescent protein
EGFR	Epidermal growth factor receptor
EMCCD	Electron multiplying charge-coupled device
ERP	Enhanced permeability and retention
FBS	Fetal bovine serum
FOLR	Folate receptors
GA	Glutaraldehyde

GLP1R	Glucagon-like peptide-1 receptor
GMP	Good manufacturing practice
IFN	Interferon
ILC	Innate lymphoid cell
IMDM	Iscove's modified dulbecco's medium
IVT	<i>In vitro</i> transcribed
LNP	Lipid nanoparticle
LPX	Lipoplex
LSFM	Light sheet fluorescence microscopy
MDA5	Melanoma differentiation-associated protein 5
MDR	Multidrug resistance
MHC	Major histocompatibility complex
MZ	Marginal zone
MZM	Marginal zone macrophages
M ⁷ G	7-methyl-guanosine
ORF	Open reading frame
OTC	Optical tissue clearing
PALS	Periarteriolar lymphoid sheath
PBS	Phosphate buffered saline
PCR	Polymerase chain reaction
PEG	Polyethylene glycol
PFA	Paraformaldehyde
PLGA	Poly(lactic-co-glycolic acid)
PTwH	Phosphate buffered Tween with heparin
RI	Refractive index
RIG-I	Retinoic acid-inducible gene
RNA	Ribonucleic acid
crRNA	CRISPR ribonucleic acid
mRNA	Messenger ribonucleic acid
miRNA	Micro ribonucleic acid
pegRNA	Prime editing guide ribonucleic acid
rRNA	Ribosomal ribonucleic acid
sgRNA	Single guide ribonucleic acid
siRNA	Small interfering ribonucleic acid

tRNA	transfer ribonucleic acid
RNase	Ribonuclease
ROI	Regions of interest
RP	Red pulp
RP-HPLC	Reversed-phase high-pressure liquid chromatography
RT	Room temperature
SEM	Standard error of the mean
SPIM	Selective plane illumination microscopy
TAA	Tumor-associated antigen
TfR1	Transferrin receptor protein 1
TLR	Toll-like receptor
TSA	Tumor-specific antigen
UTR	Untranslated region
VEGF	Vascular endothelial growth factor
WP	White pulp
2D	Two-dimensional
3D	Three-dimensional

1 INTRODUCTION

1.1 RNA, progress towards therapy

The history of ribonucleic acid (RNA) research began at the end of the 19th century with the discovery of nucleic acids by Friedrich Miescher (Thess et al., 2021). In the middle of the 20th century, Alex Rich and David Davies succeeded in hybridizing two separate RNA strands, the structure of which could be determined using X-ray crystallography (Rich & Davies, 1956). RNA consists of nucleotides, a structural complex of ribose sugars bound to nitrogenous bases and phosphate groups (**Figure 1**). For RNA, a differentiation is made between the four bases adenine, guanine, uracil and cytosine. Three subtypes of RNA are important for protein synthesis in living organisms. Messenger RNA (mRNA), transfer RNA (tRNA), and ribosomal RNA (rRNA). Ribosomal RNA is the foundation of ribosomes. It has several functional groups to bind aminoacyl-tRNAs and link amino acids into polypeptides. The primary function of tRNA is to carry amino acids on its 3' acceptor site to a ribosome complex with the help of aminoacyl-tRNA synthetase (Raina & Ibba, 2014). The messenger RNA is transcribed from the DNA and contains the genetic information for the synthesis of proteins. The freshly formed mRNA is described as pre-mRNA and contains non-coding and coding regions (introns and exons). The splicing of the introns, the joining of the exons, the attachment of the so-called 5' cap (7-methylguanosine) and the polyadenylation of the poly(A) tail at the 3' end transforms the pre-mRNA into mature mRNA. The 5' cap prevents the mRNA from degradation, whereas the 3' poly(A) tail enhances the stability of the mRNA (van Lint et al., 2013; Wang & Farhana, 2022).

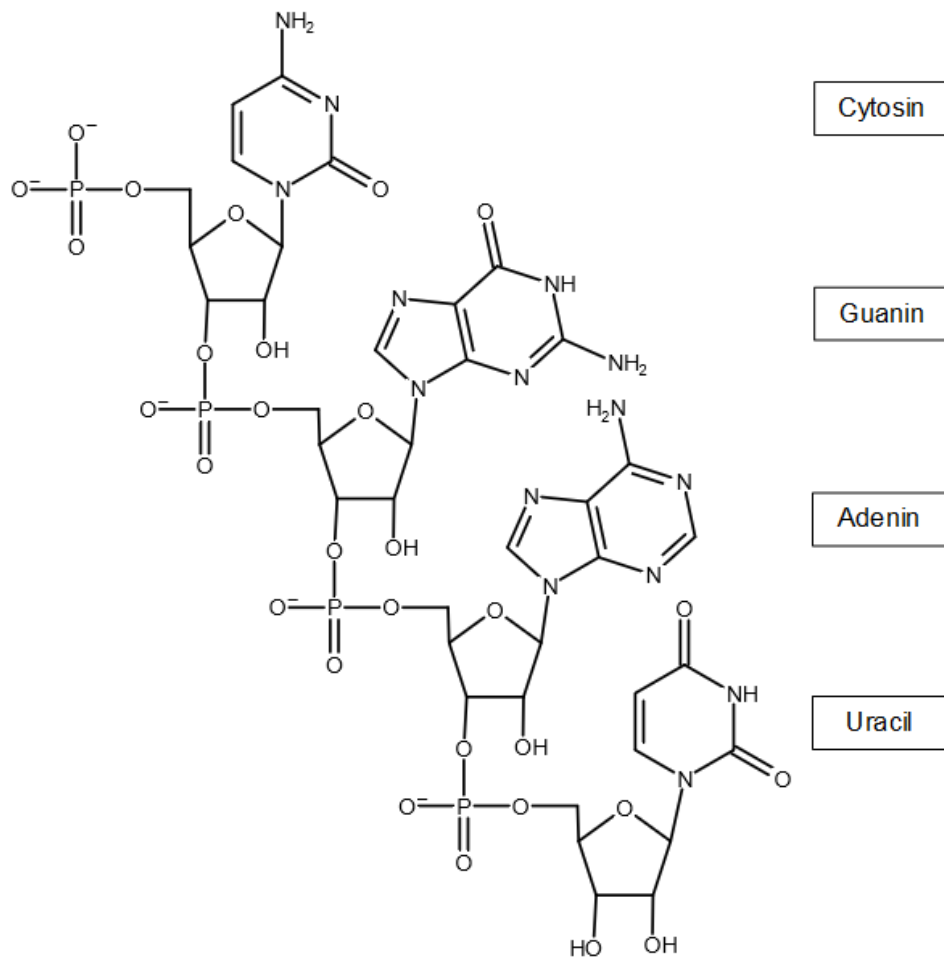


Figure 1: Molecular structure of ribonucleic acid

Since the discovery of catalytic RNA in the 1980s and RNA interference in the 1990s, the understanding of how RNA functions as well as therapies using RNA have continuously developed using different approaches (Burnett & Rossi, 2012; Fire et al., 1998; Guerrier-Takada et al., 1983; Kruger et al., 1982). Among the first classes to be investigated for potential therapeutic application were antisense RNA or antisense oligonucleotides (ASO, inhibitors of mRNA translation), aptamers (RNA that binds proteins and other molecular ligands), RNA decoys, small interfering RNA (siRNA), ribozymes (catalytically active RNA molecules), microRNA (miRNA) and messenger RNA (mRNA) (Burnett & Rossi, 2012; Dorsett & Tuschl, 2004; Melnikova, 2007).

The first RNA-based drug (Macugen) approved by the FDA in 2004 was an anti-vascular endothelial growth factor (VEGF) aptamer used as an anti-angiogenic medicine for the treatment of age-related neovascular macular degeneration (Stein & Castanotto, 2017). The first siRNA-based drug named Patisiran was approved in 2018 for the treatment of hereditary ATTR amyloidosis (Wood, 2018; L.-Y. Zhou et al., 2019).

Today, RNA therapeutics are mainly classified by their mode of action. The following list briefly explains the major features of the current RNA therapeutics in use.

ASOs are synthetic single-stranded DNA/RNA-like molecules that selectively bind to complementary mRNAs or pre-mRNAs (**Figure 2a**). Using a sequence-specific degradation that modulates splicing and blocks polyadenylation, RNA decay can be accelerated, or by disrupting endogenous microRNA (miRNA), which will enhance translation (Seth et al., 2019). Small interfering RNA (siRNA) are double-stranded RNA molecules (usually 21 to 28 base pairs) that serve as mRNA inhibitors to silence the expression of a pathologically overregulated target gene in a disease (**Figure 2a**) (Fellmann & Lowe, 2014).

Due to the targeted base pairing with a target mRNA, the target gene is degraded and ultimately silenced (Bartel, 2004).

Ribozymes are catalytically active RNA molecules that function like enzymes and could selectively slice target RNAs to reduce expression and disrupt subsequent transcription of pathogenic genes (Usman & Blatt, 2000).

RNA aptamers are short, single-stranded oligonucleotide sequences that have a high binding affinity for specific molecules due to their stable 3D structure (Jayasena, 1999). Small activating RNA are short double-stranded noncoding RNA with 2nt overhangs at both sides, similar to siRNAs. saRNAs target gene promoters to mediate transcriptional gene activation also known as RNA activation (L.-Y. Zhou et al., 2018). Messenger RNA (mRNA) also belongs to the group of single-stranded RNA molecules and corresponds to the genetic sequence of a gene which is read by the ribosomes during protein biosynthesis (**Figure 2b**). As a result, gene expression can be directly influenced with mRNA therapy instead of reaching the target indirectly (Wolff et al., 1990; L.-Y. Zhou et al., 2018) (**Figure 2c**).

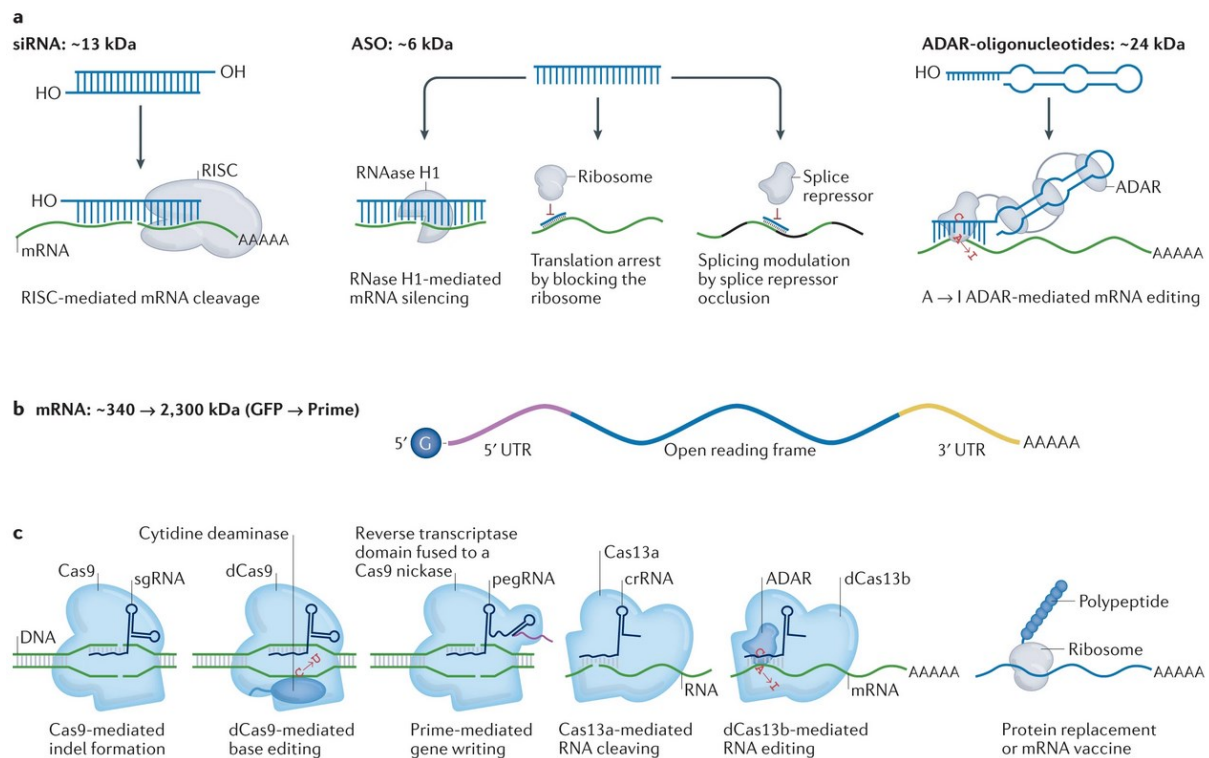


Figure 2: Latest therapeutically used RNAs. Small RNA molecules for use as therapeutic substances (a). Large RNA molecules such as *in vitro* transcribed mRNA (b) or mRNA payloads that encode nucleases that mediate DNA or RNA processing (c). Reproduced from (Paunovska et al., 2022)) with permission from Springer Nature.

Due to the different mechanisms of action, the potential application of RNA therapeutics range from the treatment of degenerative diseases to virally induced diseases and cancer therapy. However, a major challenge with RNA therapeutics is not the mode of action of these different approaches but the inherently unstable, potentially immunogenic nature of RNA *in vivo*. In the organism, the RNA is exposed to increased ribonucleases in the serum and in cells on the way to the target (Burnett & Rossi, 2012). Therefore, a suitable transport system is required that protects the RNA and at the same time enhance the pharmacokinetics as well macrodynamic properties (Sanghvi, 2011; Shukla et al., 2010).

1.2 Nanoparticles and their therapeutic use

The use of RNA as a therapeutic substance makes it possible to selectively influence protein biosynthesis. For many therapies, however, it is of the utmost importance to deliver the RNA to specific tissues or cells in a targeted manner and without degradation (Gupta et al., 2019).

In principle, the nanoparticles used as therapeutic transporters can be classified based on their physical and chemical properties. Particularly important parameters are the size and shape, which mainly limit cell penetration (Bahrami et al., 2017).

The nanoparticles that are currently considered for therapeutic use can be divided into three groups: inorganic, organic and hybrid nanoparticles (Yao et al., 2020).

Inorganic nanoparticles include metallic nanoparticles such as gold and silver as well as non-metallic nanoparticles such as graphene, carbon, semiconductor nanocrystals (quantum dots), silica and magnetic nanoparticles (Khafaji et al., 2019). The inorganic nanoparticles come in various forms, which can significantly change the physical properties. Besides the advantage of a particularly good surface to volume ratio, the inorganic nanoparticles are characterized by easily modifiable surface conjugation chemistry, but with weaknesses in biocompatibility and biodegradability when used as drug carriers (Jiang et al., 2016) (**Figure 3**).

Another group of nanoparticles that can potentially be used for therapeutic purposes are the hybrid materials. Lipid-polymer and liposome-silica hybrid nanoparticles in which the inorganic material forms the core and is surrounded by an organic material are often used (Zhang et al., 2017). In addition, hybrids of e.g., carbon nanotubes with chitosan, or half-shells of metal multilayers (such as manganese and gold) with polylactic-co-glycolic acid are also being investigated (H. Park et al., 2009; Yao et al., 2020) In order to increase stability and to protect the nano-carrier from phagocytosis, approaches in which both organic and inorganic particles are coated with a cell membrane, e.g. silicone particles coated with a leukocyte membrane were also developed (Fang et al., 2018; Parodi et al., 2013).

With these nanoparticles was attempted to combine the advantages of inorganic and organic nanoparticles aiming to improve the biological properties, treatment efficiency, and reducing drug resistance (Mottaghitlab et al., 2019).

For penetration through biological barriers, the surface volume ratio, the size of the particles, and the bioavailability are fundamental (Mitchell et al., 2021). Organic nanoparticles are particularly popular for a drug carrier because there are many different well known materials. However, the biggest advantage are their high biocompatibility and low toxicity due to their organic structure. Mainly lipid-based or polymer-based carriers, dendrimers, or emulsions are investigated and used.

Organic polymer-based nanoparticles usually consist of a multi-monomer structure or polymeric micelles composed of polylactic-co-glycolic acid (PLGA) or amphiphilic

copolymers (Amreddy et al., 2018; Q. Zhou et al., 2018). They are characterized by good biocompatibility, strong enhanced permeability and retention (EPR) effect and good biodegradation (Saneja et al., 2019). Dendrimers are a subgroup of polymer-based nanoparticles. They are characterized by good biocompatibility and a special 3D structure with branches (Sherje et al., 2018).

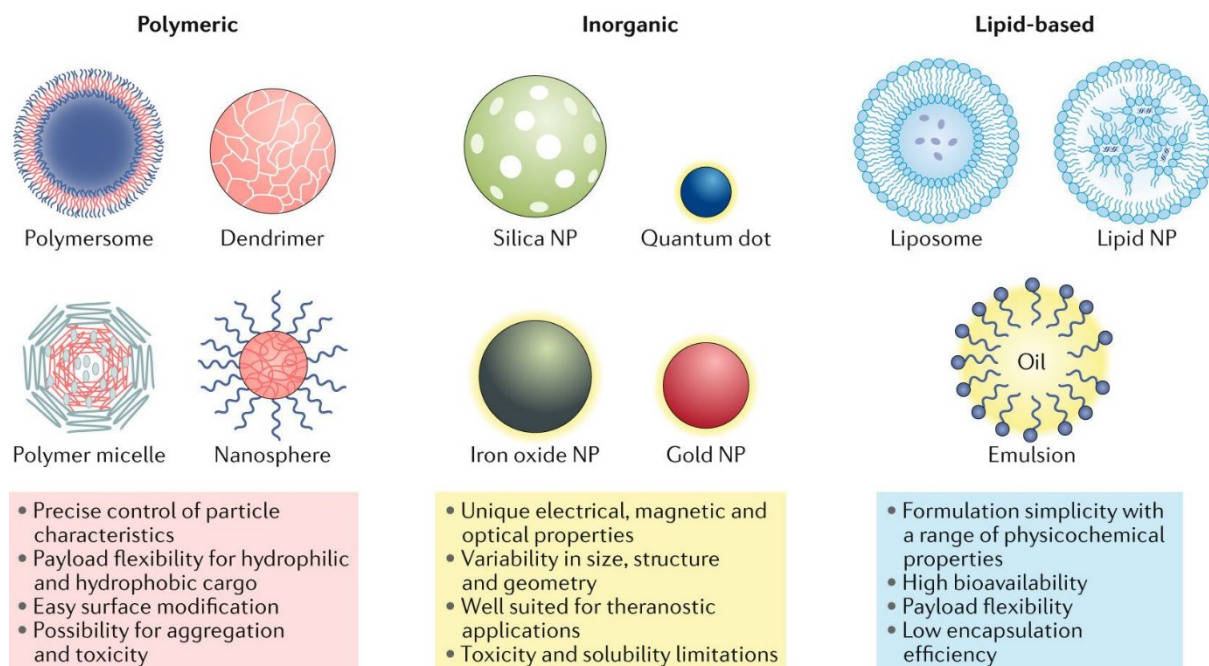


Figure 3: Different nanoparticles and subtypes. The nanoparticles illustrated are the best explored classes and subtypes. Each of the subtypes have different advantages and disadvantages in terms of cargo, delivery and patient response. Reproduced from (Mitchell et al., 2021) with permission from Springer Nature.

Lipid-based nanoparticles are typically made up of phospholipids and can contain unilamellar and multilamellar vesicular structures (Mitchell et al., 2021).

In particular, liposomes, which consist of an outer and an inner lipid layer, can transport both hydrophobic and hydrophilic therapeutics due to this structure (Sarfraz et al., 2018). Liposomes also have many advantages and can mimic biophysical characteristics such as mobility and deformation (Yao et al., 2020). They are characterized by high *in vitro* and *in vivo* stability with rapid uptake by the reticuloendothelial system. They can be produced inexpensively in different sizes, with different lipid compositions, surface charges, surface modifications, or varying number of lamellae (Fonseca-Santos et al., 2015; Mitchell et al., 2021; Sedighi et al., 2019). The transport system plays an elementary role, especially when it comes to cancer therapy and the targeting of certain cells population.

1.3 mRNA Lipoplex vaccines

In recent years it has become evident what an enormous therapy potential the combination of RNA and a nanocarrier offer. However, with all the technical opportunities and benefits that RNA therapy can bring, there are also some challenges.

One of the biggest challenges is to transport the RNA undamaged to its destination. The research results of the last decade reveal that a combination of messenger RNA (mRNA) and lipid-based nanoparticles is very promising. The ability to use *in vitro* transcribed (IVT) mRNA (exogenous delivery mRNA) as a therapeutic vaccine (Mustafa Diken et al., 2017; Kreiter et al., 2010) that is translated into a pharmacologically active product (protein) *in vivo*, was first used in a vaccine against SARS-CoV-2 virus in late 2020 (Polack et al., 2020).

The structure of IVT mRNA mimics that of naturally occurring mRNA in eukaryotic cells, beginning with a 5' cap, an untranslated region (UTR) with a start codon, an open reading frame (ORF) encoding the target protein, followed by another UTR with the stop codon and a poly(A) tail at the 3' end (Sahin et al., 2014). With this structure, a therapeutic effect is possible without the mRNA reaching the nucleus, thereby reducing the risk for mutagenic side effects. The mRNA synthesis is relatively simple, easily scalable even under GMP conditions and the mRNA sequence can be quickly modified if necessary (Sahin et al., 2014; Taina-González & La Fuente, 2022).

There are two main methods used to produce therapeutic mRNA. The first one uses a template with a bacteriophage promoter and generates a 5'-UTR, an open reading frame, a 3'-UTR and a poly-A sequence by PCR.

The second is based on *in vitro* transcription of a linearized pDNA (Plasmid deoxyribonucleic acid) (Taina-González & La Fuente, 2022; Weng et al., 2020). Among the most common chemical modifications of mRNA are changes in the m7G residue that prevent mRNA from being degraded by RNases and from being detected by the immune system (Li & Kiledjian, 2010). Also, the poly-A sequence is often extended, which increases stability by changing the secondary structure of the mRNA (Mauger et al., 2019). Attempts are also being made to improve the stability of the mRNA by substitution with synthetic nucleotides such as N1-methyladenosine or N6-methyladenosine (Taina-González & La Fuente, 2022).

However, the success of the SARS-CoV-2 vaccine could be achieved by transporting the mRNA using lipid nanoparticles. Lipid nanoparticles are particularly well suited as nanocarriers for mRNA due to their size (> 100 nm, high payload capacity) and their versatile modifiability. . In addition to protecting mRNA during systemic circulation, these nanocarriers can efficiently transport mRNA into the cell by fusing with the lipid bilayer of the plasma membrane, thereby transporting mRNA into the cytosol (Hou et al., 2021; Ramachandran et al., 2022). These lipid nanoparticles often consists of structural lipids and cationic ionizable lipids which form complexes with the mRNA (the lipoplex stabilization within LNPs). Structural lipids include polyethylene glycol (PEG) lipids, which shield any residual charge on the surface of the lipid nanoparticles, phospholipids for the bilayer structure, and for further stabilization, cholesterol is most commonly used (Ramachandran et al., 2022).

1.4 Targeting of nano-drug delivery systems

The main tasks of tissue targeting include improving therapeutic potency, increasing specificity and reducing toxicity at the same time (Seth et al., 2019). The targeting of the RNA nanocarriers is important and must be adapted according to the intended use and the disease to be treated. In addition to their use as vaccines against certain viruses, nanocarriers are also very promising for overcoming drug resistance - especially in the context of cancer therapy. A distinction is made between passive and active targeting strategies (Deng et al., 2019).

Passive targeting takes advantage of the difference between normal tissue and the specific properties of the target tissue. In tumor tissue, for example, there is a high proliferation as well as neovascularization, leading to a worse permselectivity of the vascular walls in tumor tissue compared to normal vessels (Carmeliet & Jain, 2000). Thus, certain nanocarriers can penetrate the tumor more easily and, at the same time, the poor lymphatic drainage associated with cancer increases the retention of nanoparticles, which increases the accumulation of nanotherapeutics within the tumor (Yao et al., 2020) (**Figure 4**). A central element of passive targeting is the enhanced permeability and retention (EPR) effect, which is influenced, among other things, by the size and molecular weight of the nanoparticles. Small nanoparticles can penetrate better and large ones are better recognized by the immune system, so the carrier can

be modified as required (Carita et al., 2018; Maeda, 2001; Sykes et al., 2014). The effect of glycolysis in cancer cells, in which the pH value of the tumoral microenvironment is reduced, is also often used for the drug release of pH-sensitive nanocarriers (Lim et al., 2018). Depending on the application, however, these passive targeting methods are inadequate, which is why active targeting methods are often used as well.

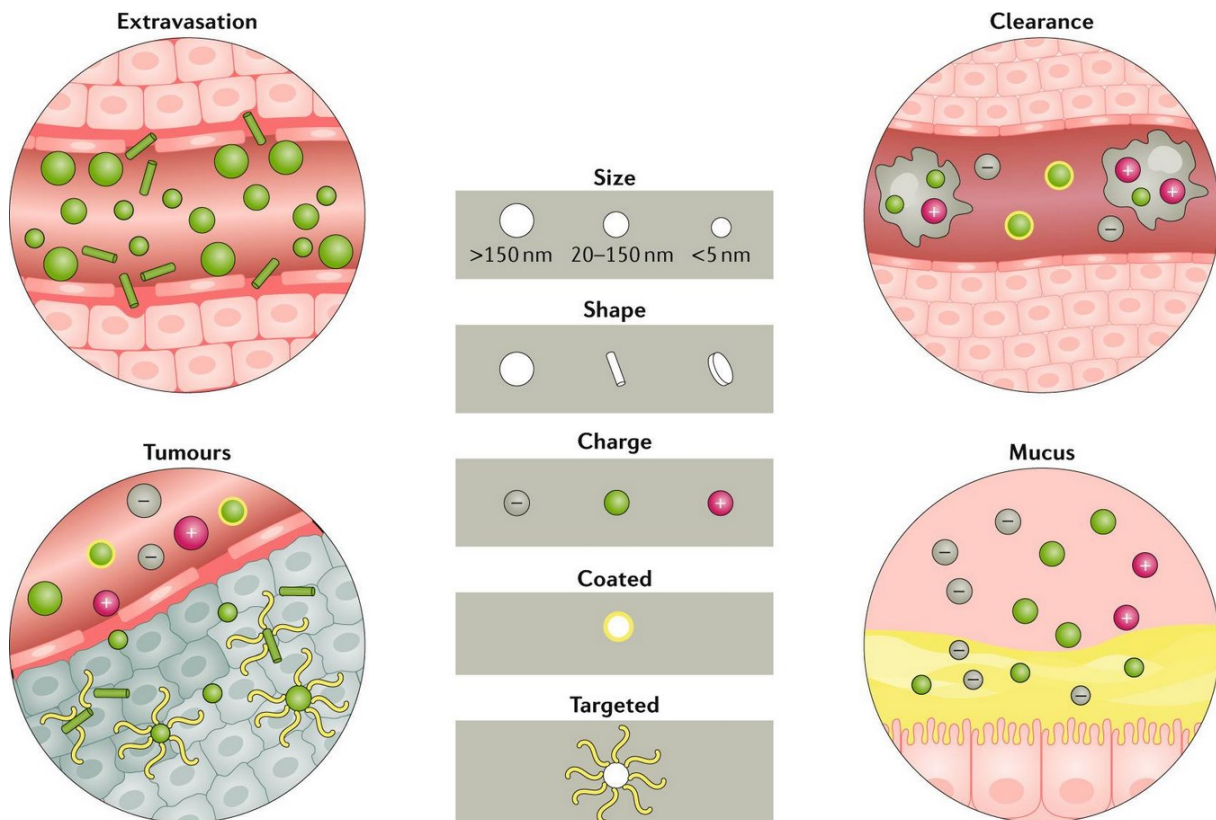


Figure 4: Factors such as shape, size, charge and surface coating allow nanoparticles to interact with different biological barriers. For example, during circulation, spherical and larger nanoparticles can marginate more easily, while rod-shaped nanoparticles extravasate more easily (top left). Uncoated or positively charged nanoparticles are taken up more quickly by macrophages (top right). In the local penetration of tumor tissue, rod-shaped, neutral and targeted nanoparticles proved to be particularly effective (bottom left). Positively charged, smaller and coated nanoparticles are particularly well suited for crossing the mucous membrane (bottom right). Reproduced from (Mitchell et al., 2021) with permission from Springer Nature.

Particularly for cancer therapy, attempts are being made to achieve a high level of specificity through active targeting. In the case of active targeting, the shape and surface of the nanocarriers are mainly adapted in order to reach specific tissues or cells (Blanco et al., 2015). Already in 2014, it was recognized that different shapes such as classical spheres, cylindrical and discoidal accumulate to different extents, e.g. in lungs, liver, spleen and kidneys (Black et al., 2014).

Another technique to increase specificity is surface functionalization of nanocarriers with ligands to target molecules overexpressed on the surface of cancer cells (Kamaly et al., 2012). Almost all molecules found on a cell surface can also be used for targeting. Mostly peptides, monoclonal antibodies, amino acids, carbohydrates and vitamins are used (Danhier et al., 2010). A variety of receptors can be used as target receptors to match the ligands. Glycoproteins (GLP1R), transferrin (TfR1), folate receptors (Folate R) or epidermal growth factor receptor (EGFR) are frequently targeted (Seth et al., 2019; Soe et al., 2019; Yao et al., 2020).

Another technique for targeting is to adjust the charge of a nanocarrier to reach a certain cell population. This technique is of particular interest when the body's own defence mechanisms are used for therapy (Mitchell et al., 2021). The antiviral defence for cancer immunotherapy uses e.g. RNA-lipoplexes, which are lipid-based nanocarriers with specially adjusted net charge to target lymphoid organs with antigen presenting cells (APCs) or other cells of the immune system (Kranz et al., 2016; Sahin et al., 2020).

1.5 Potential of lipid nanoparticle-based mRNA drugs in cancer therapy

Cancer represents a group of diseases in which uncontrolled proliferation, differentiation and increased cell resistance occur primarily due to cell damage or mutations. These disturbances at the cellular level usually lead to abnormal cell masses with increased vascularization which are defined as tumors. Exceptions are hematologic cancers, in which cancer cells grow and spread throughout the vascular and lymphatic systems and bone marrow. Due to the large variety of possible mutated genes, cell types, tissues, their underlying interactions and secondary mutations make cancer a very complex type of disease. Depending on the size, location and degree of development, therapeutic strategies must be adapted (Gaspar et al., 2020; Pérez-Herrero & Fernández-Medarde, 2015). In recent years, the most promising forms of treatment have been surgical resection of the tumor, radiotherapy and, especially in the case of metastatic cancer, chemotherapy (Chabner & Roberts, 2005). Depending on the stage of metastasis, not all metastases can be detected or removed. Treatment with chemotherapeutic agents often involves the risk of drug resistance. In multidrug resistance (MDR), cancer cells are able to resist the toxic effects of the most commonly

used anticancer drugs despite different chemical structures and different modes of action (Liu, 2009).

Therefore, hormones and biological therapies are often investigated in addition to classical chemotherapy (Pérez-Herrero & Fernández-Medarde, 2015). Other very promising and versatile therapeutic approaches include the use of nucleic acid technologies to target cancer-critical genes or to stimulate the human immune system to fight cancer.

In this field, research is focused on the use of plasmid DNA, small-interference RNA, microRNA, antisense oligonucleotides and messenger RNA (Gaspar et al., 2020). The combination of organic lipid nanocarrier and mRNA is particularly versatile. With this approach, the immune system should be used to attack the cancer directly, by means of induced effector memory T cells, the immune system could be able to recognize and prevent metastases (Kranz et al., 2016; Pastor et al., 2018; Sahin et al., 2020).

1.6 Immune system and its role for drug targeting

Utilizing the immune system itself for cancer therapy using targeted stimulation with lipid-based mRNA opens a wide range of new possibilities. In recent years, the approach has evolved from lipid-based mRNA therapeutics to shelf cancer vaccines or even a personalized neoantigen vaccine (Beck et al., 2021). Often, the mRNA therapies target tumor overregulated proteins, tumor-associated or tumor-specific antigens (TAAs or TSAs) (Coulie et al., 2014; Miao et al., 2021). Besides its function of genetic information transfer, mRNA also performs a strong intrinsic adjuvant effect, as exogenous mRNA acts as a natural ligand of endosomal Toll-like receptors (TLRs) 3, 7, 8, retinoic acid-inducible gene 1 (RIG-I), and melanoma differentiation-associated protein 5 (MDA5) in the cytoplasm. In the process, mRNA can also trigger the release of type I interferon (IFN) and pro-inflammatory cytokines (Pastor et al., 2018). The innate immunostimulatory effect of mRNA can be further enhanced by precise targeting using lipoplexes. As part of the innate immune system, antigen presenting cells (APCs) represent an optimal target for the RNA lipoplex. APCs are in close contact with other cells of the immune system and therefore provide the ideal microenvironment for efficient priming and amplification of T cell responses. Hence, CD4 and CD8 positive T cells can also be addressed by lipid nanoparticle-based mRNA therapy (Aarntzen et al., 2012; Beck et al., 2021; Sahin et al., 2017).

In the systemic application it is therefore important to reach the primary and especially the secondary organs of the lymphatic system, such as lymph nodes and spleen, since a strong accumulation of APC is found here. The use of cationic liposomes of lipids DOTMA and DOPE forming colloiddally stable nanoparticulate RNA-LPX with reproducible particle sizes between 200 and 400 nm is investigated for this purpose. The net charge, which is the sum of both positive and negative excess charge, is to be used for cell-specific targeting. Early studies have shown that this technique allows to specifically target different organs of the immune system. Furthermore, it could be demonstrated that also CD11 positive dendritic cells are addressed (Kranz et al., 2016). RNA-lipoplex uptake occurs in APCs mainly through phagocytosis and macropinocytosis or receptor-mediated endocytosis, which are all special forms of Endocytosis (Guevara et al., 2020; Sahay et al., 2010). In addition to the highly specialized dendritic cells (DCs), there are also atypical APCs such as mast cells, innate lymphoid cells (ILCs), basophils and eosinophils. In contrast to the atypical APCs, the so-called professional APC such as dendritic cells, macrophages and B cells constitutively express major histocompatibility complex (MHC) class II structural proteins together with co-stimulatory molecules and pattern recognition receptors (Kambayashi & Laufer, 2014). The MHC I and MHC II complexes enable professional antigen-presenting cells to differentiate immature T cells into mature cytotoxic CD8+ cells or CD4+ cells (T helpers). This antigen presentation enables effective adaptive immune responses and may contribute to immune responses against intracellular as well as extracellular pathogens (Haan et al., 2014; Hillion et al., 2020).

1.7 Spleen structure and function within the immune system

The spleen is the largest organ in the secondary lymphatic system and is responsible for blood filtration in the body. As a filter organ, the spleen is responsible for purifying the blood from pathogens and abnormal cells. At the same time, the spleen is important for the immune system as it is involved in the formation, maturation and storage different kind of lymphocytes. Crucial for the performance of these functions is the architecture of the spleen (Lewis et al., 2019). The structure of the spleen can be separated into the red pulp (RP) and the white pulp (WP) each fulfils specific functions. Between these two areas is the marginal zone (MZ), which in the human organism is also known as the perifollicular zone (Bronte & Pittet, 2013; van Krieken & te Velde, 1988). The red pulp covers a large part of the spleen area, and this is the first site

where aged, infected or dysfunctional red blood cells are filtered out of the blood before it enters the marginal zone. Although the RP does not play a central role in the adaptive immune response, CD 8 finds positive T cells, neutrophils, monocytes, dendritic cells and macrophages (CD11b⁺, F4/80⁺, CD68⁺,CD206⁺) (Nolte et al., 2000). The blood from the terminal arterioles flows into the marginal zone, the interface between RP and WP. The marginal zone contains B cells surrounded two populations of macrophages, the marginal metallophilic macrophages (CD169⁺) and MZ macrophages (MZMs) (Mebius & Kraal, 2005). After the capture of an antigen, the antigen-presenting cells, macrophages and B cells migrate to the WP (Cerutti et al., 2013). The WP can be divided into the T-cell-rich zone, also called the periarteriolar lymphoid sheath (PALS) and the B-cell zone (BCZ, CD45R⁺) similar to those in the lymph nodes. The direct extension of the PALS into the RP is called bridging channel and contains besides T cells also antibody-producing cells (Lewis et al., 2019). The WP also contains antigen-presenting cells such as dendritic cells (MHC-II⁺, CD11C⁺) that can serve as targets for RNA-based therapeutics (Kranz et al., 2016; Nolte et al., 2000). After vaccination, the first exchange between cells from the circulation and various immune cells as well as antigen-presenting cells takes place in the spleen. Therefore, the spleen is a central organ for investigating the effects vaccines on the cells of the immune system.

1.8 Advanced drug testing models for nanoparticle-based RNA therapeutics

To study the abundance of new applications for nanoparticle-based RNA therapeutics, it is necessary to develop appropriate and advanced testing platforms and analyses. The standard platform for *in vitro* analysis of drugs is 2D cell culture because it is inexpensive and reliably reproducible. However, for highly complex tissues and diseases such as cancer, classical 2D models are insufficient because they cannot represent the 3D context of the *in vivo* situation. Especially when it comes to mimicking the pathophysiology of tumors to test the use of radiotherapy or drugs, 2D cell culture models often reveal weaknesses (Dunne et al., 2014). The utilization of multicellular tumor spheroids also enables the microenvironments of the *in vivo* situation of a tumor to be depicted much more realistically (Imamura et al., 2015; Jensen & Teng, 2020).

Over the last few years, a variety of different techniques for generating 3D cell cultures have been developed. The generation of 3D *in vitro* models is possible with various established methods such as hanging drop methods, low attachment plates, magnetic

levitation, spinner bioreactor, rotational bioreactor, microfluidic system, or gel embedding (Lv et al., 2017). Although the complexity of multicellular cell culture models is constantly evolving, the methods are becoming more stable and achieve a high level of reproducibility. Reproducing the microenvironment of a tumor in an *in vitro* model requires the use of cocultures of different cell types. In these cocultures, the different cell types assume tumor-specific functions that reflect the *in vivo* tumor situation much more realistically.

3D tumor cocultures can, depending on the cells used, also reflect the therapeutic effect of drugs on e.g., cellular signalling pathways, cell-cell interactions or cancer-associated fibroblast (Duval et al., 2017). This makes it possible to reproduce the typical structure of a tissue such as the lungs or skin in order to study drug effects on these structures (Esch et al., 2015; Klicks et al., 2019; Schäfer et al., 2021). The 3D structure also has an influence on the proliferation behaviour of the cells, cell targeting, the penetration, and dose effect of a drug. (Paris et al., 2020; Schäfer et al., 2022). In order to analyse these complex systems without neglecting the structural effects, the analysis methods are also extended to the three-dimensional context. Microscopy as a method of analysis is particularly well suited because it can also be used to consider the morphological aspects of a tissue or a study model.

1.9 Fluorescence microscopic 3D tissue analysis

Advanced microscopic techniques allow not only the detection of smallest subcellular components but also the morphological analysis of an entire organ or organisms (Wan et al., 2019). The rapid development of new nanoparticles and RNA-based drugs and the increasingly complex study models require that these is also taken into account in the analysis. In particular for RNA-based therapeutics, where mRNA-encoded reporters can be used for morphological analysis, this represents a high added value. mRNA coding for luciferase or fluorescent proteins (e.g. eGFP) is often applied for this purpose (Dhungel et al., 2019).

Confocal laser scanning microscopy (CLSM) is a well-established microscopic technique for the analysis of such reporter proteins. CLSM is also suitable for the detection of various nanoparticles and can even be used for the analysis of larger studies due to its high scanning speed. However, CLSM is mainly suitable for 2D

imaging due to a low scanning depth, which means that for the analysis of 3D specimens it is normally necessary to prepare thin sections (Mandal et al., 2015). The preparation of tissue sections or the fragmentation of samples for 2D analysis is always a potential source for artifacts (Paknezhad et al., 2020).

Light-sheet microscopy, which had its origins as early as 1902, is now, through continuous further development, a possibility for 3D analysis without the risk of classical artefact formation (Huisken et al., 2004; Siedentopf & Zsigmondy, 1902; Voie et al., 1993). Such systems became of more interest when the first analyses of whole zebrafish embryos were performed using similar techniques, then called Selective Plane Illumination Microscopy (SPIM) (Huisken et al., 2004). Recent developments in light sheet fluorescence microscopy have evolved into light sheet fluorescence microscopy (LSFM), which allows 3D imaging with high spatial resolution, fast image acquisition rate, acceptable signal-to-noise ratio and low phototoxicity (Chatterjee et al., 2018). The technique of light sheet fluorescence microscopy uses a thin excitation light sheet oriented orthogonally to the detection axis to illuminate a single plane of the sample through an illumination objective. The specimen is moved through the light sheet, so images can be scanned level by level over the entire sample and finally 3D image stacks can be generated for quantitative analysis. The detection objective, which is mounted perpendicular to the illumination axis, collects the emitted fluorescence signals. To enable this enormous and parallel acquisition of millions of pixels at high speed, most LSFM systems are equipped with fast area detectors such as electron multiplying charge coupled devices (EMCCD) or metal oxide cameras (CMOS) with very high sensitivity (Chatterjee et al., 2018; Keller et al., 2010; Reynaud et al., 2015; Stelzer & Lindek, 1994).

To further optimise imaging speed and imaging quality especially for large samples, digital scanned laser light sheet fluorescence microscopy (DLSM) was developed (Keller et al., 2008). The principle of this further development is to create a virtual light sheet from a laser scanner and an F-theta lens or double mirror which can then scan even faster through large samples. The imaging is also performed in an orthogonal plane to the specimen, which allows for the use of CLSM in hybrid systems (Köster & Haas, 2015). The digitally generated light sheet is characterised by uniform intensity, which is particularly important for quantitative analyses and the gain of contextual

information in certain areas of the sample that would otherwise be difficult to interpret (Chatterjee et al., 2018; Keller & Stelzer, 2008).

However, to acquire such sets 3D images require a certain degree of transparency of the specimens. This is especially important for large samples or specimens with a high light scattering (Silvestri et al., 2016). The second relevant aspect for optimal 3D microscopic analysis results is to minimise light absorption. In tissues, natural pigments and haemoglobin are mainly responsible for light absorption (Ricci et al., 2022). Light scattering and absorption are therefore dependent on the size and structure of the tissue to be analysed.

For 3D LSM analysis of whole organs or even whole organisms, the samples are chemically treated in a process known as optical tissue clearing (OTC). The aim of OTC is to reduce the refractive index (RI) mismatch and the light absorption within a sample while preserving fluorescent proteins (staining targets), native architecture and information of target molecules (Y.-G. Park et al., 2018; Tainaka et al., 2014; Ueda et al., 2020). The refractive index is a number without dimensions and describes the light bending capacity of a medium. The higher the number, the more the light is bent. Usually OTC methods are based on four fundamental steps: tissue fixation, permeabilization, decolorization and RI matching (Tian et al., 2021). However, biological tissues consist of heterogeneous compounds such as lipids, proteins and also differ considerably in their cellular structure (Johnsen & Widder, 1999; Tuchin, 2006). Therefore, not all clearing methods work equally well for all tissues or tissue types and often need to be adapted or further developed to the study. In recent years, a variety of tissue clearing methods have been developed that are either highly specialised or attempt to be versatile for different tissues. The techniques differ in completely or partially in all of the four fundamental steps (Tian et al., 2021). Fixation is crucial to preserve specimen morphology and prevent degradation. Paraformaldehydes (PFA), acrylamide hydrogel embedding or glutaraldehyde (GA) are commonly used for this purpose. A wide range of reagents such as ethanol, tert-butanol, Triton X-100, Tween, urea, aminoalcohols and saponin can be used for permeabilization. The permeabilization is essential for the success of promoting the diffusion of all other reagents and especially for the staining of specific structures in the tissue. Depending on the tissue to be analysed, decolorization is key in reducing

light absorption. Quadrol, thioglycerol, N-alkylimidazole, ammonium or hydrogen peroxide are often used for this purpose. As a final step to ensure the highest possible clearing capability, the RI must be equilibrated to reduce light scattering. In common protocols, sucrose, aromatic amide, dibenzyl ether, diphenyl ether or polyethylene glycol are used for this (Tian et al., 2021).

The standard protocols can be divided into three main groups. Tissue clearing methods using organic solvents achieve extremely high tissue transparency due to various components that create a high RI in the tissue (Ertürk et al., 2012).

Hydrophilic based methods are relatively simple and safe, but do not provide high clearing capability. The aqueous-based methods can be divided into simple immersion, delipidation and hydration techniques (Weiss et al., 2021).

Hydrogel embedding tissue clearing methods achieve high efficiency in lipid extraction and stabilize proteins in the specimen. However, these methods often use harsh treatments that can lead to the loss of native biomolecules and damage to tissue architecture (Ariel, 2017; Tian et al., 2021).

1.10 Aims of the project

Resistance to therapeutic agents is a problem especially in the case of cancer, bacterial and viral diseases, but also in the long-term treatment of some neurodegenerative diseases (Chen et al., 2022).

The combination of RNA as therapeutic agent and of nanoparticles as their transporters provides a new tool for the treatment of a variety of diseases (Damase et al., 2021). This technology enables various application routes and, in addition to passive targeting, also active targeting (Salahpour Anarjan, 2019). RNA lipoplexes (RNA-LPX), a promising example of such nanoparticles, enable the targeted stimulation of the immune system by specifically addressing and delivering the payload to different antigen-presenting cells (APCs) in lymphoid organs (Kranz et al., 2016).

The primary target of this work was to develop techniques and 3D cell models to analyse RNA-LPX targeting at the cellular level both *in vitro* and *in vivo*.

In a first step, the effect of local application should be investigated in different **in vitro** tumor models in the absence of immune cells. For this purpose, specially developed 3D cell culture models as well as classical 2D mono- and cocultures should be used to investigate the distribution of the RNA reporter signal.

The aim of the second part of the study was to investigate the *in vivo* situation after systemic application of RNA-LPX. For the analyses, the spleen should be used as a central organ of the secondary lymphatic system. Of particular interest for the work was the colocalization between the signal generated by the mRNA reporter and different antigen presenting cells to understand which cell types are targeted by the RNA-LPX.

To obtain a deeper understanding of the distribution of the mRNA reporter signal in the spleen, both classical 2D immunohistological preperates and state-of-the-art 3D preperates should be investigated.

For the investigation of RNA-LPX, new techniques, especially for 3D analyses, should be developed and existing methods further developed to be able to depict the special requirements of these therapeutics.

This provided new insights not only into the cell targeting of RNA lipoplexes, but also into the 2D to 3D and *in vitro* to *in vivo* correlation with respect to RNA reporter signal distribution.

2 MATERIAL AND METHODS

2.1 Statement on copyright and self-plagiarism

The main contents of the methodology described in sections 2.2 - 2.3, the results including figures from section 3.1 and the discussion described in section 4.1 are excerpts from the article published under open access licence by Schäfer, Maximilian E. A.; Keller, Florian; Schumacher, Jens; Haas, Heinrich; Vascotto, Fulvia; Sahin, Ugur et al. (2022): 3D Melanoma Cocultures as Improved Models for Nanoparticle-Mediated Delivery of RNA to Tumors. In: *Cells* 11 (6), p. 1026. DOI: 10.3390/cells11061026.

2.2 *In vitro* 2D and 3D cell culture study

2.2.1 Cell culture and lipoplex nanoparticle treatment

For 2D cultures as well as spheroid cultures, human fibroblast CCD-1137Sk (ATCC® CRL-2703™), human keratinocyte HaCaT (CLS order no. 300493) and human melanoma SK-MEL 28 (CLS order no. 300337) cell lines were used. SK-MEL 28 and HaCaT cells were cultured in Dulbecco's Modified Eagle Medium (DMEM) with high glucose (4.5 g/L), L-Glutamine, and sodium pyruvate (Capricorn), supplemented with 10 % fetal bovine serum (Sigma-Aldrich) and 1 % Penicillin Streptomycin (Capricorn). CCD-1137Sk cells were cultured in Iscove's Modified Dulbecco's Medium (IMDM) with L-Glutamine, supplemented with 10 % fetal bovine serum (Sigma-Aldrich), and 1 % Penicillin Streptomycin (Capricorn). All cells were maintained at 37 °C in 5 % CO₂. On day 0 of each experiment, the cell viability was determined (Vi-CELL XR, trypan blue method, Beckman Coulter). Routinely, cells were tested for mycoplasma using the MycoAlert™ Mycoplasma Detection Kit (Lonza). All 2D and 3D experiments were performed in mono- and cocultures. Transfections with lipoplex nanoparticles (LPX) and RNA encoding eGFP were executed in serum-free medium for a period of 24 h at 37 °C in 5 % CO₂. The LPX concentration range used for transfection of the 2D cultures was based on previous reports and adapted to the different cell lines used in this study (Kranz et al., 2016; Ziller et al., 2018) ; (NCT02410733). As reference concentration for 2D cultures, 1.25 ng/μL of the LPX was used. The 3D cultures required 10 ng/μL LPX for transfection.

2.2.2 2D/3D mono- and cocultures

2D cultures were prepared using 96-well, flat bottom microplates (Greiner). For 2D mono- as well as for 2D cocultures, a total number of 3×10^4 viable cells per well (viability > 96 %) were seeded. In each experiment, the cell number was previously determined using the Vi-CELL XR (Beckman Coulter), trypan blue method. Then, cells were cultured for 24 hours before they were washed (3 x 5 min., PBS, Sigma-Aldrich) and treated with the lipoplexes in serum free medium. Spheroids were generated using 96-well cell repellent plates (Greiner). For 3D monocultures, 1×10^4 viable cells per well (viability > 96 %) were seeded. After seeding, the well plates were centrifuged (5 min., 34 x g) to allow for rapid spheroid formation. Then, spheroids were cultured for 48 hours before treatment with lipoplexes in serum-free medium for a period of 24 h at 37 °C in 5 % CO₂.

Tri-culture spheroids composed of CCD-1137Sk, HaCaT, and SK-MEL 28 cells were prepared in 96 well plates with a cell repellent bottom (Greiner) in two steps: First, 1×10^4 fibroblasts per well (viability > 96 %) were seeded, centrifuged (5 min., 34 x g) and cultured for 72 h. In a second step, HaCaT (1×10^4 cells/well) and SK-MEL 28 cells (2.5×10^3 cells/well, viability > 96 %) were added together and centrifuged (5 min., 34 x g). After coculturing for 48 hours, the spheroids were transferred to serum-free medium and treated with lipoplexes (PBS as negative control) for 24 hours. The creation of the tri-culture was strictly based on (Klicks et al., 2019) and (Schäfer et al., 2021). After the 24 h lipoplex treatment, 3D monocultures and tri-cultures were washed with PBS (3 x 5 min., Carl Roth) and fixed with paraformaldehyde solution (4 % in PBS, RT, 30 min.). For further processing, the spheroids were transferred to 1.5 ml tubes.

2.2.3 Live-cell imaging and optical clearing

Immediately after incubation with lipoplex, 2D mono- and cocultures were washed with PBS and nuclei were stained with DRAQ5 (Invitrogen, diluted 1:1000) for 30 min. at 37 °C. Analysis of eGFP fluorescence in 2D cultures used live-cell confocal microscopy (see below). Analysis of eGFP fluorescence in spheroids was performed in fixed and optically cleared whole mounts. After fixation with paraformaldehyde solution (4 % in PBS, RT, 30 min., Carl Roth) the spheroids were quenched with 0.5 M glycine (Carl Roth) in PBS for 1 h at 37 °C. Next, they were incubated in penetration buffer (0.2 % Triton X-100, 0.3 M glycine, and 20 % DMSO all Carl Roth) in PBS for 30 min. at RT. Then, spheroids were washed with PBS/1 % FBS and incubated in blocking buffer

(0.2 % Triton X-100, 1 % bovine albumin serum (BSA, Carl Roth), 10 % DMSO in PBS) for 2 h at 37°C. Depending on the further readout, samples were either incubated with a primary antibody or the nuclear staining was carried out directly. For primary antibody incubation, mouse anti-cytokeratin 14 (CK14, Merck, MAB3232) was diluted 1:500 in antibody buffer (0.2 % Tween 20, 10 µg/ml Heparin (both Sigma-Aldrich), 1 % BSA, 5 % DMSO in PBS) and then incubated overnight (ON) at 37°C with gentle shaking. Before secondary antibody incubation, samples were washed in washing buffer (0.2 % Tween 20, 10 µg/ml heparin, 1 % BSA), and 5 times for 5 min. at RT. The secondary antibody (A21424, Invitrogen, diluted 1:1000) as well as the nuclear staining (DRAQ5, Invitrogen, diluted 1:1000) were incubated overnight at 37°C with gentle shaking in antibody buffer. Subsequently, samples were washed for 5 times for 5 min. in washing buffer at RT. Finally, samples were washed with ddH₂O and refractive index was adjusted to 1.456 with Dimethyl sulfoxide (Carl Roth), urea (Nacalai Tesque), quadrol (Tokyo Chemical Industry), and sucrose (Nacalai Tesque) glycerol (88 %, Carl Roth) for 48 h at constant RT followed by mounting on 18 well µ-slides (Ibidi) in the same solution. Staining was adapted from (Nürnberg et al., 2020; Williams et al., 2019).

2.3 Assembly of lipoplex

LPX were assembled using protocols as described earlier (Kranz et al., 2016; Rosigkeit et al., 2018). Briefly, mRNA encoding for eGFP, provided in a HEPES/EDTA buffer (10 mM/0.1 mM) was conditioned with a sodium chloride solution to arrive at a sodium chloride concentration of 224 mM and RNA concentration of 0.2 mg/ml (~0.66 mM). The RNA (unmodified) was manufactured at our cooperation partner's laboratory (Mainz, Germany) using internal protocols. The conditioned RNA was mixed one-to-one (v/v) with cationic liposomes consisting of DOTMA (R-1,2-di-O-oleoyl-3-trimethylammonium propane) as a cationic lipid and DOPE (1,2-Dioleoyl-sn-glycero-3-phosphoethanolamine) as helper lipid in a 2:1 molar ratio. Liposomes were manufactured at our cooperation partner's laboratory (Mainz, Germany) with a proprietary protocol derived from the ethanol injection technique. The concentration of the DOTMA in the liposomes was 0.284 mg/ml (~0.42 mM), corresponding to a molar ratio DOTMA/RNA (calculated as one negative charge per nucleotide, 33 Da) of about 0.65. The molar (charge) ratio of DOTMA to RNA inside the LPX was about 1 to 1 (Ziller et al., 2018). Because the LPX were assembled at an excess of RNA regarding charge ratio, an equivalent fraction of free, uncomplexed RNA (~35 %) was present in

the formulations. The LPX were compact globular particles and were characterized by a distinct internal lamellar organization consisting of repeating lipid bilayers where the RNA was inserted into the hydrophilic slab in between the adjacent bilayers (Grabbe et al., 2016; Kranz et al., 2016; Ziller et al., 2018). For quality control, the sizes of the liposomes and the LPX were determined by using dynamic light scattering measurements (Nicomp ZLS Z3000). Concentration of the lipids in the liposome was controlled by RP-HPLC (Agilent Technologies). Size measurements from two independent manufactured batches yielded results as follows:

Table 1: LPX characteristics

	Size (nm)	Polydispersity index
Liposomes	350	0.35
Lipoplex Batch 1	264	0.14
Lipoplex Batch 2	266	0.12

RNA concentrations in the starting phase and the final lipoplex formulation were determined by UV-vis measurements (Nanodrop, Thermo Fisher Scientific), RNA integrity was controlled by capillary electrophoresis measurements (Fragment Analyzer, Agilent Technologies), typical integrity values were >95 %. Prior to the measurements described here, the activity of the LPX was controlled by internal standard cell culture measurements at our cooperation partner's laboratory (Mainz, Germany).

2.4 *In vivo* lipoplex treatment study

2.4.1 Animal treatment and dissection

The treatment and tissue dissection were performed by trained technicians at our cooperation partner's laboratory (Mainz, Germany). For the treatment C57BL/6 female and male mice were used. The treatment was carried out with lipoplex nanoparticle and as control TRP1 was used. To arrange the dissection, the mice were treated 6 hours before tissue isolation with lipoplex nanoparticle and TRP1 as controls. After isolation, the organs were fixed according to the planned experiments.

2.4.2 Sectioning and immunofluorescence staining

For immunostaining of spleen sections, the following steps were implemented. After isolating the corresponding organs, they were either fixed in 4 % (w/v) paraformaldehyde in PBS at 4 °C for 8 h, or directly frozen on dry ice, depending on their further intended use.

After paraformaldehyde fixation the sample was incubated for 16 h at 4 °C in 15 % sucrose (Roth, 4621.1) in PBS, followed by an incubation for 16 h at 4 °C in 30 % sucrose in PBS, before they were embedded in tissue freezing medium (Leica Biosystems). The samples were frozen at –80°C for storage. As standard 10 µm sections were made with a CM-1950 cryostat (Leica Biosystems), the chamber temperature was set to -18°C and the head to -15°C. Also, the fresh frozen samples were cut in the manner described above.

A VT1000 S vibrating blade microtome (Leica Biosystems) was used for thicker cuts (50-100 µm). For this purpose, only 4 % PFA fixed tissue, embedded in low-melting agarose (4 % w/v in ddH₂O) (Roth, 6351.1), were used.

The immunofluorescence staining protocols explained below were used for PFA-fixed, fresh frozen, cryo- and microtome sections.

Only the PFA fixed samples were quenched with quenching buffer (PBS, 0.1 % Triton X-100, 20 % DMSO, 0.3 M glycine) for 2 h at 4 °C before permeabilization.

The sections were permeabilized with 0.4 % Triton X-100 (Roth, 3051.4) in PBS for 10 min. at RT. Before blocking with 2 % BSA (Roth, 8076.3) in PBS for 2 h at 4°C, the sections were washed 3 times for 5 min. with PBS. The primary antibodies were diluted in 2 % BSA and incubated for 3 h at 4°C. All corresponding dilutions of antibodies (primary and secondary) are specified in table 1. Between primary and secondary antibody incubation, sections were washed 3 times for 5 min. with 2 % BSA at RT. The secondary antibodies were also diluted in 2 % BSA and incubated for 3 h at RT protected from light. Subsequently, the respective nuclear staining was implemented, diluted in 2 % BSA and incubated for 30 min. at RT protected from light. Finally, the sections were washed 3 times with PBS and 3 times with ddH₂O each for 5 min. before they were mounted with Mowiol (Carl Roth, 0713.2) on glass slides for microscopic analysis (SP2, SP8, Aperio VERSA, Leica).

2.4.3 List of antibodies for tissue sections and cell culture

Table 2: Antibodies and dilutions for immunofluorescence analysis

Antibody	Company	Number	Dilution
Anti-Firefly Luciferase	Abcam	ab21176	1:500
Anti-GFP	Abcam	ab6673	1:500
Anti-CD169 AF647	Biolegend	142408	1:1000
Anti-CD4 AF594	Biolegend	100446	1:250
Anti-CD45R AF488	BD Biosciences	557669	1:500
Anti-CD11c AF647	Biolegend	117312	1:250
Anti-Cytokeratin 14	Merck	MAB3232	1:500
Anti-S100b	Sigma	HPA015768	1:1000
Anti-Collagen IV	Rockland	600-401-106S	1:500
Draq5	Thermo Fisher Scientific	62251	1:1000
Dapi	Sigma	10236276001	1:500
Phalloidin-TRITC	Sigma	P1951	1:500
Wheat Germ Agglutinin	Biotium	29022	1:500
Anti-Rabbit-AF488	Invitrogen	A21206	1:1000
Anti-Goat-AF488	Invitrogen	A11078	1:1000
Anti -Goat AF546	Invitrogen	A11056	1:1000
Anti-Rabbit AF555	Invitrogen	A32794	1:1000
Anti-Goat 647	Invitrogen	A21447	1:1000
Anti-Mouse-AF647	Invitrogen	A31571	1:1000

2.5 LPX 3D *in vivo* study, optical tissue clearing for light sheet microscopy

Various methods were tested for optical tissue clearing, adapted for the target tissue, spleen and new methods developed for the 3D detection of the lipid nanoparticle-based mRNA drug.

2.5.1 MYOCLEAR

The basic MYOCLEAR protocol (Williams et al., 2019) was adopted and further developed. For whole mount immunostaining of spleen, the following steps were used: After isolating the corresponding organs, they were fixed in 50 ml dark tubes filled with pre-cooled 40ml 4 % acrylamide/0.05 % bisacrylamide + 100 mg 2,2'-[Azobis(1-

methylethyliden)] bis [4,5-dihydro-1H-imidazoldihydrochloride] (Wako Chemical, 27776-21-2) in ddH₂O rolling at 4 °C for 5 days. Before the acrylamide/bisacrylamide gel was polymerized, the samples were gassed with nitrogen for 1 h on ice to remove oxygen within the hydrogel solution. For this purpose a custom made gassing/degassing system was used (Williams et al., 2019). The samples were then degassed using a tissue-gel-hybridization system (LifeCanvas Technologies, EasyGel) for 30 min. at RT with shaking, followed by further incubation for 30 min. at 37 °C. After the initiator had started, the actual polymerization took place at 37 °C for 3.5 h under constant nitrogen flushing (LifeCanvas Technologies, EasyGel). To ensure that the samples were inside the gel during polymerization, custom-built 3D printed sample holders were used. The resulting gel with the sample inside was then removed from the tube using forceps. The samples were carefully removed from the outer gel remnants and then washed for 16 h in 1x PTwH (0.2 % Tween in 1x PBS with 10 µg/ml heparin) at RT on a roller mixer in order to prepare it for the following immunofluorescence staining.

After embedding the samples in acrylamide/bisacrylamide gel and removing the residual hydrogel, the tissue was permeabilized with BnP solution (1x PBS/1x PTwH (0.2 % Tween in 1x PBS with 10 µg/ml heparin)/0.5 % Triton X-100/10 % (vol/vol) DMSO/6 % (vol/vol) BSA) for 5 days at RT on a roller mixer. Thereby, the 3D immunohistochemistry was prepared. The labeling substances were diluted in BnP for 6 days at 37°C using an orbital shaker followed by 4 days of washing with PTwH at RT on an orbital shaker. Secondary antibodies were also diluted in BnP for 6 days at 37°C with constant shaking and protected from light. After secondary antibody incubation the samples were washed for 3 days with PTwH at RT on an orbital shaker and 1 day with ddH₂O under same conditions.

For refractive index (RI) matching the spleen was incubated in a gradient of increasing glycerol concentrations (20 %, 40 %, 60 %, 80 %, 88 % glycerol in ddH₂O). Each concentration was incubated for 1 day at RT. As a last step, the RI was adjusted to 1.457 (ddH₂O in 88 % glycerol) at microscopy room temperature for 2 days. The individual process steps are illustrated in the following Table 8.

Table 3: Adapted MYOCLEAR protocol

Fixation		
Process	Materials	Incubation settings
Immersion perfusion	4 % acrylamide/0.05 % bisacrylamide + VA-044 initiator in ddH ₂ O	5 d at 4 °C on roller mixer
Oxygen removing	Nitrogen fumigation	1 h on ice
Degassing	Tissue-gel-hybridization system	30 min. at RT with shaking
Degassing	Tissue-gel-hybridization system	30 min. at 37 °C with shaking
Polymerization	Tissue-gel-hybridization system with constant nitrogen flushing	3.5 h at 37 °C
Removing outer gel remnants	Forceps	RT
Washing	PTwH	16 h at RT on roller mixer
Permeabilization and decoloration		
Permeabilization and decoloration	BnP	5 d at RT on roller mixer
Immunofluorescence labeling		
Immunofluorescence labeling	BnP + primary antibody	6 d at 37 °C on roller mixer
Washing	PTwH	4 d at RT refresh/2 h on roller mixer
Immunofluorescence labeling	BnP + secondary antibody, nuclear marker and dyes	6 d at 37 °C on roller mixer
Washing	PTwH	3 d at RT refresh/1 h on roller mixer
Washing	ddH ₂ O	1 d at RT refresh/1 h on roller mixer
Refractive index matching		
Gradient perfusion	20 % glycerol in ddH ₂ O	1 d at RT
Gradient perfusion	40 % glycerol in ddH ₂ O	1 d at RT
Gradient perfusion	60 % glycerol in ddH ₂ O	1 d at RT
Gradient perfusion	80 % glycerol in ddH ₂ O	1 d at RT

Gradient perfusion	88 % glycerol in ddH ₂ O	1 d at RT
Final RI matching	88 % glycerol in ddH ₂ O adjusted to 1.457	2 d at microscopy room temperature

2.5.2 CUBIC 1/2

CUBIC 1/2, this clearing method was carried out as described in the published protocol (Susaki et al., 2015; Tainaka et al., 2014). It was based on the “immersion protocol for faster clearing of whole organs” except of the CB-perfusion steps (Susaki et al., 2015). The following chemicals were used for clearing and RI matching: Quadrol 25 % (w/w) final concentration (Tokyo Chemical Industry, T0781), Triton X-100 15 % (w/w) final concentration (Nacalai Tesque Inc., 25987-85) and urea 25 % (w/w) final concentration (Nacalai Tesque Inc., 35904-45) in ddH₂O for reagent-1. Triethanolamine 10 % (w/w) final concentration (Wako Pure Chemical Industries Ltd., 145-05605), urea 25 % (w/w) final concentration (Nacalai Tesque Inc., 35904-45), sucrose 50 % (w/w) final concentration (Nacalai Tesque Inc., 30403-55) and Triton X-100 0.1 % (v/v) (Nacalai Tesque Inc., 25987-85) in ddH₂O for reagent-2. All adjustments are given in the following table. The following processes were carried out in a dark 50 ml tube filled with 40 ml of the respective solution. Only the labeling was performed in 2 ml solution. The dilution of the labeling reagents is shown in Table 8.

Table 4: Adapted cubic 1/2 protocol

Fixation		
Process	Materials	Incubation settings
Immersion perfusion	4 % paraformaldehyde in PBS	16 h at 4 °C on roller mixer
Washing	PBS	1 d at RT refresh/1 h on roller mixer
Permeabilization and decoloration		
Permeabilization and decoloration	Reagent-1	1 d at 37 °C refresh/2 h on roller mixer
Immunofluorescence labeling		
Immunofluorescence labeling	Reagent-1 + primary antibody	3 d at 37 °C on roller mixer

Washing	Reagent-1	1 d at 37 °C refresh/2 h on roller mixer
Immunofluorescence labeling	Reagent-1 + secondary antibody, nuclear marker and dyes	3 d at 37 °C on roller mixer
Washing	PBS	1 d at RT refresh/1 h on roller mixer
Refractive index matching		
Immersion perfusion	1/2-PBS-diluted glycerol	1 d at RT refresh/1 d on roller mixer
Passive perfusion	Reagent-2	3 d at RT refresh/1 d
Final RI matching	88 % glycerol in ddH ₂ O adjusted to 1.457	2 d at microscopy room temperature

2.5.3 Visikol® HISTO-1/-2™

The tissue clearing with Visikol® was carried out according to the manufacturer's instructions. All adjustments are recorded in the following table. The following processes were carried out in a dark 50 ml tube filled with 25 ml of the respective solution. For antibody incubation 2 ml solution were used. The dilution of the labeling reagents is given in Table 8.

Table 5: Applied Visikol® HISTO-1/-2™ protocol

Fixation		
Process	Materials	Incubation settings
Immersion perfusion	4 % paraformaldehyde in PBS	16 h at 4 °C on roller mixer
Washing	PBS	1 d at RT refresh/1 h on roller mixer
Permeabilization and decoloration		
Permeabilization and decoloration	50 % ethanol in PBS	2 h at 4 °C on roller mixer
Permeabilization and decoloration	80 % ethanol in deionized water	2 h at 4 °C on roller mixer

Permeabilization and decoloration	100 % dry ethanol	2 h at 4 °C on roller mixer
Washing	20 % DMSO/ethanol	2 h at 4 °C on roller mixer
Washing	80 % ethanol in deionized water	2 h at 4 °C on roller mixer
Washing	50 % ethanol in PBS	2 h at 4 °C on roller mixer
Washing	PBS	2 h at 4 °C on roller mixer
Washing	2 % Triton™X-100 in PBS	2 h at 4 °C on roller mixer
Immunofluorescence labeling		
Blocking	Visikol® HISTO blocking buffer	6 d at 37 °C on roller mixer
Immunofluorescence labeling	Visikol® HISTO antibody buffer + primary antibody	7 d at 37 °C on roller mixer
Washing	Visikol® HISTO washing buffer	1 d at RT refresh/1 h on roller mixer
Immunofluorescence labeling	Visikol® HISTO antibody buffer + secondary antibody, nuclear dye	7 d at 37 °C on roller mixer
Washing	Visikol® HISTO washing buffer	1 d at 37 °C refresh/1 h on roller mixer
Permeabilization and decoloration	50 % ethanol in PBS	2 h at 4 °C on roller mixer
Permeabilization and decoloration	80 % ethanol in deionized water	2 h at 4 °C on roller mixer
Permeabilization and decoloration	100 % dry ethanol	2 h at 4 °C on roller mixer
Refractive index matching		
Immersion perfusion	Visikol® HISTO-1™	2 d at 37 °C refresh/1 d on roller mixer
Final RI matching	Visikol® HISTO-2™	2 d at 37 °C refresh/1 d

2.5.4 AbScale

This protocol was used as already described by (Hama et al., 2015). Dark 50 ml tubes filled with 40 ml of the respective solution were used for the individual process steps.

The only exception to this is the solutions for the antibodies, which were diluted in 2 ml reagents. The antibody dilutions used for labeling are represented in Table 8. All adjustments are recorded in the following table. The *ScaleS0* solution contained 20 % (w/v) sorbitol, 5 % (w/v) glycerol, 1 mM γ -cyclodextrin, 1 mM methyl- β -cyclodextrin, 3 % (v/v) DMSO, and 1 % N-acetyl-L-hydroxyproline in PBS. The *ScaleA2* solution contained 0.1 % (w/v) Triton X-100, 4 M urea and 10 % (w/v) glycerol in ddH₂O. For *ScaleB4(0)* urea was diluted in ddH₂O to 8 M. The *AbScale* rinse used 2.5 % (w/v) BSA, 0.05 % (w/v) Tween-20 and 0.1 % (w/v) Triton X-100 diluted in PBS. The *AbScale* solution contained 0.1 % (w/v) Triton X-100 and 0.33 M urea diluted in PBS. The refractive index matching solution *ScaleS4* consisted of 15 % (v/v) DMSO, 10 % (w/v) glycerol, 4 M urea and 40 % (w/v) D-sorbitol in ddH₂O.

Table 6: Adapted *AbScale* protocol

Fixation		
Process	Materials	Incubation settings
Immersion perfusion	4 % paraformaldehyde in PBS	16 h at 4 °C on roller mixer
Washing	PBS	1 d at RT refresh/1 h on roller mixer
Adaptation	<i>ScaleS0</i>	12 h at 37 °C with shaking
Permeabilization and decoloration		
Permeabilization	<i>ScaleA2</i>	2 d at 37 °C with shaking
Decoloration	<i>ScaleB4(0)</i>	1 d at 37 °C with shaking
Permeabilization	<i>ScaleA2</i>	1 d at 37 °C with shaking
<i>DeScaling</i>	PBS	8 h at RT refresh/1 h on roller mixer
Immunofluorescence labeling		
Blocking	<i>AbScale</i> rinse	2 d at 37 °C on roller mixer
Immunofluorescence labeling	<i>AbScale</i> + primary antibody	2 d at 37 °C on roller mixer
Washing	<i>AbScale</i>	6 h at RT refresh/2 h on roller mixer
Immunofluorescence labeling	<i>AbScale</i> + secondary antibody, nuclear dye	2 d at 37 °C on roller mixer

Washing	AbScale rinse	10 h at RT refresh/2 h on roller mixer
Refixation	4 % paraformaldehyde in PBS	1 h at RT on roller mixer
Washing	PBS	6 h at RT refresh/2 h on roller mixer
Refractive index matching		
Passive perfusion	ScaleS4	2 d at 37 °C refresh/1 d on roller mixer
Final RI matching	ScaleS4 adjusted to 1.457	2 d at RT refresh/1 d

2.5.5 DIMM α

For the Deep Imaging Mounting Medium (DIMM α) 23 % (v/v) ddH₂O, 12 % (w/v) sucrose, 5 % (v/v) DMSO, 13 % (w/v) urea, 38 % (v/v) glycerol and 9 % (w/v) quadrol were diluted in ddH₂O. The fixation, permeabilization, decoloration and immunofluorescence labeling were applied in an adapted form of the MYOCLEAR protocol. All process steps were carried out in a dark 50 ml tube filled with 40 ml of the respective solution. Only the labeling was performed in 1.5 ml solution. The dilution of the labeling reagents is shown in Table 8.

Table 7: DIMM protocol

Fixation		
Process	Materials	Incubation settings
Passive perfusion	4 % acrylamide/0.05 % bisacrylamide + VA-044 initiator in ddH ₂ O	5 d at 4 °C on roller mixer
Oxygen removing	Nitrogen fumigation	1 h on ice
Degassing	Tissue-gel-hybridization system	1 h at RT with shaking
Degassing	Tissue-gel-hybridization system	30 min. at 37 °C with shaking
Polymerization	Tissue-gel-hybridization system with constant nitrogen flushing	3 h at 37 °C

Removing outer gel remnants	Forceps	RT
Washing	PTwH	16 h at RT on roller mixer
Permeabilization and decoloration		
Blocking and permeabilization	BnP	2 d at RT on roller mixer
Immunofluorescence labeling		
Immunofluorescence labeling	Primary antibody diluted in BnP	5 d at 37 °C on roller mixer
Washing	PTwH	2 d at RT refresh/2 h on roller mixer
Immunofluorescence labeling	Secondary antibody + nuclear dye in BnP	5 d at 37 °C on roller mixer
Washing	PTwH	2 d at RT on roller mixer changing interval start 15 min. doubled up to 6 h
Washing	ddH ₂ O	1 d at RT refresh/2 h on roller mixer
Refractive index matching		
RI matching	DIMM	3 d at RT refresh/7 h on roller mixer

2.5.6 List of whole mount labeling reagents

Table 8: Antibodies and dilutions for 3D immunohistochemistry

Antibody	Company	Number	Dilution
Anti-Firefly Luciferase	Abcam	ab21176	1:250
Anti-GFP	Abcam	ab6673	1:250
Anti-CD169 AF647	Biolegend	142408	1:500
Anti-CD4 AF594	Biolegend	100446	1:250
Anti-CD45R AF488	BD Biosciences	557669	1:250
Anti-CD11c AF647	Biolegend	117312	1:200
Anti-CD31/ PECAM-1	Abcam	AF3628	1:200
Anti-Cytokeratin 14	Merck	MAB3232	1:500
Anti-S100b	Sigma	HPA015768	1:1000
Anti-Collagen IV	Rockland	600-401-106S	1:500

Draq5	Thermo Fisher Scientific	62251	1:1000
Dapi	Sigma	10236276001	1:500
Phalloidin-TRITC	Sigma	P1951	1:500
Wheat Germ Agglutinin	Biotium	29022	1:500
Anti-Rabbit-AF488	Invitrogen	A21206	1:1000
Anti-Goat-AF488	Invitrogen	A11078	1:1000
Anti -Goat AF546	Invitrogen	A11056	1:1000
Anti-Rabbit AF555	Invitrogen	A32794	1:1000
Anti-Goat 647	Invitrogen	A21447	1:1000
Anti-Mouse-AF647	Invitrogen	A31571	1:1000

2.6 Data Acquisition and Analysis

2.6.1 Confocal microscopy

All micrographs were taken with an inverted Leica TCS SP8 confocal microscope (Leica Microsystems CMS, Mannheim) equipped with the latest Leica Application Suite X software. The 2D cell culture images were taken with 5x or 10x Leica objectives. For 3D cell cultures 10x objective was used. The 2D spleen sections were imaged with 10x, 20x or 63x Leica objectives. Images of all samples within an experiment were acquired with the same setting adjusted to the negative control.

2.6.2 Light sheet microscopy

For whole mount 3D scans an inverted Leica TCS SP8 DLS equipped with a Digital Light Sheet objective (Leica Microsystems CMS, Mannheim) and the latest Leica Application Suite X software was used. The samples were imaged with Leica HC APO L10x/0.3 DLS objective in combination with 7.8 mm wide glycerol corrected mirrors. Images of all samples within an experiment depending on the clearing reagents were acquired with the same setting. The exposure settings were always adjusted to the respective control.

2.6.3 Image processing

For illustrative purposes, image brightness and contrast were adjusted and median-filtered (kernel 1 x 1), for both treated and control samples. The figures were composed using Adobe Illustrator (Adobe Systems Software). The 3D cell culture images were

also processed with ImageJ (NIH, Bethesda, MD). The 3D spleen images were processed (mirror fusion, channel merge, background subtraction) with Leica Application Suite X software. Further 3D image processing (deconvolution) was done with the Huygens software (Scientific Volume Imaging B.V., Netherlands).

2.6.4 Colocalization of 2D and 3D Data

All quantitative analyses of nuclei (draq5, dapi), cell type specific markers (α -CK 14, α -S100b, α -collagen IV, α -CD169, α -CD 4, α -CD45R, α -CD11c) and mRNA product (eGFP, luciferase) reporters were performed using ImageJ software (NIH, Bethesda, MD). Therefore, images were threshold adjusted to the control and the mRNA product or cell marker positive area was measured. The results were normalized to the total area of the nuclei. For the colocalization studies, the previously determined Regions of Interest (ROIs) were used and superimposed. The resulting overlap was then linked using the ImageJ software “combine function”. The measurements of the area were made after all non-superimposed areas had been removed using the “clear outside function” of ImageJ.

2.6.5 Ring Analysis

Quantitative image analysis was performed using ImageJ (1.52p). Images of all samples within an experiment were acquired with the same settings. Therefore, the areas of eGFP or CK14 immunofluorescence signal were threshold adjusted to the negative control. Data were normalized to the total area of DRAQ5 signals. For the penetration study, a single optical plane taken in the center of the spheroids was analyzed. For the ring-like region analysis, the ImageJ erosion function was used on the previously generated single optical plane. This allowed four areas (Outer Ring, Mid Ring, Inner Ring and Core) to be defined, which represent the spheroids from the outer border to the core. Using a threshold, the eGFP signal area was determined for each part and normalized to the area of the nuclei signal. The segmentation into rings was intended to better describe the microscopy analysis.

2.6.6 Statistical Analysis

All graphs were created with GraphPad Prism version 8.0.1. The data is presented as mean \pm SEM (standard error of the mean) and statistically analysed using two-way ANOVA (analysis of variance) with post-hoc Tukey test (2D data), one-way ANOVA

with post-hoc Tukey test or Student t-test. P-values are indicated as * ≤ 0.05 , ** ≤ 0.01 , *** ≤ 0.001 , **** ≤ 0.0001 .

3 RESULTS

3.1 Local application *in vitro* study

3.1.1 Lipoplex-mediated eGFP expression in 2D mono- and coculture systems

In a first set of experiments, we focused on the *in vitro* capacity of melanoma and other cell lines to uptake mRNA lipoplex (mRNA-LPX) in 2D and 3D cell culture. The main aim was to compare the mRNA product expression on 2D single cell level and in a 3D multicellular culture model.

For this purpose, we used a previously established cell culture model consisting of fibroblasts, keratinocytes and melanoma cell lines in combination with a lipoplex carrier that transports mRNA encoding for eGFP. In an initial experiment, we examined a concentration window for the cell lines used. For this purpose, CCD-1137Sk, HaCaT and SK-MEL-28 cells were prepared in both mono- and tri-cultures. As reference concentration 0.0125 µg/µL of mRNA-conjugated LPX was applied, which was already used in classic 2D cell culture by Kranz et al. 2016. In order to find a suitable concentration range, concentrations smaller and larger than the reference concentration were tested. The cells were exposed to mRNA-LPX for 24 hours in a light-free environment. Before and after treatment with RNA-LPX, the viability of the cells was tested. For analysis by confocal microscopy, the cells were washed and stained with a nuclear dye. The following **Figure 5(A)** provides representative confocal sections of the samples and shows that eGFP reporter expression was stronger at the lowest concentration (1.25 ng/µl) compared to higher concentrations. With higher concentrations, saturation appeared to set in. A difference in mRNA product expression between the different cell types became visible. Amongst the 2D monocultures, HaCaT cells showed the highest expression. Overall, the tri-cultures showed a higher mRNA product expression compared to any of the monocultures (**Figure 5(B)**).

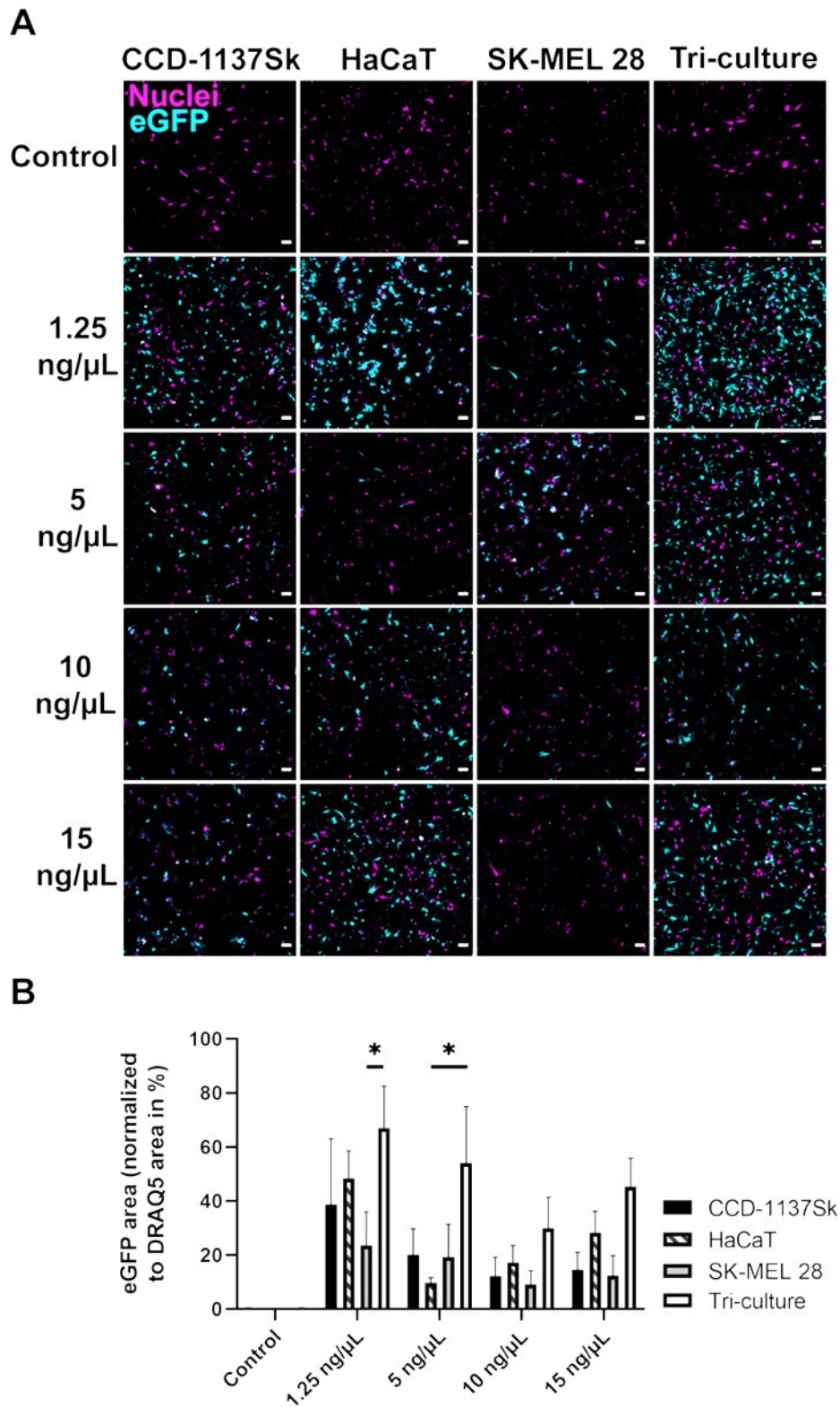


Figure 5: Lipoplex-mediated eGFP translation is enhanced in adherent tri-cultures of CCD-1137Sk, HaCaT, and SK-MEL 28 cells, compared to corresponding monocultures. For each culture condition, a total number of 3×10^4 cells were seeded. The cell number and viability were determined by Vi-CELL XR. After 24 h treatment with varying dosages of eGFP LPX, or with PBS (control). Afterwards, cells were fixed and nuclei were stained. Confocal microscopy was used to visualize nuclei (magenta) and eGFP (cyan). **(A)** Representative confocal multi-tile scans are shown. Scale bars are 100 μm . **(B)** Quantitative analysis of the eGFP area normalized to nuclei signal area as a function of LPX amount added (0 to 15 ng/ μL). Mean + SEM ($n = 3$ independent experiments). Two-way ANOVA with Tukey's multiple comparison post-hoc test ($\alpha = 0.05$). * $p \leq 0.05$. For the illustration, brightness and contrast were adjusted and a median filter (0.3) was used. (Schäfer et al., 2022).

3.1.2 3D multicellular culture specificity test

Based on the results of the 2D mono- and tri-culture data, the first experiments with spheroid monocultures were planned. After the viability test on day 0, for each cell line 1×10^4 cells were seeded in a 96-well plate with cell repellent bottom. Cells were cultured for 48 hours before the spheroids were washed with PBS in order to prepare them for treatment. Based on previous experiments, the 3D cell culture was treated with 10 ng/ μ l. The three different monocultures (CCD-1137Sk, HaCaT, SK-MEL-28) were treated with mRNA-LPX (10 ng/ μ l) and PBS as control for 24 h in serum free medium. **Figure 6(A)** shows an overall mRNA product expression (maximum projection) of the distinct cell lines in treated and untreated conditions. In spheroids, the reporter expression pattern was different for each cell line. While eGFP expression was distributed over the entire spheroids made by SK-MEL 28 cells, the more compact CCD-1137Sk and HaCaT spheroids showed a reporter signal almost exclusively in the periphery. In 3D, the SK-Mel 28 cells showed the highest eGFP positive area with 32.9 % + 2.4 (mean + SEM, n = 3) of the total spheroid area. The eGFP positive area of keratinocytes (HaCaT) was 26.3 % + 11.6 (mean + SEM, n = 3) and 13.3 % + 2.4 (mean + SEM, n = 3) for CCD-1137Sk cells (**Figure 6(B)**).

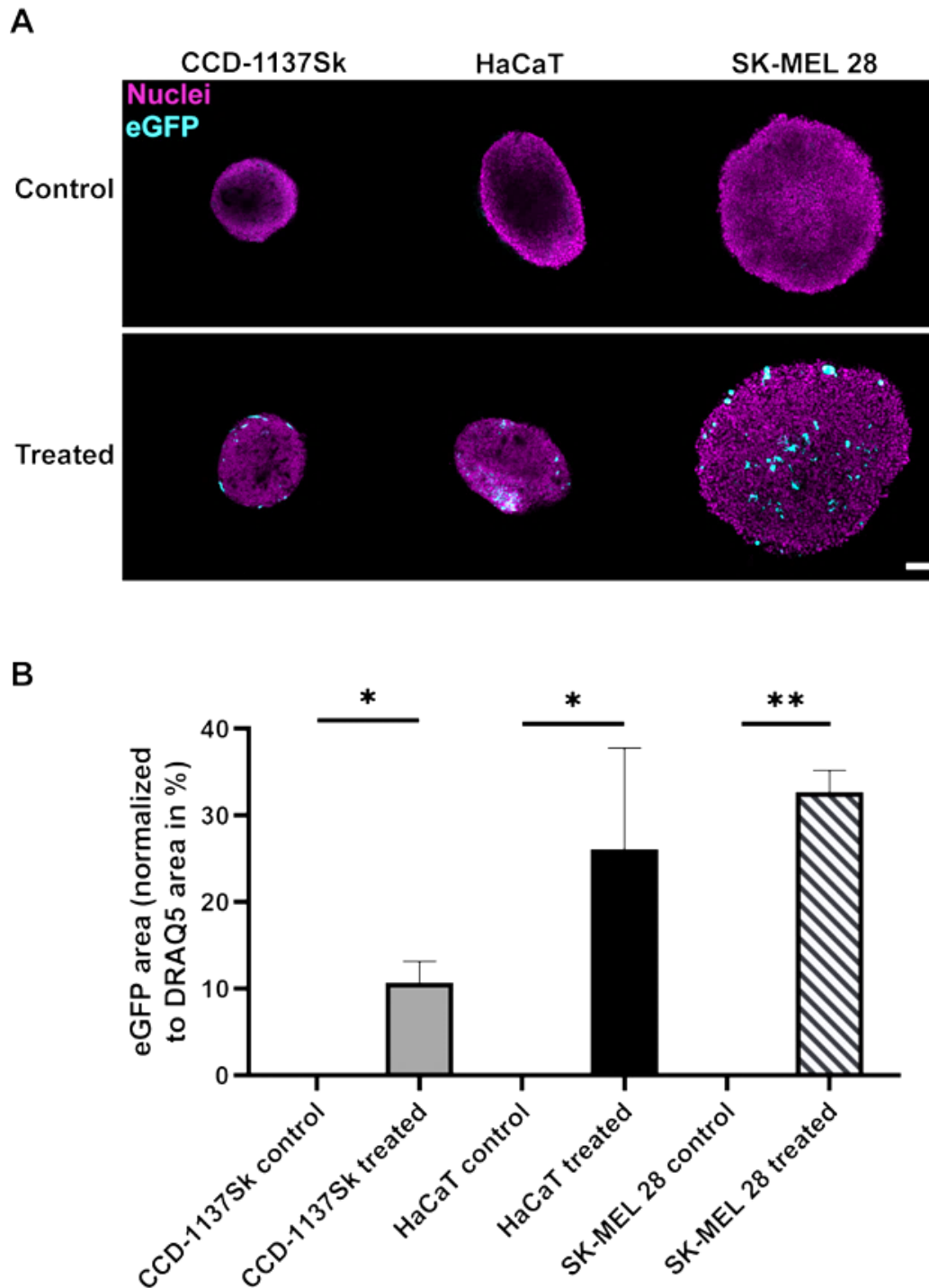


Figure 6: SK-MEL 28 spheroids show high expression of eGFP upon eGFP LPX transfection. For each spheroid, a total of 1×10^4 cells were seeded and transfected with $10 \text{ ng}/\mu\text{L}$ eGFP LPX. PBS was used as a control. Confocal microscopy was used to visualize nuclei (magenta) and eGFP (cyan). (A) Representative single confocal sections through the Z stack of representative spheroids are indicated. Scale bar is $100 \mu\text{m}$. (B) Quantitative analysis of the eGFP area normalized to nuclei signal area are shown. Mean + SEM ($n = 3$ independent experiments, at least 3 spheroids per condition). One-way ANOVA with Tukey's multiple comparison post-hoc test ($\alpha = 0.05$). * $p \leq 0.05$, ** $p \leq 0.01$. For illustration purpose brightness and contrast were adjusted. (Schäfer et al., 2022)

3.1.3 mRNA product distribution in 3D monocultures

In the following experiments, the mRNA product distribution over the entire spheroid was examined. Therefore, confocal optical sections were made at the spheroid center to display a cross section. For further description of the experiments, ring shaped areas were defined on the spheroid's cross section (core area and rings 1-3). The area of the individual rings was adapted to the total size of the spheroid and the cell line, so that the ring areas were comparable between cell lines and test sets. Within each ring the total sizes of the nucleic area and the mRNA reporter (eGFP) area were measured. For the analysis of the individual areas, the middle plane was extracted out of a z-stack. This was then divided into the individual rings. The area of the cell nuclei and the mRNA product signal were determined within each ring. ImageJ was used to create these individual areas and the subsequent analysis. **Figure 7(A)** shows representative images of the midplane from a fibroblast spheroid. It was evident that eGFP expression was largely limited to the outer spheroid ring, while the core remained untransfected. Quantitative analysis showed 10.6 % + 2.2 (mean + SEM, n = 3) eGFP positive area in the first ring, less than 1.5 % + 0.5 (mean + SEM, n = 3) in the second, third ring and no reporter fluorescence in the spheroid core (**Figure 7 (B)**).

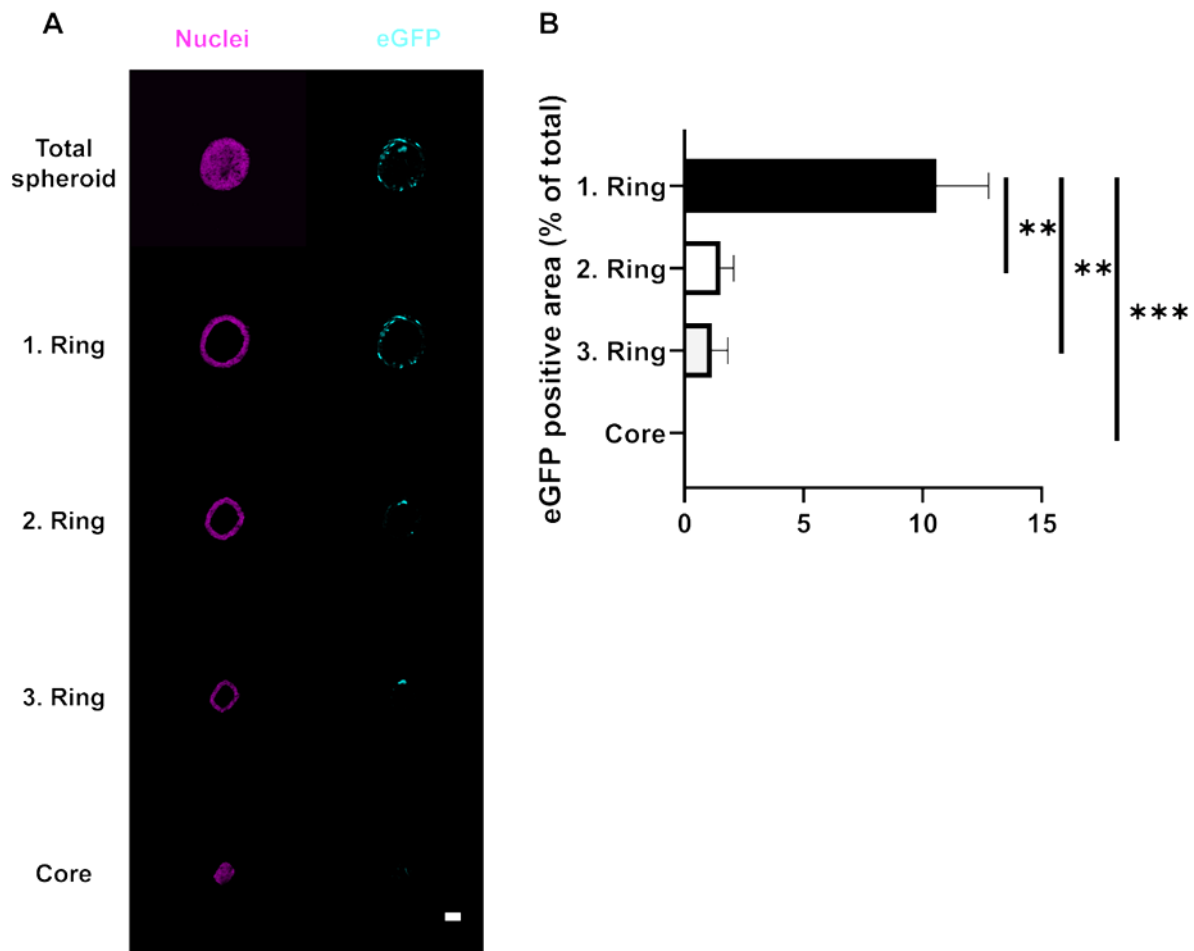


Figure 7: Fibroblasts (CCD-1137Sk) after 24 h treatment with RNA-LPX in serum free medium. Nuclei (draq5, magenta) and endogenous eGFP (mRNA, cyan) were measured (A). A single optical plane out of a z-stack was determined for the graphic evaluation. The total area was divided into 4 parts. Using a threshold, the area of the eGFP signal was determined for each part and normalized to the area of the nuclei signal. This results in values for CCD-1137Sk of 10.6 % + 2.2 in the 1st ring, 1.5 % + 0.5 in the 2nd ring, 1.2 % + 0.6 in the 3rd ring and no penetration into the core (mean + SEM, n = 3 independent experiments, at least 3 spheroids per condition) (B). One-way ANOVA with Tukey's multiple comparison post-hoc test ($\alpha = 0.05$). Imaged with 10 x objective. Scale bar is 100 μm . For illustration purpose brightness and contrast were adjusted. (Schäfer et al., 2022).

In contrast to the fibroblast, in SK-MEL 28 spheroids the eGFP expression was observed in all four areas of the spheroid, and there was even a slight trend towards a larger eGFP positive area in the core (Figure 8(A)). Quantification revealed significantly smaller periphery eGFP-positive area fractions in the SK-MEL 28 spheroid compared to CCD-1137Sk. However, towards the core this picture changed and the SK-MEL 28 showed a significantly larger area of mRNA product positive signal (Figure 8(B)).

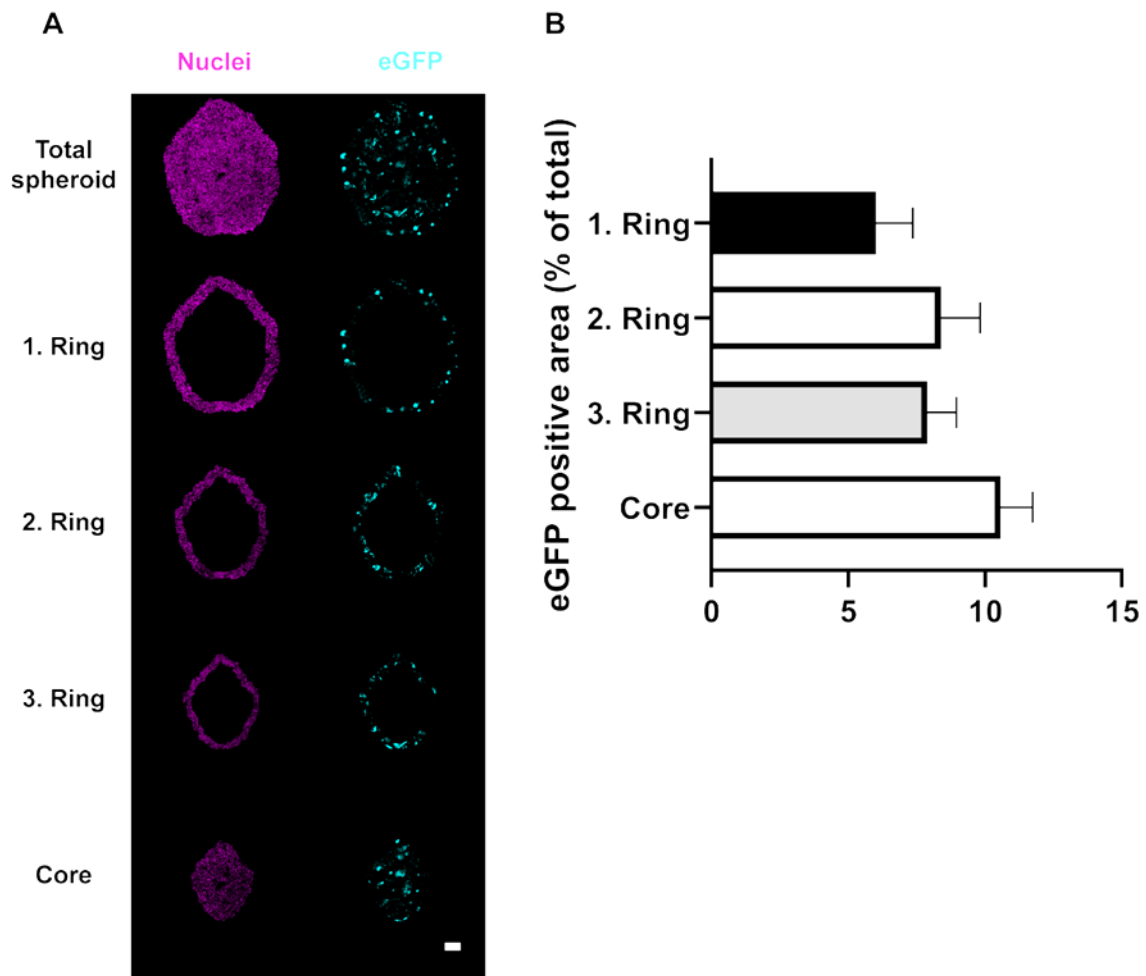


Figure 8: The melanocyte cell line (SK-Mel 28) shows distribution through the entire spheroid. Nuclei were stained with draq5, (magenta) and endogenous eGFP (mRNA product) is displayed in cyan (**A**). Using a threshold, for each ring the area of the eGFP signal was determined and normalized to the area of the nuclei signal. In the first ring 6.0 % + 1.3, 8.4 % + 1.4 in the 2nd ring, 7.9 % + 1.0 in the 3rd ring and 10.6 % + 1.2 (mean + SEM, n = 3 independent experiments, at least 3 spheroids per condition) in the core (**B**). One-way ANOVA with Tukey's multiple comparison post-hoc test ($\alpha = 0.05$). Single optical plane from the center of the z-stack, imaged with 10 x objective. Scale bar is 100 μm . For illustration purpose brightness and contrast were adjusted. (Schäfer et al., 2022).

Finally, spheroids made of HaCaT cells showed a similar reporter distribution as CCD-1137Sk spheroids with a limitation of eGFP fluorescence to the 1. And 2. Ring. As shown in **Figure 9**, eGFP expression was entirely restricted to rings 1 and 2, where it ranged between 12 and 15 % of the total area.

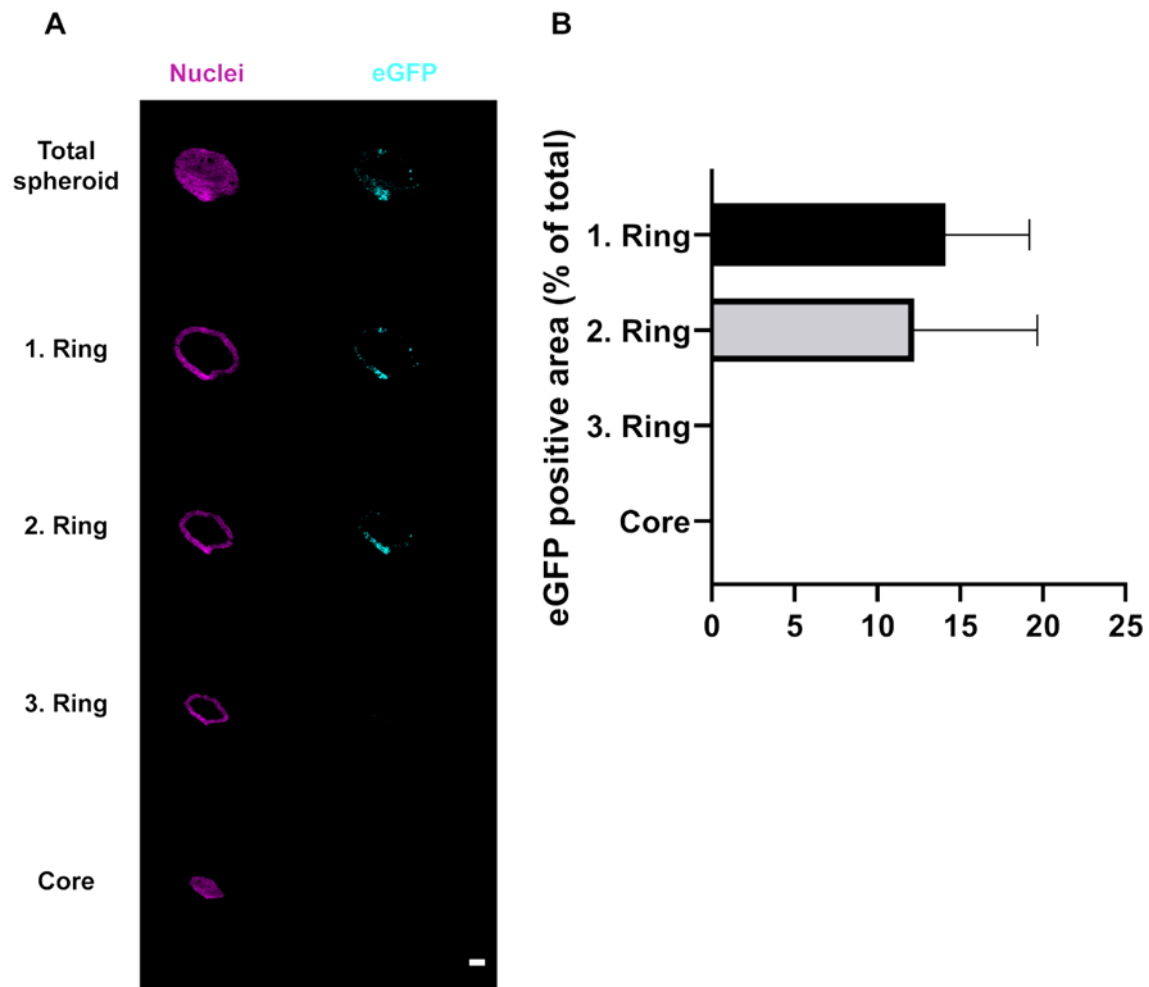


Figure 9: The keratinocyte cell line (HaCat) only indicates an eGFP signal in the peripheral areas. (A) Nuclei were stained with draq5, (magenta) and endogenous eGFP (mRNA, cyan). Using a threshold, for each part of the spheroid the eGFP signal area was determined and normalized to the area of the nuclei signal. The first ring 14.1 % 5.0 and the second ring 12.2 % 7.4 (mean + SEM, n = 3 independent experiments, at least 3 spheroids per condition) eGFP positive area normalized to the nuclei area **(B)** One-way ANOVA with Tukey's multiple comparison post-hoc test ($\alpha = 0.05$). Scale bar is 100 μm . Single optical plane from the center of the z-stack, imaged with 10 x objective. For illustration purpose brightness and contrast were adjusted. (Schäfer et al., 2022).

3.1.4 RNA product distribution in melanoma tri-culture model

The 2D cell culture experiment revealed that the coculture has a larger mRNA product area. Finally, reporter distribution was assessed in tri-culture spheroids.

For the tri-culture (3D coculture), which represents a melanoma model for drug testing (Klicks et al., 2019; Schäfer et al., 2021), a core of fibroblasts was first seeded. Subsequently, the HaCaT and the SK-MEL 28 cells were added to form multilayer tri-culture spheroids. After another 2 days, the tri-cultures were treated with LPX like the monocultures **(Figure 10(A))**. Interestingly, they consistently showed a lower expression of the mRNA than any of the monocultures **(Figure 10(B))**.

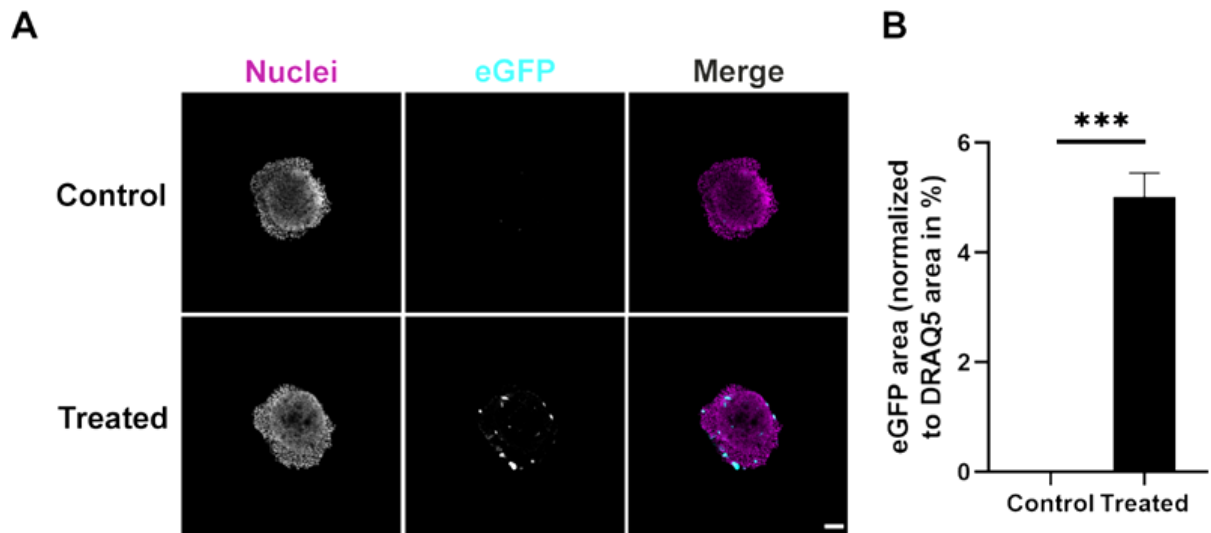


Figure 10: Tri-culture spheroids show reduced expression of the eGFP reporter protein compared to monocultures upon eGFP LPX transfection. For each tri-culture spheroid, identical amounts of cells were used and transfected with 10 ng/ μ L eGFP LPX (treated). PBS was used as a control. Afterwards, spheroids were fixed and stained for nuclei **(A)**. Shown are single confocal sections through the center of representative spheroids. In merge images, nuclei and eGFP are shown in magenta and cyan, respectively. Scale bar, 100 μ m. **(B)** Quantitative analysis of the eGFP area normalized to nuclei area. Mean + SEM ($n = 3$ independent experiments, at least 3 spheroids per condition). T test (two-tailed, unpaired, ($\alpha = 0.05$), *** $p \leq 0.001$). For illustration purpose brightness and contrast were adjusted. (Schäfer et al., 2022).

In order to get a more precise overview of the penetration of the mRNA product into the tri-culture, an analysis was also performed in different areas (rings) like for the monocultures. As depicted in **Figure 11(A)** showing a representative spheroid, the tri-cultures displayed different areas. In addition to a densely packed fibroblast core, also a more loosely structured area was visible towards the outer rim of the spheroid. Indeed, a large part of the mRNA product positive area was located in this first ring. However, the other areas were also mRNA product positive, to a lower degree though (**Figure 11(B)**).

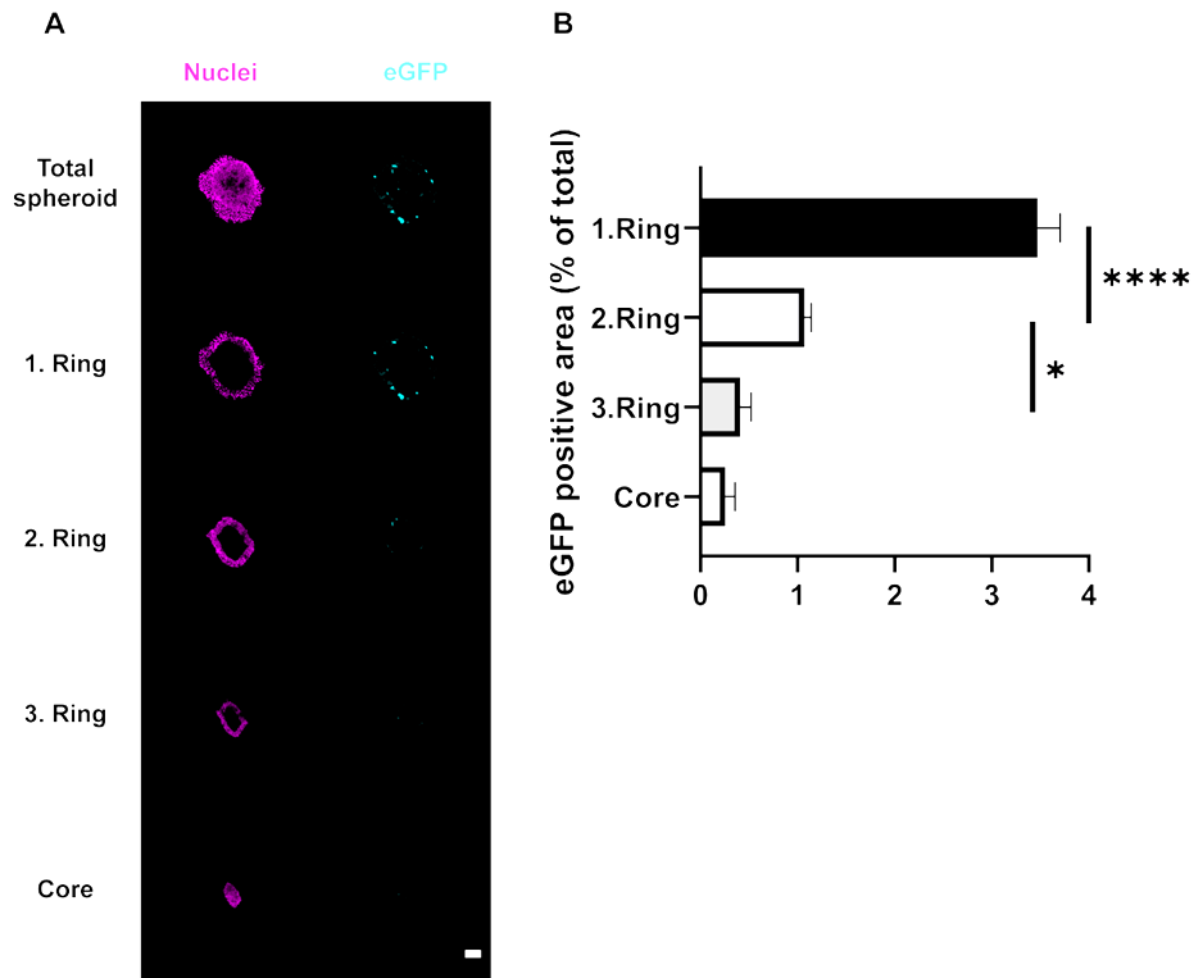


Figure 11: Different mRNA expression in melanoma tri-culture. In total 2.25×10^4 cells were seeded and cultured for 5 days. After 24 h treatment with lipoplex nanoparticle in serum free medium, nuclei (draq5, magenta) and endogenous eGFP (mRNA, cyan) were measured (**A**). Using a threshold, for each part of the spheroid the eGFP signal area was determined and normalized to the area of the nuclei signal. The eGFP expression on the outer layer of the spheroid is $3.5 \% \pm 0.2$ and decrease to the core to $0.2 \% \pm 0.1$ (mean + SEM, $n = 3$ independent experiments, at least 3 spheroids per condition) (**B**). One-way ANOVA with Tukey's multiple comparison post-hoc test ($\alpha = 0.05$). Scale bar is $100 \mu\text{m}$. Single optical plane from the center of the z-stack, imaged with $10 \times$ objective. For illustration purpose brightness and contrast were adjusted. (Schäfer et al., 2022).

To find out, which cell types expressed the reporter, spheroids were co-stained with cytokeratin 14 (CK 14) a marker for keratinocytes. Indeed, CK 14 is found in the basal layer of stratified squamous as well as non-squamous epithelia and present in a large proportion of HaCaT cells. Colocalization analysis revealed that most eGFP positive cells were either CK14 positive or more peripheral (**Figure 12**). From previous work with these tri-cultures (Klicks et al., 2019; Schäfer et al., 2021), it can therefore be inferred that the most reporter positive cells in the tri-cultures were either HaCaT or SK-MEL 28.

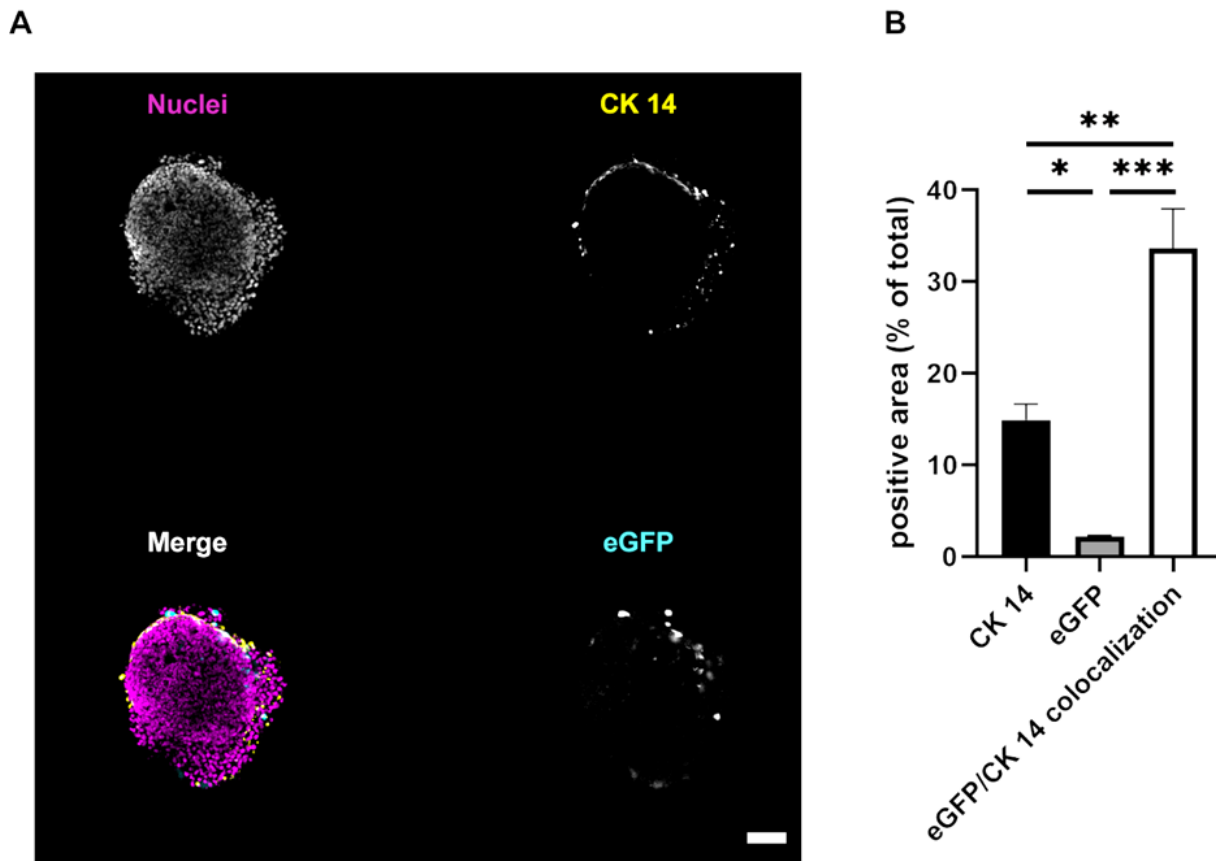


Figure 12: Colocalization of mRNA product (eGFP) and CK 14 (basal keratinocytes). In total 2.25×10^4 cells were seeded and cultured for 5 days. After 24 h treatment with lipoplex nanoparticle in serum free medium, nuclei (draq5, magenta), CK 14 (yellow) and endogenous eGFP (mRNA, cyan) were measured (**A**). The eGFP and CK 14 positive area was threshold adjusted to the control. The resulting eGFP or CK 14 area was normalized to the nuclei or CK 14 area. The overall CK 14 expression is $14.9\% \pm 1.7$ and eGFP $2.2\% \pm 0.1$ (mean + SEM, $n = 3$ independent experiments, at least 3 spheroids per condition). Altogether $33.6\% \pm 4.3$ (mean + SEM) of the eGFP positive area is also positive for CK 14 (**B**). One-way ANOVA with Tukey's multiple comparison post-hoc test ($\alpha = 0.05$). Scale bar is $100 \mu\text{m}$. Single optical plane from the center of the z-stack, imaged with $10 \times$ objective. For illustration purpose brightness and contrast were adjusted. (Schäfer et al., 2022).

3.2 Systemic application for *in vivo* spleen targeting

Besides local application, mRNA-LPX is often applied systemically to target cells of the immune system. The targeting of mRNA-LPX can be studied particularly well in an *in vivo* study. The spleen is an important organ of the secondary lymphoid system. An exchange between different immune cells and pathogens can take place through the blood vessels. In the context of intravenous administration of RNA-LPX, antigen-presenting cells are of particular interest. When selecting the markers, care was taken to depict dendritic cells and macrophages that represent a potential target for LPX vaccines. For the *in vivo* study, adult (f/m) C57BL/6 mice were systemically injected with RNA-LPX. After 6 hours, the spleen was isolated and directly frozen on dry ice. The following figure shows a cryosection of mouse spleen stained with anti CD169 to

depict macrophages (magenta), which are mainly found in the metallophilic marginal zone of the spleen which is a part of the white pulp and surrounds the primary follicle. In addition to the cell nuclei, which are shown in blue, blood vessels are visible (green) (**Figure 13**). In the middle, the large trabecular vessels and the ramifications from the red pulp towards the white pulp can be seen.

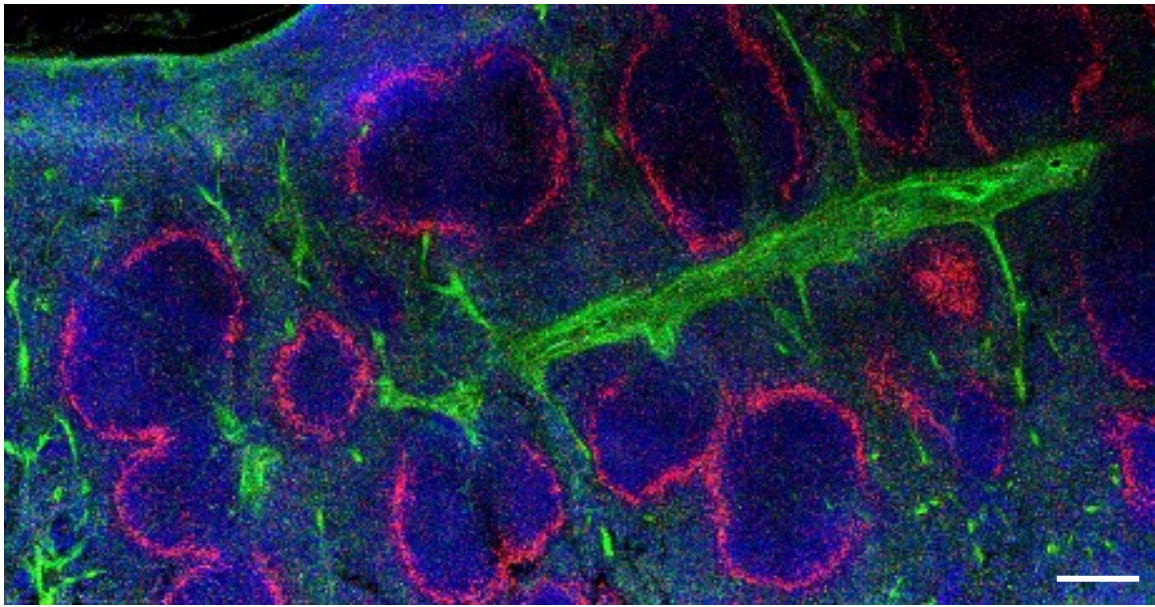


Figure 13: Spleen staining shows vascularization and macrophage rich metallophilic zones. PFA-fixed spleen vibratome section (50 μm layer thickness). Nuclei (Dapi, blue), plasma membrane especially of vessels (WGA, green) and macrophages of the metallophilic zone (CD169, magenta). Scale bar is 100 μm . Maximum projection of a z-stack, imaged with 10 x objective. For illustration purpose brightness and contrast were adjusted.

The next goal was to correlate the eGFP reporter expression to spleen anatomy and to identify individual cell types expressing the reporter protein in LPX treated animals. Preliminary experiments (**Figure 14**) showed that the endogenous fluorescence signal could only be detected very weakly or not at all. It was therefore investigated whether indirect immunofluorescence using antibodies could serve as a reliable amplification strategy. Thus, it was assessed, whether the endogenous GFP fluorescence signals and those of the antibody-enhanced eGFP signal would detect the same structures.

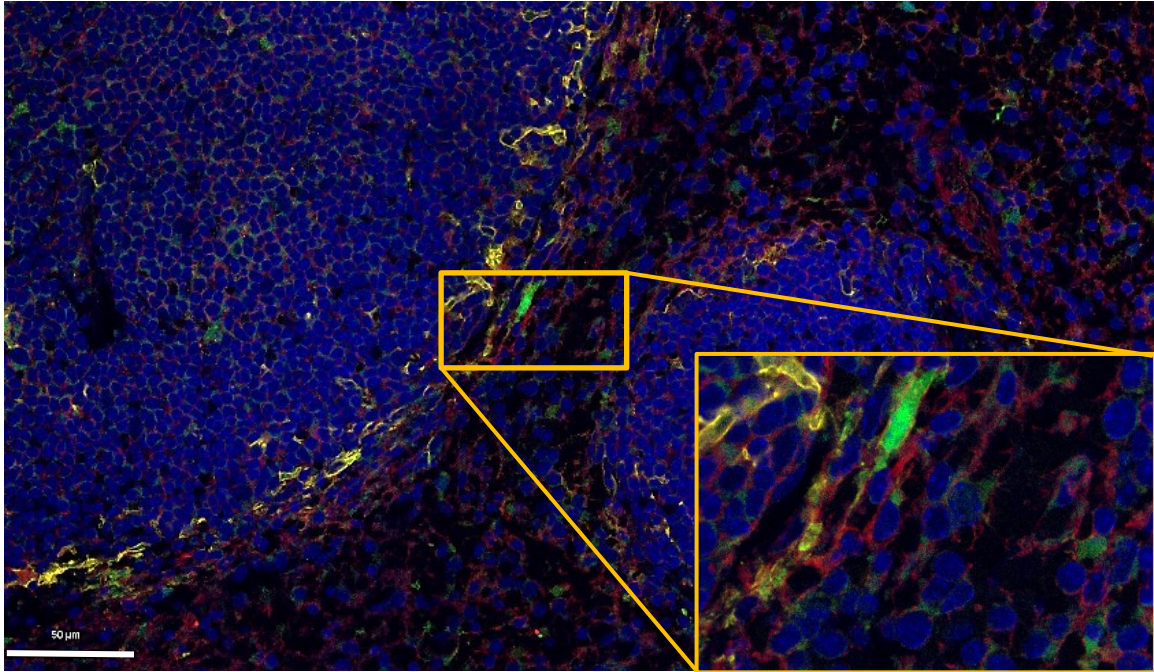


Figure 14: Endogenous eGFP shows only weak signals. Spleen cryo-section (10 µm layer thickness). Nuclei (Dapi, blue), plasma membrane especially of vessels (WGA, red), eGFP reporter (endogenous eGFP, green) and macrophages of the metallophilic zone (CD169, yellow). Lower right side shows an enlargement with single positive eGFP cells and direct neighborhood to CD169 positive macrophages Scale bar is 50 µm. Single optical plane from z-stack image, recorded with 63 x objective. For illustration purpose brightness and contrast were adjusted.

While qualitatively there was a significant overlap between endogenous and immunofluorescence eGFP signals, the signal positive area increased from 2.1 % + 0.7 (mean + SEM, n = 3) in the absence to 17.7 % + 7.2 (mean + SEM, n = 3) in the presence of anti-GFP antibody (**Figure 15**). Due to the significant amplification by antibodies, weaker signals could now also be detected in more complex staining methods.

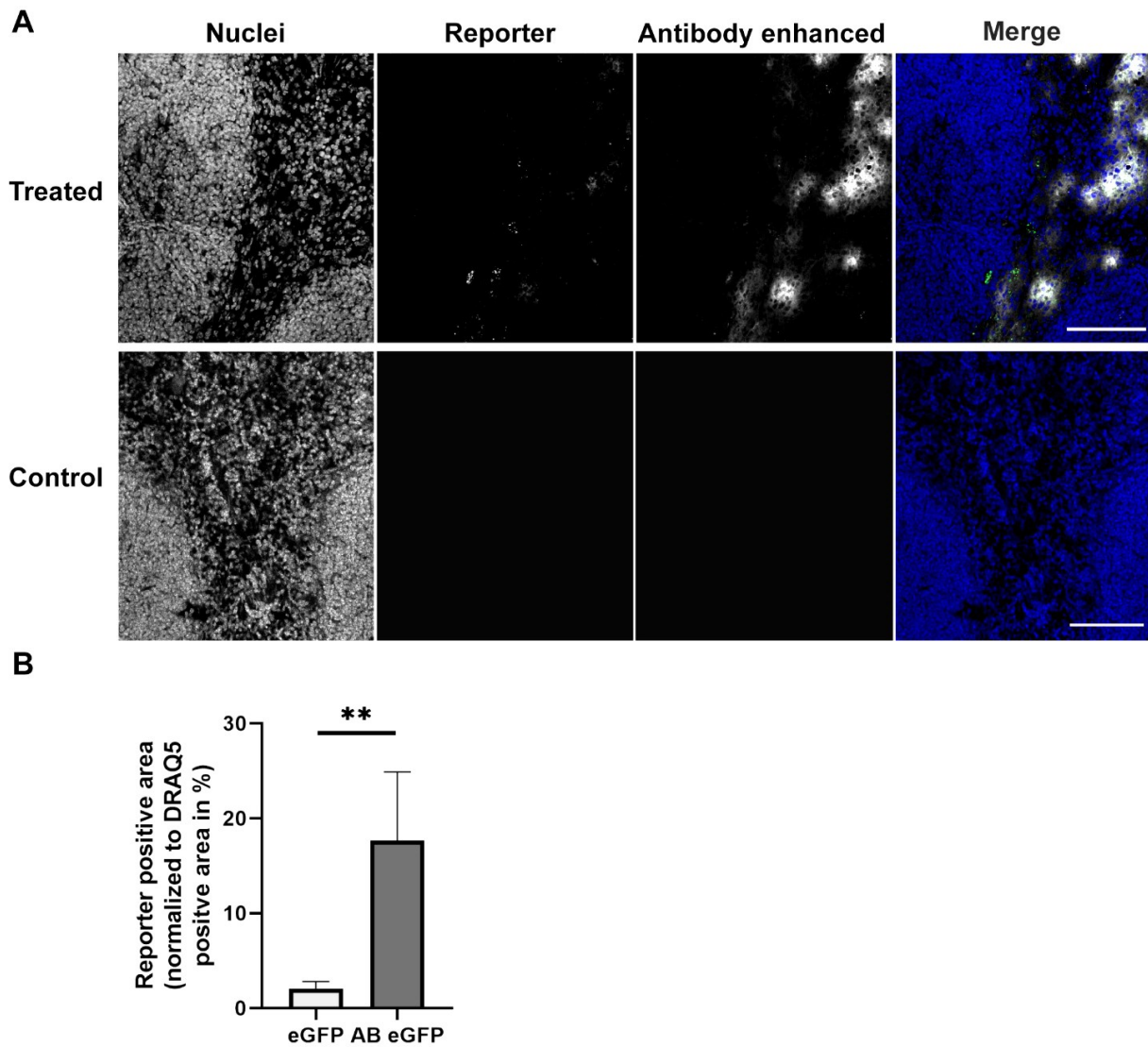


Figure 15: Comparison between endogenous reporter signal and antibody enhanced signal. Representative section of a spleen cryo-section. Nuclei (DRAQ5, blue), mRNA reporter (eGFP, green) and antibody-enhanced reporter signal (anti-eGFP, white). Scale bar is 100 μ m. Single optical plane from z-stack image, recorded with 20 x objective. For illustration purpose brightness and contrast were adjusted (**A**). Antibody enhancement improves the reporter signal from 2.1 % + 0.7 to 17.7 % + 7.2 (mean + SEM, n = 3 independent experiments, at least 1 section per condition). Quantitative analysis. Graph shows the area of endogenous eGFP reporter fluorescence compared to antibody enhanced signal normalized to nuclei signal area. One-way ANOVA with Tukey's multiple comparison post-hoc test ($\alpha = 0.05$), ** p \leq 0.01 (**B**).

In order to be able to work with various other fixation and staining methods and to confirm the LPX expression pattern, firefly luciferase was also tested as an mRNA reporter. The use of a luciferase mRNA reporter as an alternative to the eGFP reporter also revealed signals in previously identified areas.

Indeed, immunofluorescence signals for both reporters were mainly but not exclusively located in the areas between white and red pulp (**Figure 16**).

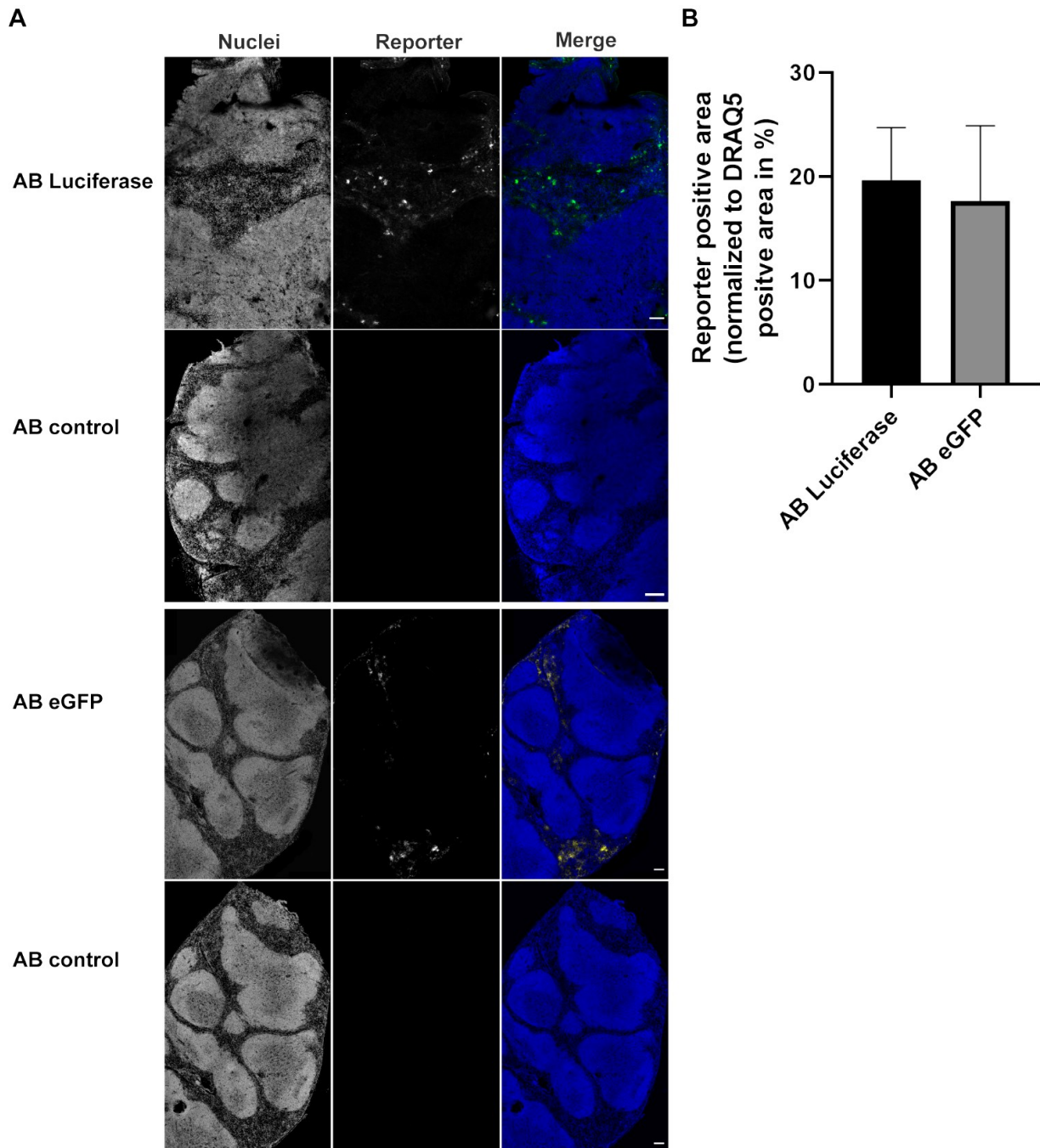


Figure 16: No significant difference between luciferase and eGFP signal area. Representative section of a spleen cryo-section. Nuclei (DRAQ5, blue), antibody enhanced eGFP reporter (yellow) and luciferase antibody enhanced reporter signal (anti-luciferase, green). Scale bar is 100 μ m. Single optical plane from z-stack image, recorded with 20 x objective. For illustration purpose brightness and contrast were adjusted (**A**). luciferase reporter shows signal area of 19.6 % +5.1 and eGFP 17.6 % + 7.2 (mean + SEM, n = 3) of total spleen section area. Quantitative analysis. Graph shows the luciferase fluorescence area compared to eGFP reporter area. Both reporter signals are normalized to nuclei area as a function of LPX amount added. One-way ANOVA with Tukey's multiple comparison post-hoc test ($\alpha = 0.05$). ** $p \leq 0.01$ (**B**).

3.2.1 2D spleen distribution analysis

The first experiments indicated that the mRNA reporter signal tends to be detected predominantly in the border regions between the white and red pulp. From the studies by (Kranz et al., 2016) it is known that the RNA-LPX is mainly taken up by immune

cells and expressed by antigen-presenting cells. The focus of the following experiments is on the colocalization of RNA-LPX expression together with two specific types of antigen-presenting cells, macrophages (CD169) and dendritic cells (CD11c) in spleen of mice.

For the spleen study, adult (f/m) C57BL/6 mice were systemically injected with LPX. The spleen was isolated 6 hours after treatment with RNA-LPX and fixed directly with dry ice. The analyses with the markers for CD169 positive macrophages and CD11c positive dendritic cells showed a differential distribution pattern for CD169 and CD11c positive cells. Indeed, while the CD169 positive cells were found in a narrow ring at the interface between red and white pulp. In contrast, CD11c-positive cells were more prominent in the periarteriolar lymphoid sheaths, red pulp and splenic nodules. Quantitative analysis revealed that 21.3 % +10.1 (mean + SEM, n = 3) of the spleen area was occupied by CD11c positive cells. With respect to macrophages, 9.7 % + 4.9 (mean + SEM, n = 3) of the spleen total area was positive for CD169, a marker for metallophilic macrophages that are reported to be highly active during viral infection (Grabowska et al., 2018) (**Figure 17**).

Since the mRNA-loaded lipoplexes should target precisely these antigen-presenting cells, the following experiments investigated which of these cells are target and in which ratio. Therefore, spleens from mice injected with LPX containing either mRNA encoding for luciferase or for eGFP were used to colocalize with macrophages and dendritic cell markers.

Confocal analysis of spleen cryo-sections showed that the mRNA reporter positive area, normalized to the nuclei area, was 19 % + 3.8 (mean + SEM, n = 3). For the CD169 positive cells, the total area in the spleen resulted in 9.7 % + 4.9 (mean + SEM, n = 3).

By superposition of the signals from CD169 positive macrophages over the mRNA reporter signal area revealed that 9.5 % + 4.4 (mean + SEM, n = 3) of the reporter signal area are also positive for the CD169 macrophages (**Figure 18**).

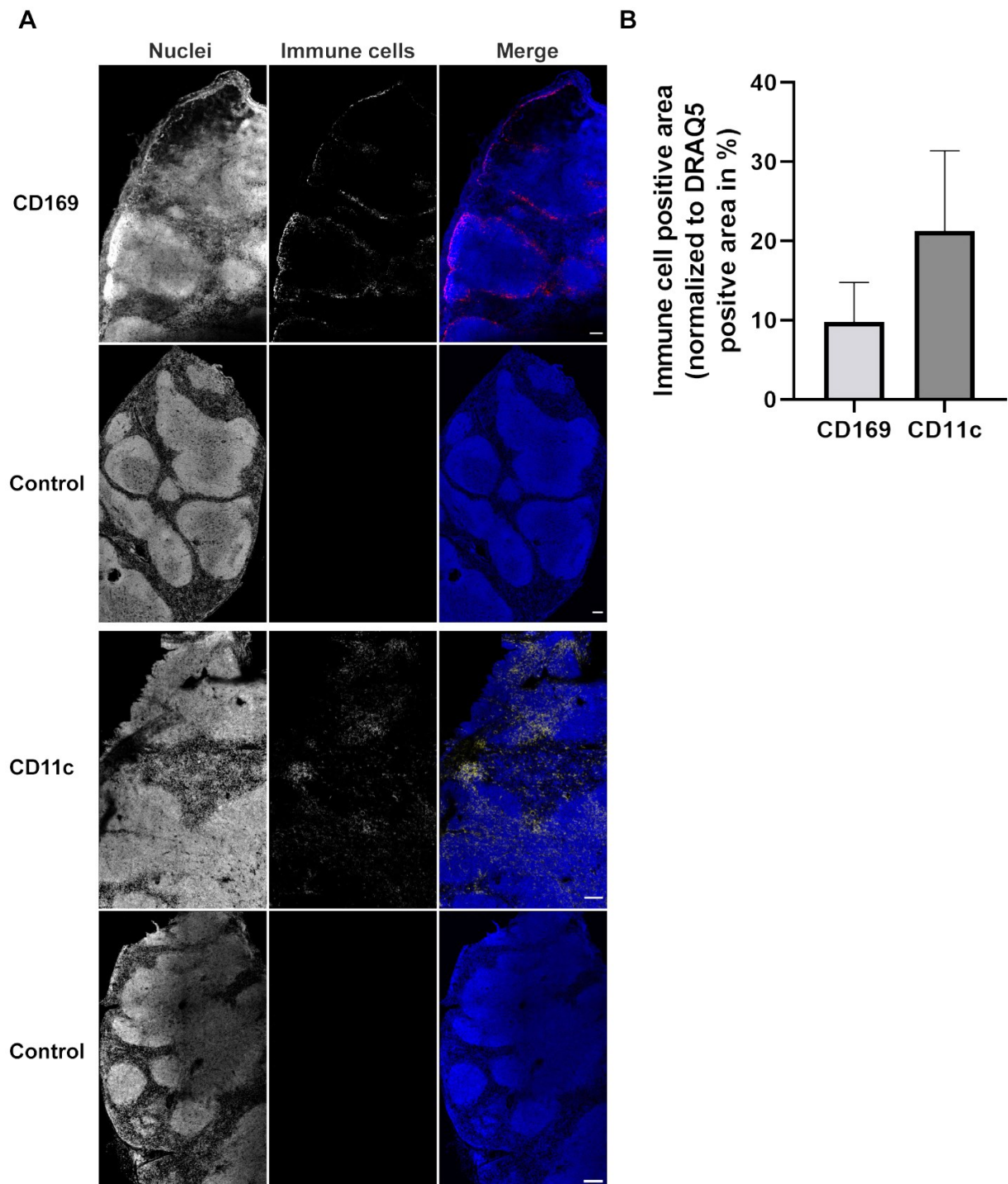


Figure 17: Distribution of CD11c-positive dendritic cells and CD169-positive macrophages in the spleen. Spleen cryo-section stained for nuclei (DRAQ5, blue), macrophages (anti-CD169 antibody, red) and dendritic cells (anti-CD11c antibody, yellow). Scale bar is 100 μ m. Representative single optical plane from z-stack image, recorded with 20 x objective. For illustration purpose brightness and contrast were adjusted (**A**). The CD169 positive macrophages take up 9.7 % + 4.9 (mean + SEM) of the nuclei positive area. The CD11c positive dendritic cells represent 21.3 % + 10.1 (mean + SEM, n = 3 independent experiments, at least 1 section per condition) of the total spleen section area. Quantitative analysis. Graph shows macrophages and dendritic cells fluorescence area normalized to nuclei signal area as a function of LPX amount added. One-way ANOVA with Tukey's multiple comparison post-hoc test (**B**).

In comparison, the analysis of the CD11c fluorescence-stained spleen sections resulted in 21.3 % +10.1 (mean + SEM) signal area. Since the CD11c positive dendritic cells are distributed less restrictively over the entire area of the spleen, signals were also shown in the areas of the white pulp. Whereas the signal of the mRNA reporter can be found more strongly in the border areas between white and red pulp, there was a smaller intersection between CD11c and mRNA reporter positive area in comparison to CD169 cells. The results showed that the 19 % + 3.8 (mean + SEM) mRNA reporter positive area resulted in a double positive area of 6.5 % + 4.0 (mean + SEM) with the CD11c positive dendritic cells (**Figure 19**).

The results showed that both the CD169 positive macrophages and the CD11c positive dendritic cells have an overlap with the signals from the mRNA reporter. However, there is a trend towards a larger overlap with the macrophages compared to the CD11c-positive cells.

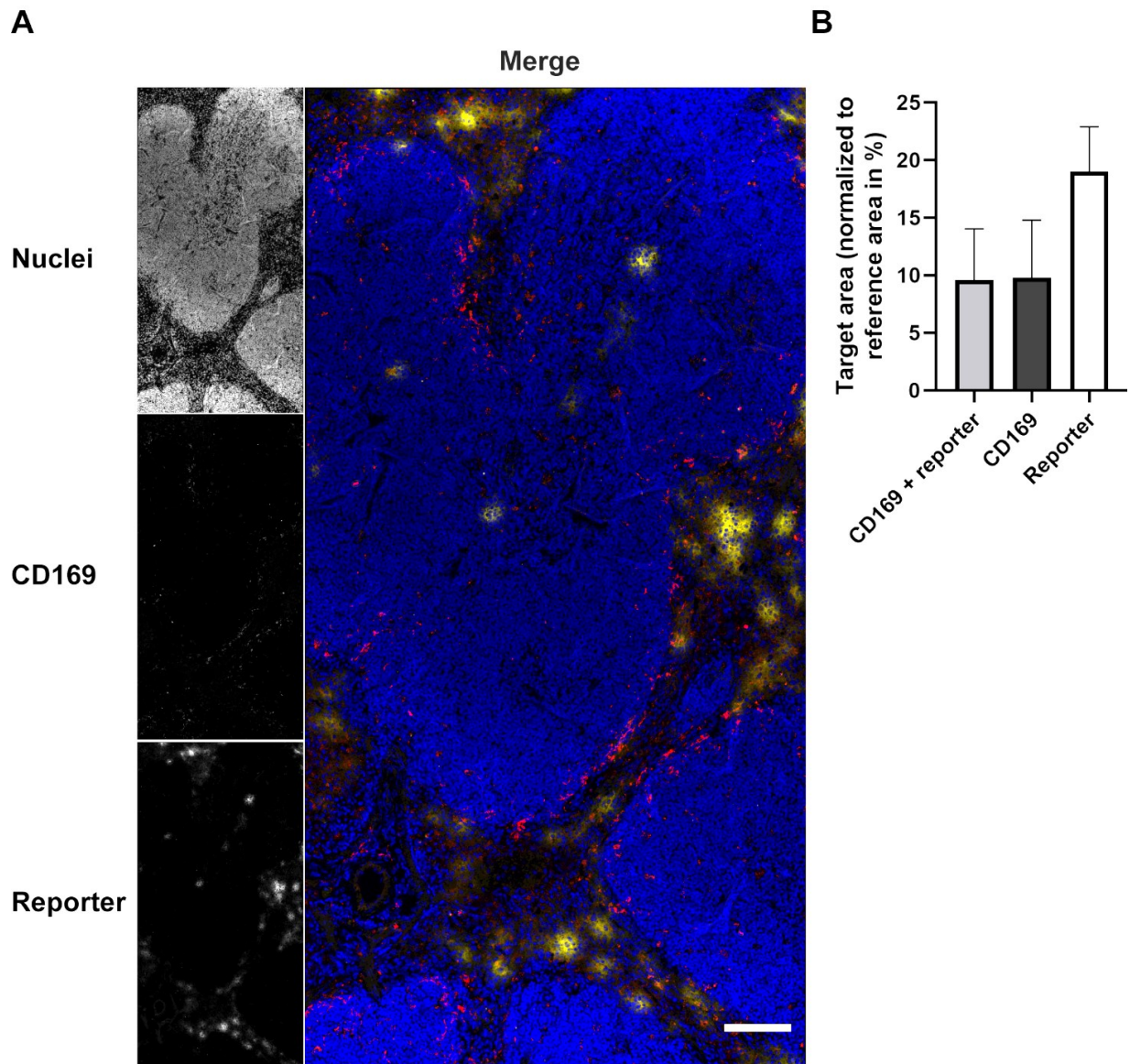


Figure 18: In the marginal zone between white and red pulp, there is an overlap between mRNA reporter and CD169 positive macrophages. Immunofluorescence staining of spleen section shows nuclei (DRAQ5, blue), macrophages (anti-CD169 antibody, red) and mRNA reporter (antibody enhanced, yellow). Representative single optical plane from z-stack image, recorded with 20 x objective (scale bar is 100 μ m). For illustration purpose brightness and contrast were adjusted (**A**). The CD169 positive macrophages take up 9.7 % + 4.9 (mean + SEM) of the nuclei positive area. The mRNA reporter signal represents 19.0 % + 3.8 (mean + SEM) of the total spleen section area and 9.5 % + 4.4 (mean + SEM) of the mRNA reporter signal area is also positive for the CD169 macrophages marker (n = 3 independent experiments, at least 1 section per condition). Quantitative analysis. Graph shows macrophages and mRNA reporter fluorescence area normalized to nuclei signal area as a function of LPX amount added. The mRNA reporter and macrophage double positive area is normalized to the mRNA reporter positive area. One-way ANOVA with Tukey's multiple comparison post-hoc test (**B**).

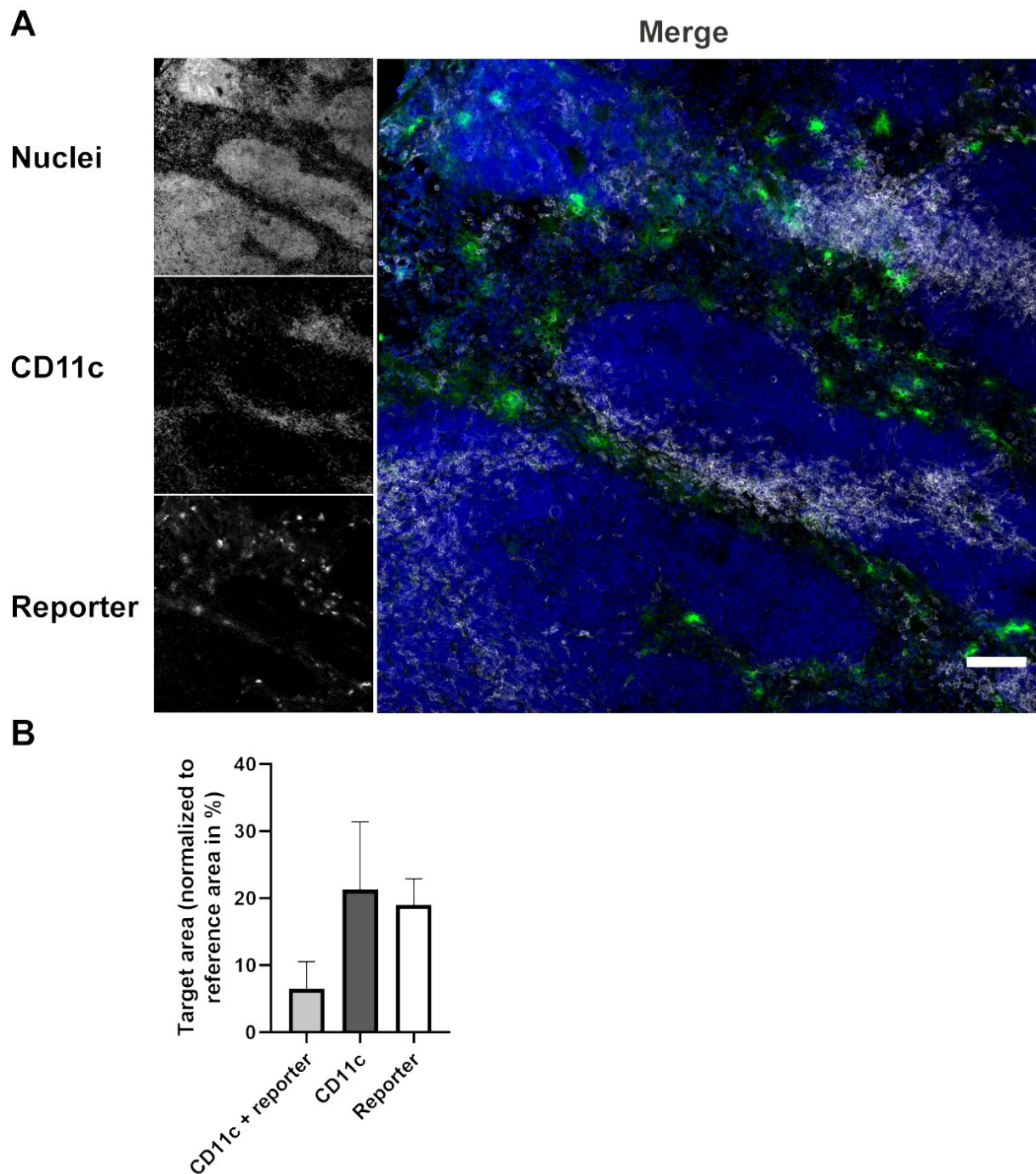


Figure 19: Immunofluorescence analyses show that mRNA reporter signals have overlap with CD11c positive dendritic cells. Immunofluorescence staining of spleen section shows cell nuclei (DRAQ5, blue), dendritic cells (anti-CD11c antibody, white) and mRNA reporter (antibody enhanced, green). Representative single optical plane from z-stack image, recorded with 20 x objective (scale bar is 100 μ m). For illustration purpose brightness and contrast were adjusted (**A**). The CD11c positive dendritic cells take up 21.3 % + 10.1 (mean + SEM) of the nuclei positive area. The mRNA reporter signal represents 19.0 % + 3.8 (mean + SEM) of the total spleen section area and 6.5 % + 4.0 (mean + SEM, n = 3 independent experiments) of the mRNA reporter signal area is also positive for the CD11c dendritic cells marker. Quantitative analysis. Graph shows dendritic cells and mRNA reporter fluorescence area normalized to nuclei signal area as a function of LPX amount added. The mRNA reporter and dendritic cells overlap area is normalized to the mRNA reporter positive area. One-way ANOVA with Tukey's multiple comparison post-hoc test (**B**).

3.2.2 3D tissue clearing for RNA-LPX *in vivo* targeting in the spleen

The results of the reporter-positive 2D spleen sections indicated transfection of both CD11c positive dendritic cells and CD169 positive macrophages with RNA-LPX. To study the distribution of RNA-LPX in a three-dimensional context without sectioning artifacts, whole spleens or large chunks of spleen were examined using optical tissue clearing techniques. To start with, a tissue clearing protocol based on standard paraformaldehyde fixation was used (adopted from (Williams et al., 2019)). The first results of the immunofluorescence staining could be achieved by fixation with 4 % paraformaldehyde (**Figure 20**). These results, however, showed a strong background, which was most likely due to the aldehyde fixation. This allowed only limited contrast and penetration of up to 400 μm depth. Even more critical was the high autofluorescence in the eGFP wavelength range, precluding analysis of reporter distribution. Therefore, different clearing methods were tested for their practicability to detect mRNA transfected eGFP expression in the spleen.

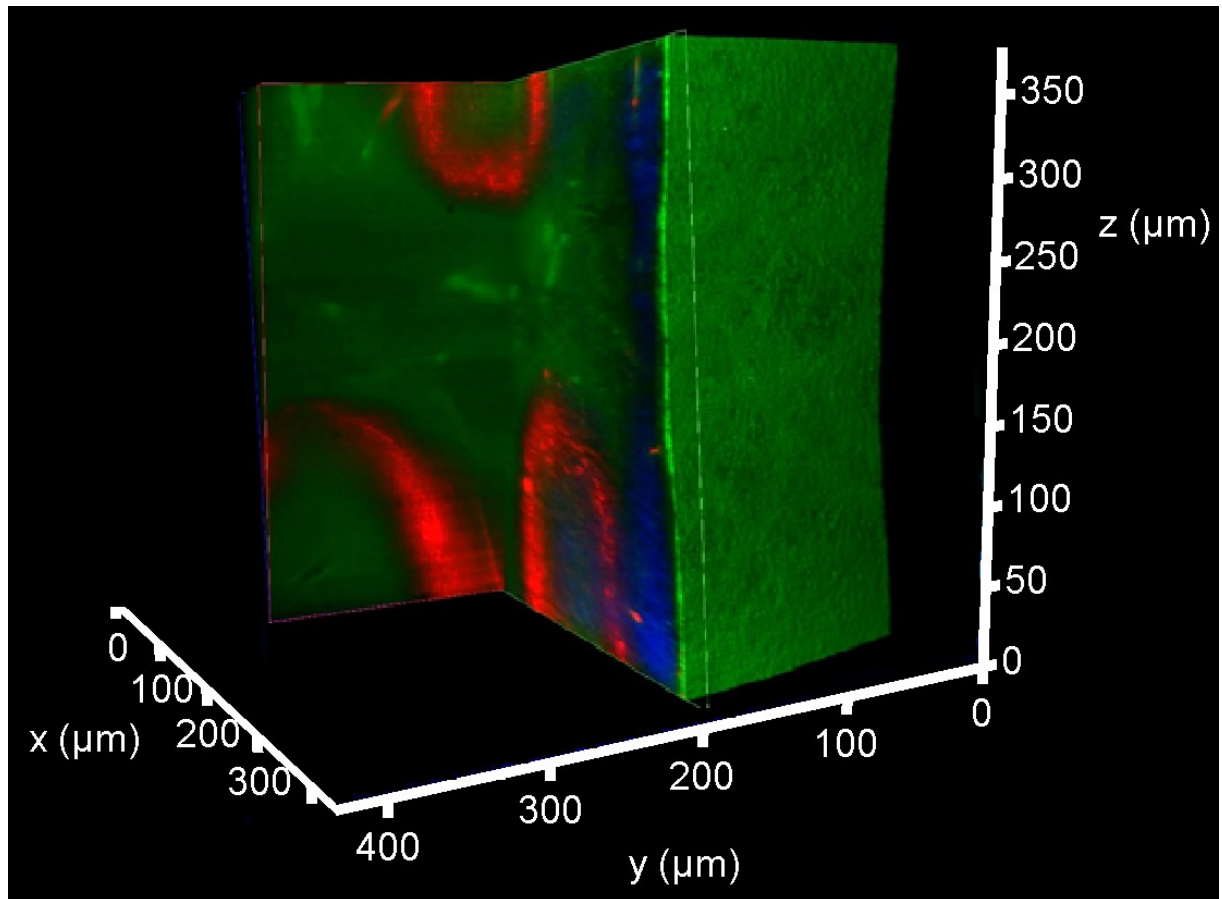


Figure 20: Tissue clearing enables a better understanding of the three-dimensional distribution of substances. 3D volume image of an adult mouse spleen in macrophages marker (anti-CD169, red), lectin marker (WGA, green) and nuclei marker (dapi, blue). A glycerin-based process was used for clearing the PFA fixed tissue. The maximum intensity projection, imaged with the Leica TCS SP8 DLS resulted in a resolution of 350 μm in the Z axis.

3.2.3 Development of a clearing method to detect mRNA reporters in spleen

With blood-rich organs of the lymphatic system such as the spleen, it is particularly important to remove the heme from the organ, as this causes a high imaging background. **Figure 21 (A)** shows a freshly isolated and unfixed spleen. **Figure 21 (B-F)** show the results of different tissue clearing methods. As is known from the literature, different clearing methods have different strengths or weaknesses in clearing different components of the spleen.

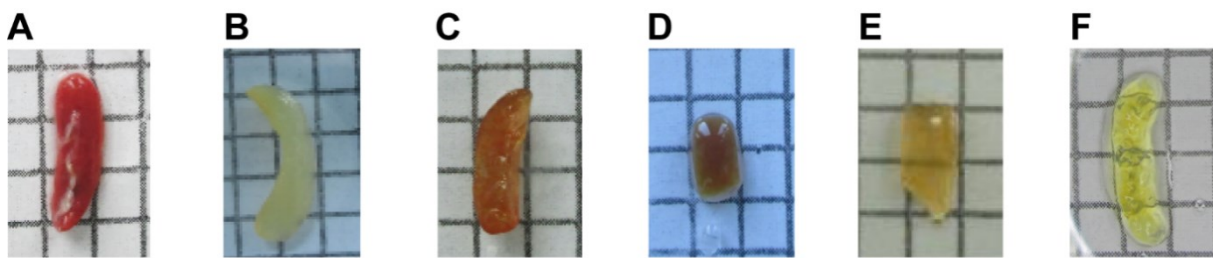


Figure 21: Different clearing capability in the spleen. Control spleen, unfixed spleen immediately imaged after isolation (**A**). Figure B-F show spleens or spleen parts after different clearing methods immediately before microscopic analysis. MYOCLEAR method with acrylamide bisacrylamide tissue fixation (**B**). VisikoI@ HISTO-1/-2™ based clearing procedure (**C**). Spleen part cleared with AbScale based method (**D**). Spleen part cleared with CUBIC 1/2 based method (**E**). DIMM α clearing method (**F**).

Notably, with respect to blood decolouring, fixation with acrylamide bisacrylamide as adopted from (Chung & Deisseroth, 2013; Williams et al., 2019) was beneficial (**Figure 21(B)**). Similarly adequate reduction in hemoglobin coloring was obtained with CUBIC 1/2 (**Figure 21(E)**) and DIMM α (**Figure 21(F)**).

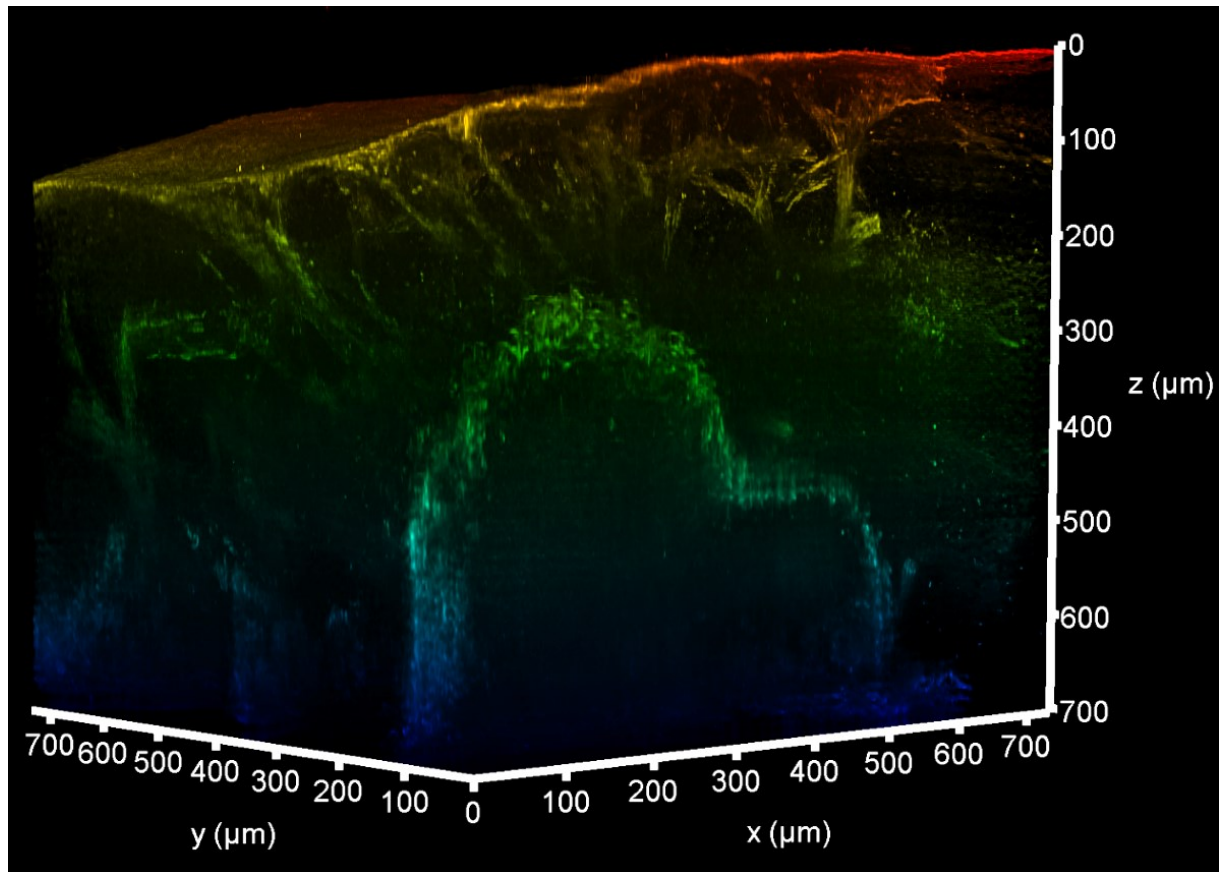


Figure 22: MYOCLEAR method provide good clearing capabilities with moderate penetration in spleen. Representative part of an adult mouse spleen in depth coded view of anti-CD169 macrophages marker. The spleen capsule is on the upper side and the structure typical of CD169 positive macrophages can be seen in the foreground. Spleen adapted MYOCLEAR protocol was used for tissue clearing. The laser intensity was adjusted to the respective control. The maximum intensity projection, imaged with the Leica TCS SP8 DLS resulted in a resolution of 700 μm in the Z axis.

As a result of the acrylamide bisacrylamide fixation, the clearing capability was strongly improved and samples could be imaged up to a depth of 700 μm . **Figure 22** depicts a representative part of an adult mouse spleen in depth coded view. However, even with the adapted MYOCLEAR method, it was not possible to detect the signal from the mRNA reporters (eGFP).

In the next approach, the spleen clearing with Visikol® HISTO-1/-2™ method was examined. After fixation with 4 % paraformaldehyde, the tissue was decolorized with an ascending ethanol series before processing with the Visikol® HISTO-1/-2™ reagents for immunofluorescence labeling and refractive index matching. Unfortunately, although this method showed a good clearing capability, neither the signal of the CD169 positive macrophages nor the signal of the mRNA reporter could be detected (**Figure 23**).

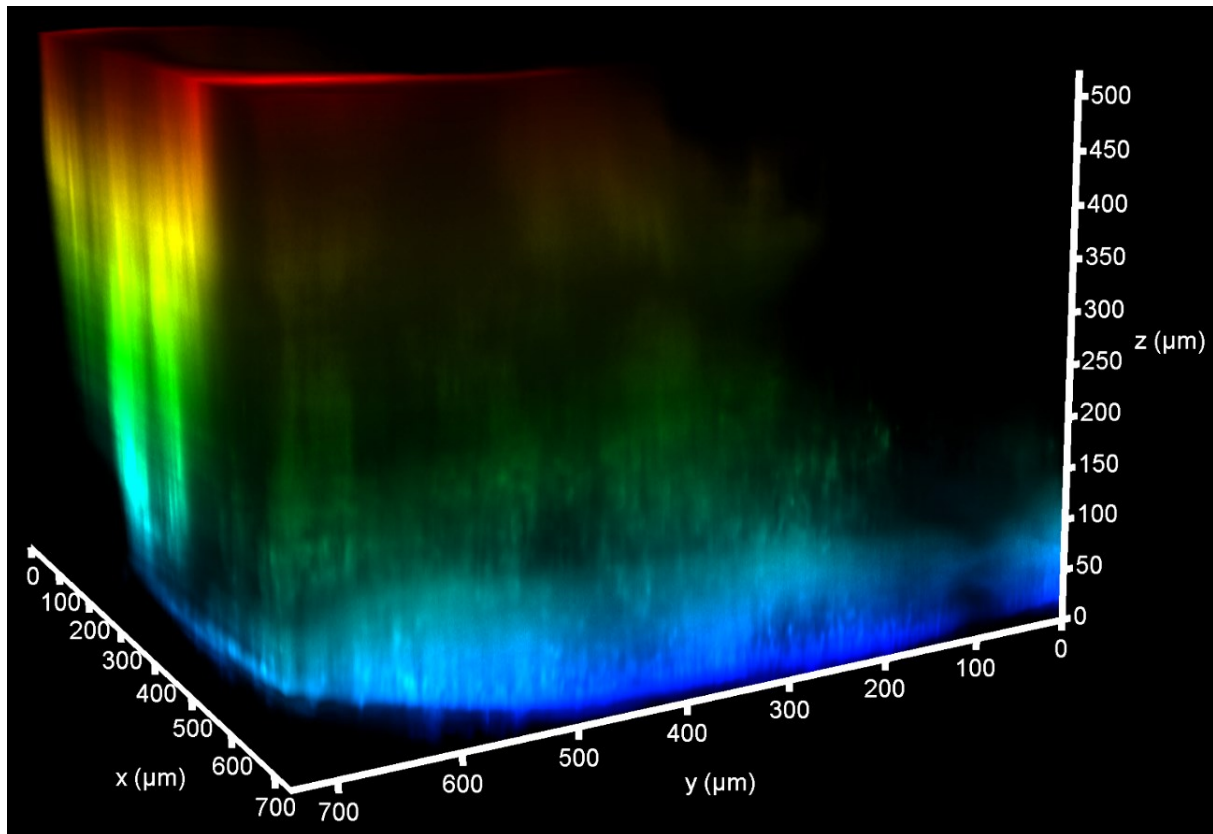


Figure 23: Visikol® HISTO-1/-2™. Image shows a representative part of the spleen in depth coded view processed with Visikol® HISTO-1/-2™ method. This method yields no measurable signals for anti-CD169 and anti-eGFP staining. The laser intensity was adjusted to the respective control. The maximum intensity projection, imaged with the Leica TCS SP8 DLS resulted in a resolution of 500 μm in the Z axis.

Since neither the high refractive index method MYOCLEAR nor the solvent-based Visikol® allowed detection of the mRNA reporter, AbScale (Hama et al., 2015) as a part of hyperhydration methods was tested.

After fixation with 4 % paraformaldehyde, the tissue was permeabilized and decolorized with Triton X-100, urea and glycerol. The sample was then prepared for immunofluorescence labeling using BSA, Tween-20 and Triton X-100. Finally, the refractive index was adjusted with DMSO, glycerol, urea and D-sorbitol (**Table 6**).

With this method, a significant increase in clearing capability could be achieved. Also, CD169 positive macrophages could be detected. However, no signal from the mRNA reporter could be shown (**Figure 24**). Thus, another method from this group was tested. The CUBIC 1/2 method differs mainly in the use of aminoalcohols instead of sorbitol (Seo et al., 2016). By using the CUBIC 1/2 method, it was possible to detect the mRNA reporter with a comparable clearing capability to the AbScale method (**Figure 25**). Unfortunately, further analysis was not possible with this method due to the high background and the lack of detection of the CD169 positive macrophages.

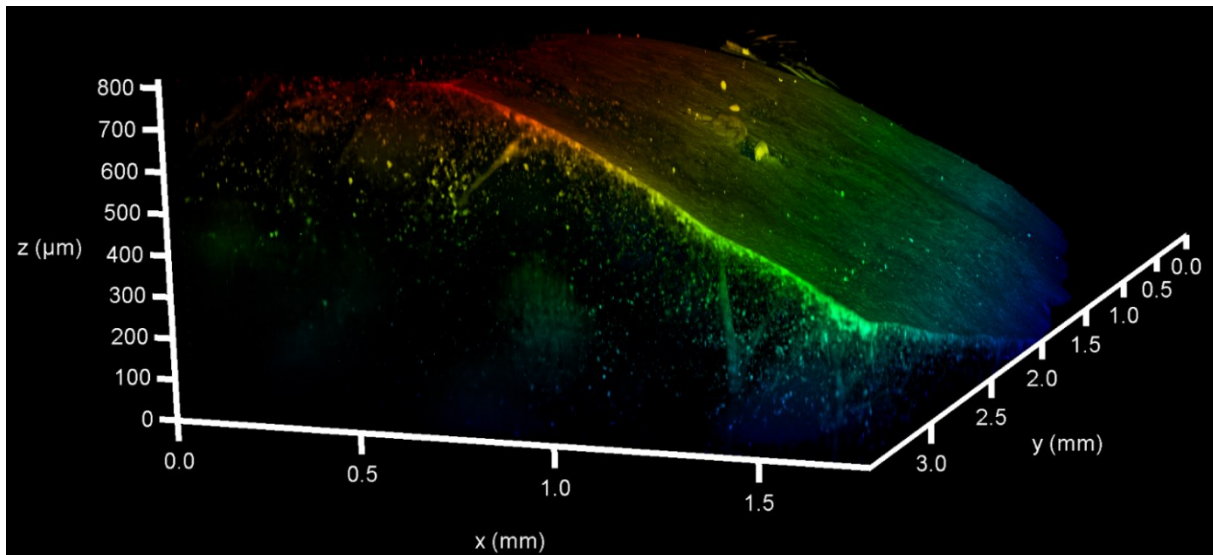


Figure 24: AbScale shows good spatial structure clearing. Representative 3D volume image of an adult mouse spleen in depth coded view of anti-CD169 macrophages marker. The laser intensity was adjusted to the respective control. The maximum intensity projection, imaged with the Leica TCS SP8 DLS resulted in a resolution of 800 μm in the Z axis.

It turned out that each of the previously tested methods had advantages and disadvantages, but none of them fulfilled the parameters required for the target.

Thus, for the development of a specially adapted clearing method, individual components from the tested methods were combined and adapted.

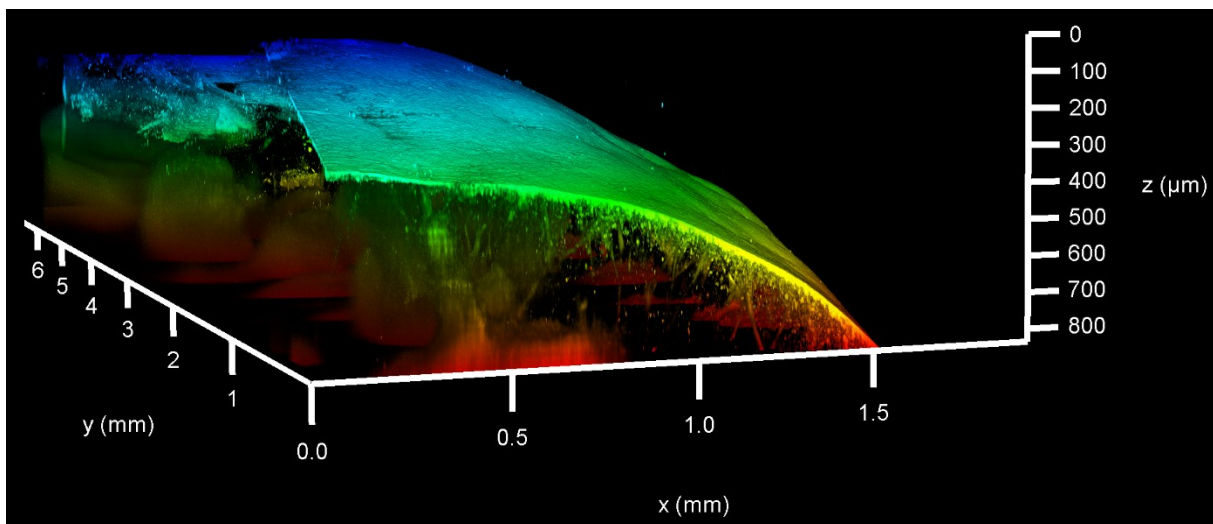


Figure 25: CUBIC 1/2. Image shows a representative part of the spleen processed with CUBIC 1/2 based method. 3D volume image of anti mRNA reporter marker (eGFP) in depth coded view. The laser intensity was adjusted to the respective control. The maximum intensity projection, imaged with the Leica TCS SP8 DLS resulted in a resolution of 800 μm in the Z axis.

The aim was a clearing method for the spleen and the detection of both the mRNA reporter and the marker for the target immune cells. This was achieved by adjusting the fixation, permeabilization, decolorization and especially by optimizing the refractive

index matching. The resulting deep imaging mounting medium (DIMM α), which was composed of sucrose, DMSO, urea, glycerol and quadrol enabled images in which the resolution limit was no longer determined by the tissue used (**Figure 26**). The only limitation was the working distance of the optics. In addition, the immune cells and the cell nuclei could also be detected with this technique in such a way that an analysis is possible (**Figure 30**).

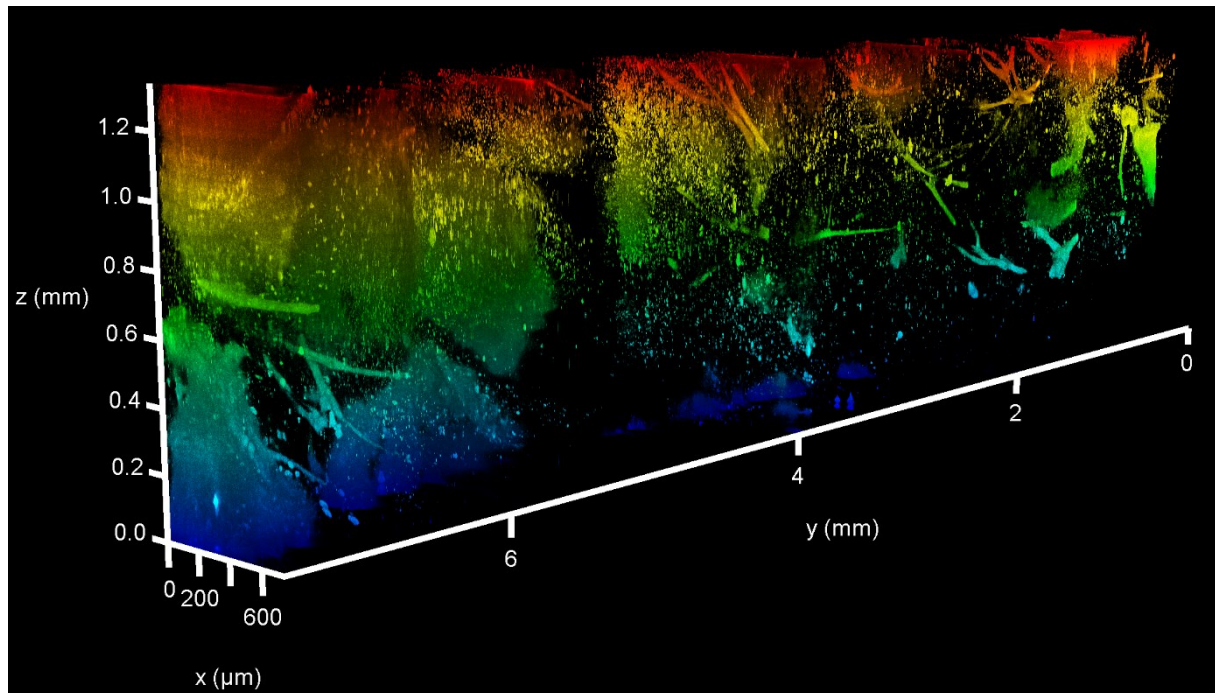


Figure 26: DIMM α provides the best tested clearing capability. Representative 3D volume image of an adult mouse spleen in depth coded view of anti-CD169 macrophages marker. The laser intensity was adjusted to the respective control. The maximum intensity projection, imaged with the Leica TCS SP8 DLS resulted in a resolution ≥ 1.2 mm in the Z axis.

Table 9: Comparison of different clearings techniques related to clearing capability in spleen, usable cell markers and mRNA reporter detection.

Clearing method	Clearing depth	mRNA reporter signal	CD169
MYOCLEAR	700 μm	-	+
Visikol® HISTO-1/-2™	700 μm	-	-
AbScale	800 μm	-	+
CUBIC 1/2	800 μm	+	-
DIMM α	>1200 μm	+	+

3.2.4 3D analysis and colocalization of RNA-LPX expression in spleen

By using DIMM technique, it was possible to achieve a resolution that enables quantitative analyses from 3D scans. The following figure shows an example of a cross-section through a 3D volume image. The structural resolution of the spleen capsule with individual vessels as well as the typical structure of the macrophages of the marginal zone can be identified particularly well (**Figure 27**).

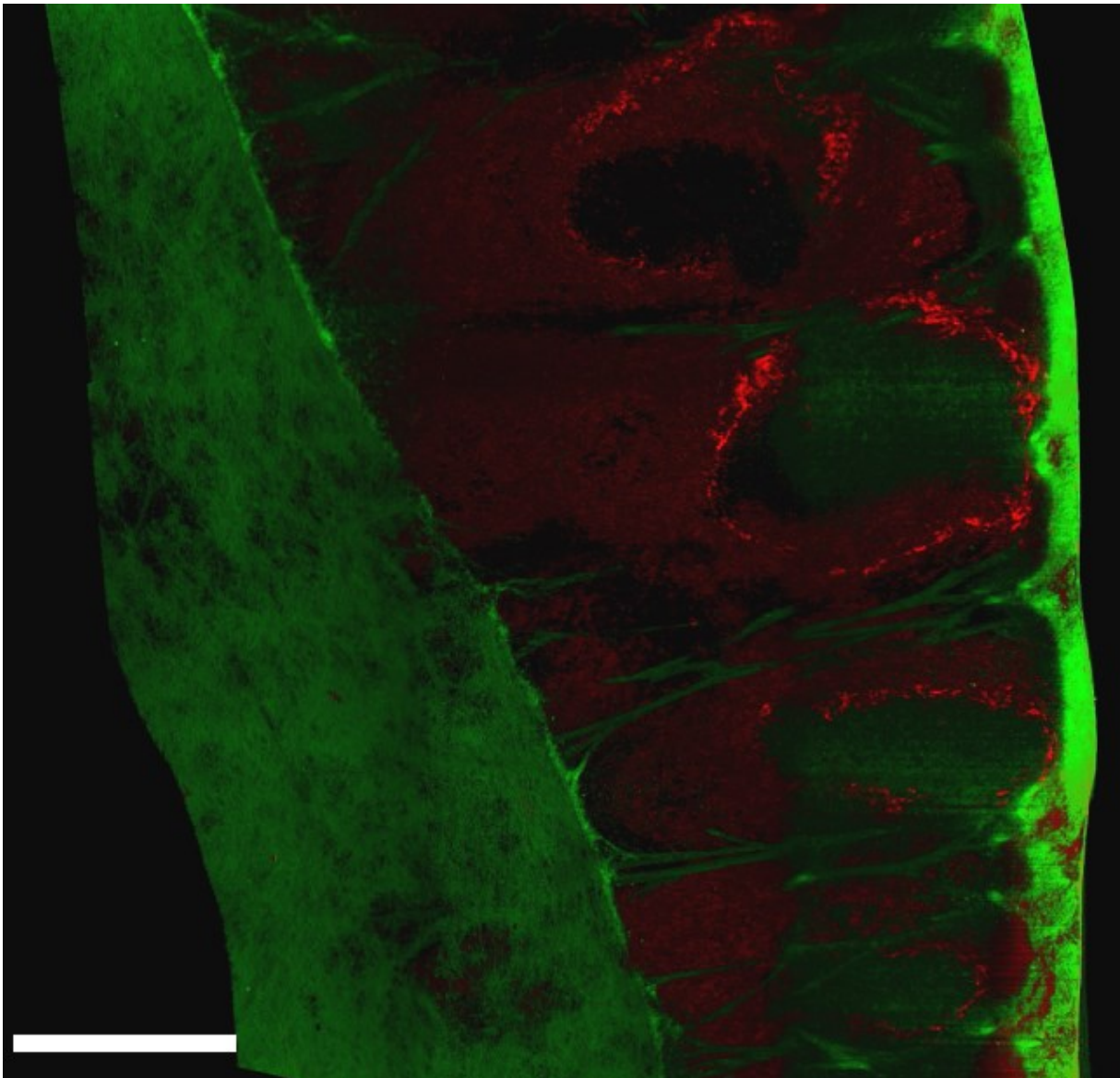


Figure 27: 3D image depicts splenic capsule and marginal zone macrophages. Cross-section of a 3D volumetric image of the spleen, cleared with DIMM α method. Merged image shows macrophages marker (anti-CD169, red) and endothelial cells (anti-CD31, green). Scale bar is 500 μm .

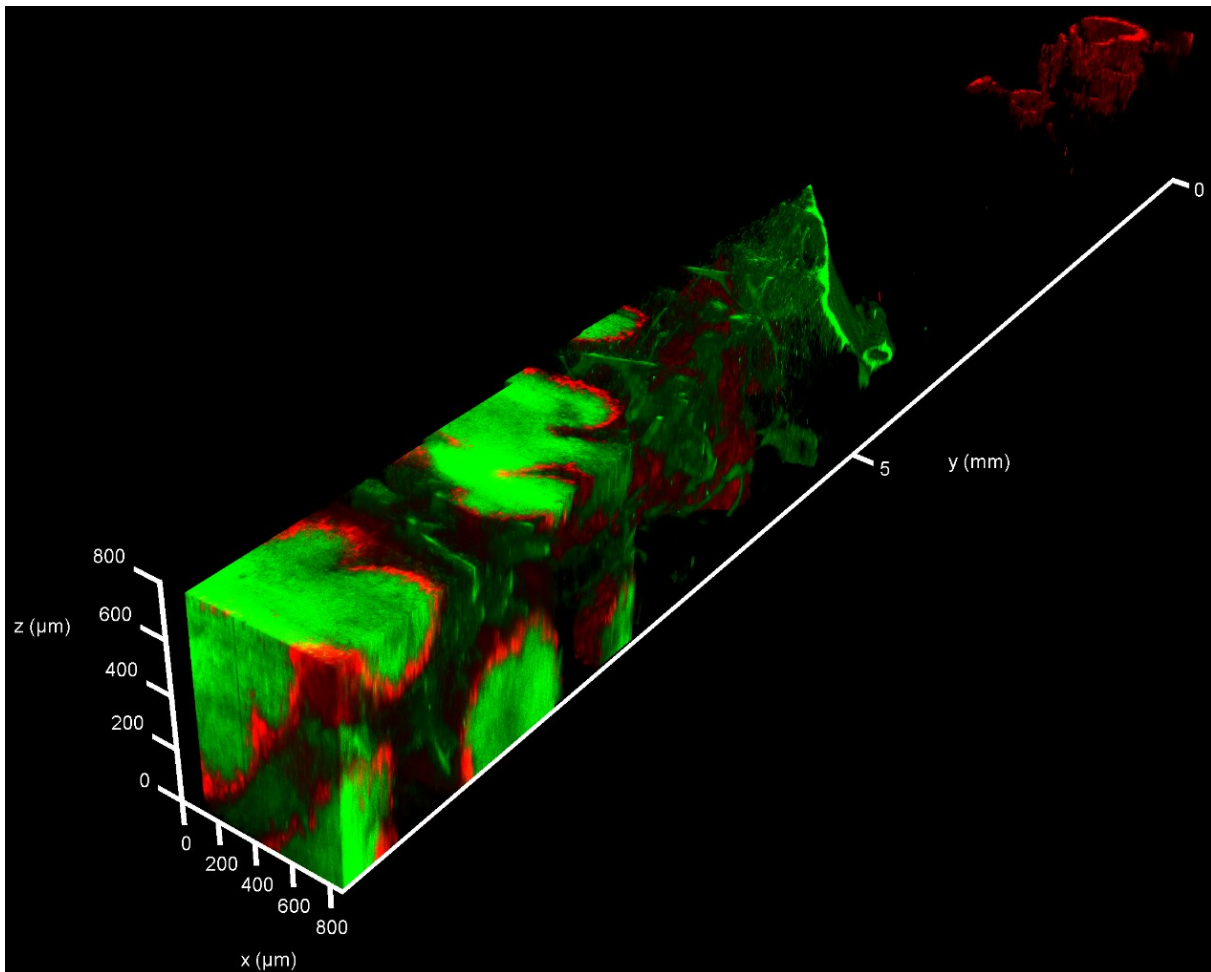


Figure 28: Due to the double mounting technique, treated and negative control organs can be analysed simultaneously. 3D volumetric image of the spleen, cleared with DIMM α method. Labeled with anti-GFP antibody (green) and macrophage marker (red, α -CD169). While both the GFP and the CD169 signal can be seen in the lower half (treated), the untreated control spleen shows only the CD169 signal at the top right.

In order to be able to quantify the samples in a stable and reproducible manner, both the treated spleen and the corresponding negative control were mounted together on the imaging platform.

By mounting the sample and the control at the same time, 3D light sheet imaging was possible with the same setting, e.g. with the same laser intensity and on the same optical plane (**Figure 28**). For practical reasons, this is normally with separately mounted samples rather difficult. This method of mounting made it possible to use the untreated and unstained spleen as a control for the eGFP signal in the case of quantification. In order to minimize the background that occurs in a 3D light sheet recording, an additional channel was recorded in which no specific signal was expected. This empty channel, located between the two target wavelengths, allowed background subtraction to be performed for both eGFP (488 channel) and CD11c / CD169 (647 channel). In **Figure 29**, the raw data was compared to the background

subtracted data. This revealed a significant reduction in the background for the fluorescence signals of both the mRNA reporter (eGFP) and the macrophage marker (CD169).

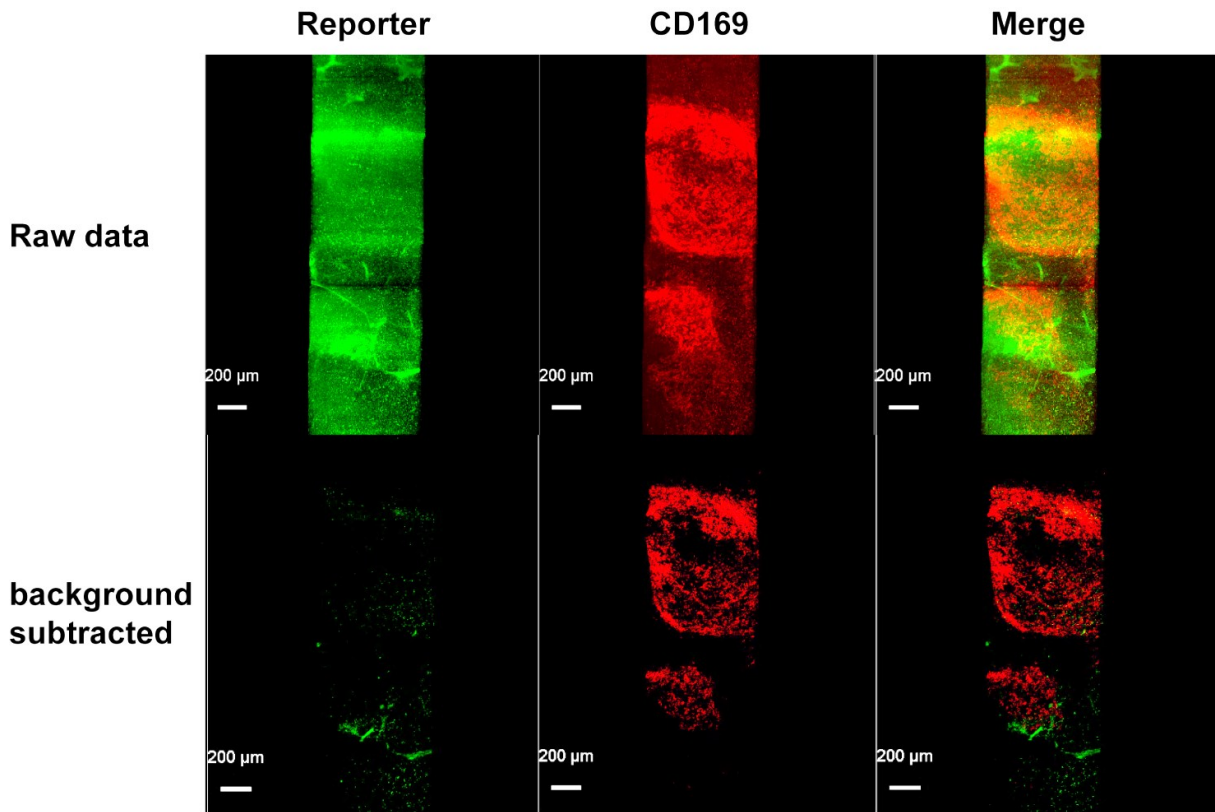


Figure 29: The background subtraction enables a signal quality that allows a quantitative analysis of the RNA reporter signal. Representative 2D projections from a 3D imaged light sheet spleen. The α -GFP signal is shown in green and the macrophage (α -CD169) signal in red. The upper half exhibits the individual signals and the merged signals without processing. The lower half shows the signals of eGFP and CD169 after background subtraction by the empty imaged 552 channel.

These changes, on the one hand due to the clearing technique specifically developed for the target and on the other hand due to post-processing, allowed a quantitative colocalisation analysis of eGFP and the CD169 positive macrophages. For the final experiments, the spleens were isolated after 6 hours of treatment and fixed directly in acrylamide/bisacrylamide. Permeabilization, decolorization, staining and RI matching were achieved with the DIMM α technique. For quantification, in addition to the RNA reporter signal and the CD169 marker, a nuclear staining was added. The light sheet scans were performed with calibration to each individual signal channel. In the following figure, a first, preliminary, quantitative colocalization between the mRNA reporter signal and the macrophage marker CD169, which was prominent in the 2D experiments, was achieved using a 3D light sheet imaging followed by background subtraction (**Figure 30**).

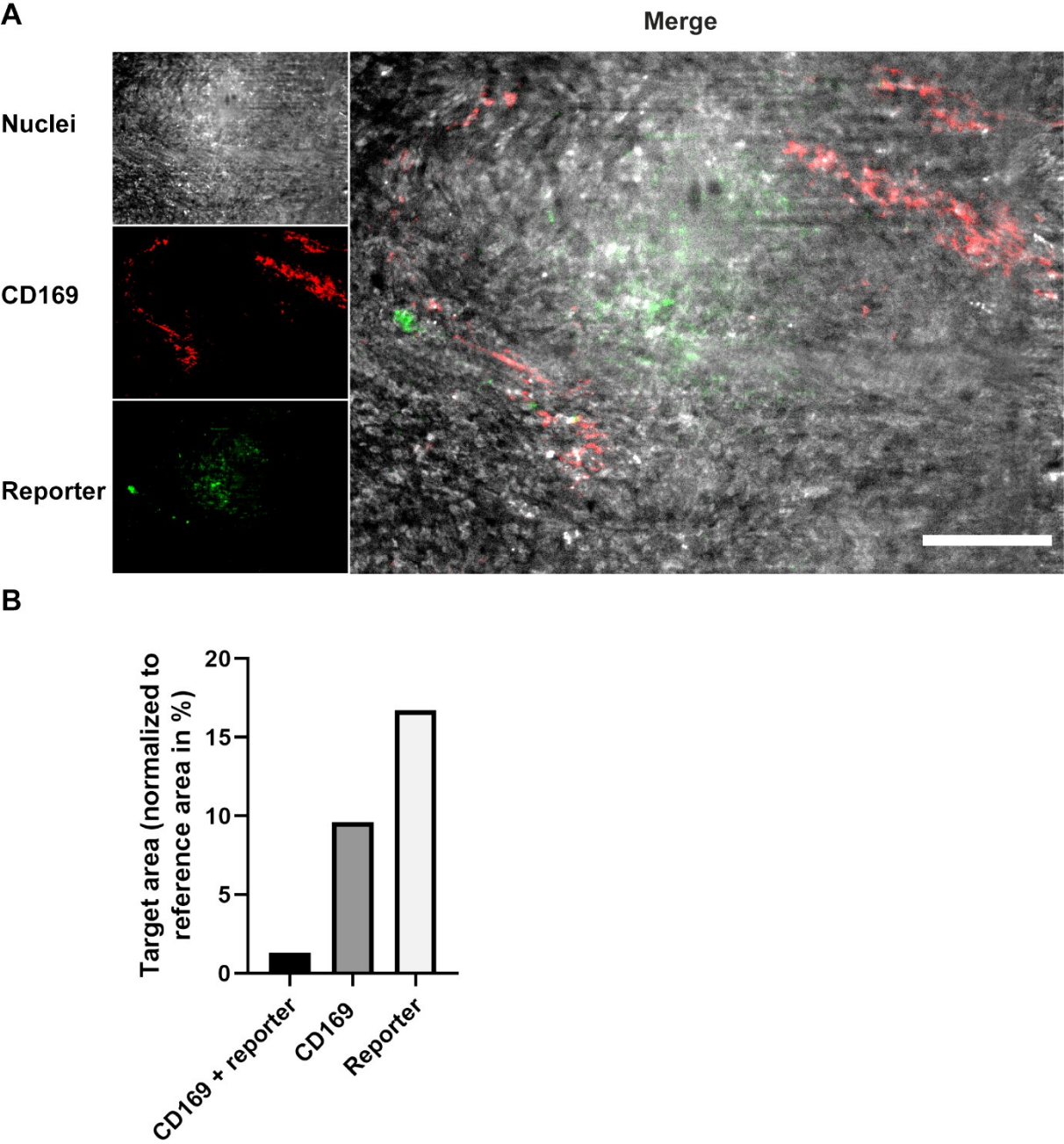


Figure 30: Whole mount RNA reporter signal colocalization provides results that are comparable to those obtained from spleen sections. The α -GFP signal is shown in green, the macrophage (α -CD169) signal in red and nuclei signal in gray. The CD169 positive macrophages represent 9.6 % of the total nuclei positive area. The RNA reporter signal represents 16.7 % of the total measured nuclei area and 1.3 % of the RNA reporter signal area is also positive for the CD169 macrophages marker. 2D projections of a 3D imaged light sheet spleen. Scale bar is 100 μ m, n=1.

4 DISCUSSION

In recent years, it has become apparent that RNA therapeutics in combination with nanoparticles as a transport system could offer a wide range of therapeutic applications for a variety of diseases (Damase et al., 2021). For drug development and preclinical studies of new therapeutics, three-dimensional *in vitro* coculture models are increasingly used because they mimic the complex microenvironment of *in vivo* tissues and the interaction of different cell types better than two-dimensional models (Langhans, 2018). Advances in technology, including analytical systems such as microscopy, have made 3D analysis more feasible, providing a new perspective on cellular distribution and the impact of therapeutics on specific cell types (Hofmann et al., 2020). The aim of the study presented here was to demonstrate cell targeting of lipid-based RNA therapeutics in an *in vitro* melanoma model as well as *in vivo* spleen tissue that represent different routes of administration.

A first focus was placed on the distribution of RNA expression in the presence and absence of the target cells in order to illustrate the behaviour in different therapeutic situations. In order to achieve these aims, a recently developed 3D cell culture model was used which represents the direct application in early stage melanoma (Klicks et al., 2019; Schäfer et al., 2021; Schäfer et al., 2022).

Second, in a murine *in vivo* study, the influence of systemic RNA-LPX application on one of the central organs of the secondary lymphatic system, the spleen, was investigated and its interaction with the antigen-presenting cells located there was examined. For the analysis of these studies, besides classical 2D microscopy, also 3D microscopy was used to obtain an understanding of the effects of the three-dimensional tissue structure on RNA expression distribution. Special interest was on the development of a tissue clearing technique adapted for the detection of lipid-based RNA therapeutics in whole mount spleen samples.

4.1 Local RNA-LPX application *in vitro* study

There is a need for predictive *in vitro* model systems to allow systematic and comprehensive screening of suitable delivery vehicles (Langhans, 2018). So far, cell culture models lack predictivity, presumably because the standard model systems do not adequately reflect the complex situation in the tumor. This study addressed the uptake and reporter gene expression of RNA lipoplex nanoparticles in complex *in vitro*

melanoma tumor models, namely containing tumor and stroma cells in 2D and 3D cell cultures. By using different combinations in mono- and cocultures, the lipofection behavior was found to be dependent on the cellular as well as the 3D context.

While in adherent (2D) monocultures, LPX-mediated eGFP expression was low and did not differ significantly between fibroblasts (CCD-1137Sk), keratinocytes (HaCaT), or melanocytes (SK-MEL 28) cells, transfection efficiency was significantly increased in 2D tri-cultures. According to present concepts of Warburg (Gentric & Mechta-Grigoriou, 2021) and Reverse Warburg effect (Pereira-Nunes et al., 2020; Wilde et al., 2017), which can be observed in 70–80 % of cancers (Vaupel & Multhoff, 2021), interactions between fibroblasts and cancer cells can have stimulatory effects on proliferation and metabolic interactions in different types of cancers (Pandey et al., 2021; Saulle et al., 2020), such as melanoma (Vandyck et al., 2021). Therefore, one may hypothesize that the coculturing of fibroblasts, keratinocytes, and melanoma cells in this study affected their mutual metabolic behavior, including the intensity of cellular uptake.

Using 3D monoculture spheroids, results differed substantially from those obtained with the 2D models. While transfection efficiencies in adherent monocultures were not significantly different between the three tested cell lines, spheroids composed exclusively of SK-MEL 28 cells showed the highest transfection rate of all cell lines. Evidence for this came from both microscopic (**Figure 6**) as well as cytometric analysis (Schäfer et al., 2022). It cannot be excluded that this was, at least partially, due to an enhanced up-/down-regulation of uptake into SK-MEL 28 or CCD-1137Sk cells, respectively. However, penetration of the reagent into the spheroids was also likely affected; whereas SK-MEL 28 spheroids showed eGFP-positive cells throughout the spheroid width, eGFP signals were limited to the outer layers in both HaCaT and CCD-1137Sk spheroids. A likely explanation for this restriction of GFP fluorescence is that CCD-1137Sk and HaCaT cells formed rather compact and tight layers, while SK-MEL 28 cells generated more loose spheroids, which could be related to their decreased E-cadherin expression (Hirano et al., 2013). Morphologically, this was corroborated by small and densely clustered cells in spheroids composed of CCD-1137Sk and HaCaT cells and larger cells in the case of SK-MEL 28 spheroids (**Figure 6**). In this context, the differential cell sizes might hint to the discussed variations in metabolic and proliferative activity. Additionally, previous work showed that both CCD-1137Sk and HaCaT cells have a low proliferation capacity in spheroids and that proliferating cells

were almost exclusively found in the outer regions of spheroids (Klicks et al., 2019). This was confirmed by additional immunofluorescence-staining data using the proliferation marker Ki67 (Supplementary Figure S4 in (Schäfer et al., 2022)). In summary, location in a spheroid, cell density, and metabolic/proliferative activity might be important additional determinants of lipofection efficiency.

Finally, it was observed that tri-culture spheroids composed of a CCD-1137Sk core, a HaCaT ring, and outer groups of SK-MEL 28 cells (Klicks et al., 2019; Schäfer et al., 2021) showed an overall reduction in eGFP-positive cells compared to the 2D tri-cultures and also compared to any of the monoculture spheroids (**Figure 10**) (Schäfer et al., 2022). Partially, this can be explained by the special arrangement of cells in the spheroid (**Figure 12**). Indeed, in the tri-culture spheroids the relative amount of the most well-transfected HaCaT and SK-MEL 28 cells was reduced in comparison to the monoculture spheroids. Furthermore, the CCD-1137Sk fibroblasts, which were already weakly transfected in the monoculture spheroids and present only in the outer cell layers, were enclosed in the tri-culture spheroids by several layers of HaCaT and SK-MEL 28 cells (**Figure 11**). From previous studies, it is also known that 3D cultures change cellular communication and thus also influence processes such as proliferation, protein biosynthesis, and mRNA expression (Maria et al., 2011; Pageau et al., 2011). Furthermore, while in the adherent cultures soluble factors released by any of the cells were likely available for all others due to the even exposure to media, the situation in the tri-culture spheroids might have been different. Indeed, in these cultures, fibroblasts are known to be largely separated from keratinocytes and melanoma cells because they form a central core (Klicks et al., 2019; Schäfer et al., 2021; Schäfer et al., 2022). While cell–cell interactions would be expected to occur at the interface between the fibroblast core and the innermost layer of the keratinocyte ring, the interaction between fibroblasts and melanoma cells in this model are likely to be only weak via paracrine factors. Whether this contributed to the uptake behavior of the tri-culture spheroids, has remained elusive. In summary, the results indicate that substantial differences may be observed when using cell culture models of different complexity. Correlation with *in vivo* results will be necessary to allow for an assessment of the predictivity of the different model settings. The present data represent a step towards the development of such complex and indicative *in vitro* models. Such tools can be helpful for development of novel mRNA therapeutics, where direct delivery to the tumor is required.

4.2 RNA-LPX *in vivo* treatment targeting antigen presenting cells in lymphoid organs

4.2.1 Systemic application for *in vivo* spleen targeting in 2D

In the systemic application of RNA-LPX, the targets are antigen-presenting cells (APCs). In the organs of the secondary lymphatic system, lymphocytes come into contact with antigens. The spleen as a filter organ is the key organ in which the various APCs can be located and targeted (Habbedine et al., 2017). The net charge of the RNA-LPX is used to target certain cells of the immune system (Kranz et al., 2016).

To produce the RNA-LPX, liposomes with cationic net charges were used according to the protocol by Grabbe et al. 2016 which is based on the ethanol injection technique (Batzri und Korn 1973) from the cationic synthetic lipid (R)-N,N,N trimethyl-2 -3-dioleoyloxy-1-propanaminium chloride (R-DOTMA) and the phospholipid 1,2-dioleoyl-sn-glycero-3-phosphoethanolamine phospholipid (DOPE). Instead of mRNA encoding for tumor-associated antigens, mRNA encoding for eGFP or luciferase was used. For the visualization of the typical structures of the spleen, specific antibodies were used that allowed the depiction of vessels and APCs as well as the signal of the mRNA reporter (**Figure 13**). The first experiments indicated that the endogenous mRNA reporter signal was only occasionally expressed in the white pulp and mainly found around the white pulp. Interestingly, the endogenous reporter signal was also occasionally found in the red pulp and was increasingly expressed in the marginal areas between the white and red pulp (**Figure 14**). In addition to APCs, B and T lymphocytes are also found in different areas of the spleen however it is known that APCs make the initial contact with exogenous material in the spleen while they are in contact with other lymphocytes over channels between the white pulp and the red pulp (Mebius & Kraal, 2005).

The partially very weak endogenous reporter signal could be significantly enhanced by using a specific antibody to make the analysis more comparable to other stainings (**Figure 15**). Due to the use of different reporters (eGFP and luciferase), it was possible to prove that the signals did not differ significantly and are mainly found in the areas of the channels between the red and white pulp, as well as in the marginal zone (**Figure 16**). Previous studies indicated that primarily dendritic cells and macrophages are addressed by RNA-LPX, which is why other antigen-presenting cells such as B cells were not included in this study (Affandi et al., 2020; Dey et al., 2021; Kranz et al., 2016). The spleen contains several subsets of macrophages including white pulp

macrophages, red pulp macrophages and metallophilic macrophages of the marginal zone located between the red and white pulp (A-Gonzalez & Castrillo, 2018). Particularly CD169 positive macrophages play a fundamental role as gatekeepers for the adaptive immune system due to their interaction with B cells and dendritic cells (Grabowska et al., 2018; Junt et al., 2007; Veninga et al., 2015). In tissue, dendritic cells can also be divided into several subgroups derived mainly from plasmacytoid DC (pDC) and conventional DC (cDC) (Backer et al., 2019). Plasmacytoid DCs are characterized by weak antigen presentation, but are important for defense against viral infections, and are involved in anti-tumor responses (Alculumbre et al., 2019). Conventional DC are defined by high CD11c and MHC class II expression, which makes them highly specialized for interaction with T cells (Schlitzer et al., 2015; Sichien et al., 2017). **Figure 17** shows the distribution of these two subtypes of APC (CD11c and CD169). Other studies have reported similar results, with the cytometric analyses showing lower values for the CD169 and CD11c markers (Hensel et al., 2019; Immig et al., 2015). However, a slight difference of absolute values was to be expected based on the microscopic analysis and does not affect the comparability with other microscopically determined data in this study. The increased levels of CD11c-positive signals could also be a result of the treatment with RNA-LPX, as suggested by other studies in which an increase in CD11c-positive cells was detected after nanoparticle treatment (Groot et al., 2018; Kranz et al., 2016; van der Jeught et al., 2018).

To investigate the correlation between the signals of mRNA reporter and CD11c and CD169, the signals were combined and the intersection of the signal area was measured. The mRNA reporter signal area was found to correlate with the signal area of CD169 positive macrophages by $9.5 \% + 4.4$ (mean + SEM) (**Figure 18**). For CD11c positive cells, the intersection in the signal area was $6.5 \% + 4.0$ (mean + SEM) (**Figure 19**). As previously indicated in cytometric analyses, the reporter signal induced by RNA-LPX is expressed by both dendritic cells and macrophages (Kranz et al., 2016). The microscopic results from the 2D spleen sections are indicative and demonstrate that although a higher number of CD11c positive cells are detected, the signal area of the CD169 positive cells correlated more closely with the signal of the mRNA reporter. One possible explanation for these results could be the uptake mechanisms. From previous studies it is known that the main mechanism of RNA-LPX uptake is macropinocytosis (M. Diken et al., 2011; Kranz et al., 2016). Macropinocytosis is involved not only in uptake but also in antigen presentation in both macrophages and

dendritic cells (Lin et al., 2020; Toh et al., 2019). In macrophages, macropinocytosis is constitutive (Lin et al., 2020; Norbury et al., 1995), whereas in mature dendritic cells macropinocytosis is no longer active (Sallusto et al., 1995). Since the tissue samples were isolated and fixed 6 h after intravenous injection, it can be assumed that the CD11c positive cells represent a population of activated APCs (Kranz et al., 2016). This could be a reason for a lower colocalization between mRNA reporter signal and CD11c positive cells. Further studies with different incubation times and macropinocytosis inhibitors such as rottlerin in the spleen could be used to investigate these results in more detail.

4.2.2 3D tissue clearing for RNA-LPX *in vivo* targeting in the spleen

To investigate the relationships between structure and function in biological tissues 3-dimensional analyses may be required (Richardson et al., 2021). Complex structures in organs and the spatial context that is often lost in classical 2D sections are essential to address certain questions. Often, a variety of cell-specific markers are required to gain an understanding of the interaction in the organ. In the last decades, the combination of new high-resolution microscopy and new clearing techniques has enabled better 3D analyses of tissue samples. A main hurdle to overcome was the opacity of biological tissues due to light scattering and light absorption (Tian et al., 2021). Since light scattering and light absorption vary from tissue to tissue and lipids are often removed or the fluorescence of reporters can be damaged during chemical tissue clearing, not all techniques can be used for all tissues. Organs that are particularly rich in pigment and contain high concentrations of melanin and heme, for instance, are still a challenge (van der Heijden et al., 1995).

State-of-the-art 3D light sheet microscopy allows for scanning complete organs without preparation of sections. This prevents cutting artefacts and at the same time allows light sheet microscopy to quickly record 3-dimensional structures. Especially with complex structures such as organs of the immune system, these 3D scans offer additional information (Chatterjee et al., 2018; Fischer et al., 2011; Neri et al., 1992). The aim of this part of the study was to provide a first comparison between 2D and 3D generated data. Similar to the 2D generated data, the focus was on the detection and analysis of the mRNA reporter signal as well as the colocalization with targeted immune cells. As expected, initial experiments revealed that the spleen, which is rich in blood and pigment, presents a challenge for tissue clearing (**Figure 20**). Most

standard tissue clearing techniques consist of several steps in which the tissue is fixed, permeabilized, decolorized and finally the refractive index is matched (Tian et al., 2021). Various well established clearing methods were tested in order to detect the signal of the mRNA reporter (encoding for eGFP) and at the same time to achieve the highest possible clearing capability (**Figure 21**). Initially, the fixation was changed to accommodate the special requirements for cleaning the spleen, in order to remove as much pigment as possible during the subsequent decolorization, in particular the heme, which produces a high background in light sheet microscopy (Chung & Deisseroth, 2013; Yu et al., 2021). With this adapted MYOCLEAR technique, the clearing capability was significantly improved, but detection of the mRNA reporter signal was still not possible (Williams et al., 2019) (**Figure 22**). One possible source for the strong background could be hemosiderin in the red pulp, and melanin which are known for their strong pigmentation (Sato et al., 2012; van der Heijden et al., 1995). Furthermore, it is known that there is a high autofluorescence in the spleen, especially in the wavelength range around 488 nm (Gary E. Carver et al., 2013). To address this problem, a commercially available method was tested that has already achieved good results in other tissues and may have potential in spleen microscopy. However, the adapted Visikol® HISTO-1/-2™ protocol did not provide mRNA reporter signal (**Figure 23**). This could be due to the harsh permeabilization and decolorization reagents used in this method.

The group of aqueous-based tissue clearing methods is known to be safe and fluorescent protein friendly (Tian et al., 2021). The AbScale technique belongs to the subgroup of simple immersion methods and is known for a strong clearing capability based on urea-mediated hydration (Hama et al., 2015). The assumption is that urea relaxes protein scaffolds such as collagen fibers by forming hydrogen bonds and disrupting the hydrogen bonding networks of the proteins, and hence a higher transparency can be achieved (Tainaka et al., 2016; Yu et al., 2021). Although a higher clearing capability and a strong CD169 signal could indeed be achieved with this technique, detection of the mRNA reporter signal remained unsuccessful (**Figure 24**). As the detection of the mRNA reporter is elementary for a comparison between 2D and 3D images, another method of aqueous-based tissue clearing techniques was tested. The CUBIC 1/2 method mainly uses aminoalcohols in an attempt to delipidate the tissue (Susaki et al., 2015; Tainaka et al., 2016; Tainaka et al., 2018). The use of amino

alcohols should result in greater removal of lipids and therefore less light scattering (Yu et al., 2021). This mechanism is intended to facilitate heme release and therefore contribute to the decolorization effect of the spleen. Interestingly, with the adapted CUBIC 1/2, the mRNA reporter signal could be detected but no immune cell or nuclei marker signal (647 nm & 405 nm) (**Figure 25**).

The previous experiments indicated that each method was convincing in certain aspects, but the overall result was not yet sufficient for the final analyses (**Table 9**). The combination of several elements such as hydrogel embedding and the use of different chemicals such as urea and quadrol made it possible to create a new technique specifically tailored to the spleen and the detection of mRNA reporters. This has enabled the advantages of gentle hydrogel embedding to be combined with the strengths of a new RI-matching solution based on sucrose, urea, glycerol and quadrol. The Deep Imaging Mounting Medium allowed images to be acquired at depths greater than 1200 μm (**Figure 26**). Furthermore, besides the CD169 marker, which is important for the analyses, other antibodies such as a marker for endothelial cells could also be used (**Figure 27**).

Another challenge with 3D images using light sheet microscopy is the acquisition of controls within the same settings, which is elementary for a subsequent analysis. With the Leica digital light sheet system (DLS), the system must be calibrated and aligned with the specimen before each acquisition. Usually, the sample is fixed in a special Petri dish at a certain height and surrounded with the mounting medium. By adjusting the petri dish and using a special mounting, it was possible to image both the treated sample and the control at the same time. This mounting technique enables verification of the mRNA reporter signal in a cleared organ at all and therefore represents an important step forward (**Figure 28**).

However, the background was still too high to allow a comparison with the data from the previously presented 2D spleen study. To reduce the final background signals in the spleen, a background subtraction was performed by measuring the autofluorescence of the tissue in a wavelength range where no signal was expected. The reference signal of the tissue autofluorescence was subsequently subtracted from the signals of the target wavelength in order to reduce background and noise. In 3D microscopy, such post-processing methods are often used and enable a significant improvement of the data (Gibbs et al., 2021). One of the major challenges in 3D

analysis, and especially in 3D microscopy, is the size of the data generated by these scans, which can quickly exceed several hundred gigabytes (Becker et al., 2022). As a result, high-performance computing systems are needed to process this data at all, which can take several days for a scan.

Since such high-performance systems are not available to most laboratories, this fact represents a considerable limitation. Therefore, a classical background subtraction procedure was used in this study, similar to the one described by (Hüpfel et al., 2021), but simplified and less resource intensive. With the help of this operation, the 3D data could be processed in such a way that a qualitative comparability with the signals generated in 2D was achieved (**Figure 29**). In a first analysis, the reporter signal could be colocalized with that of CD169-positive cells and the nuclear staining (**Figure 30**). The results indicate comparable values between 2D and 3D spleen samples (**Figure 18**), with small deviations mostly in terms of colocalization. With relatively simple procedural steps, data could also be generated from whole mount 3D samples, enabling quantitative analysis similar to that from 2D data, while at the same time containing more structural information.

4.3 Conclusion

The present work studied RNA-lipoplex mediated cell targeting in both *in vitro* and *in vivo* models. Direct application was analysed in 2D/3D mono and coculture of an early-stage melanoma model and revealed differences in colocalization between RNA reporter (eGFP) and different cell types. Systemic application *in vivo* demonstrated that colocalization of antigen presenting cells (APCs) with RNA reporter signal is possible in 2D slices as well as in 3D whole mount spleen. For whole mount scans of the spleen in the context of detection of RNA reporters such as eGFP or luciferase and colocalization with other markers, different tissue clearing techniques were tested. Based on these results, a method was developed that can be easily implemented with standard tools and is adapted for colocalization of lipid nanoparticle-based RNA therapeutics using RNA reporters from 3D scans. On the basis of the techniques presented in this study, further cell-specific markers could be used in future studies to identify additional cell populations involved in RNA-induced antigen presentation in the spleen or other modalities.

5 SUMMARY

Advanced mRNA therapeutics are not only emerging as vaccines, but are also being investigated for cancer therapy. The purpose of RNA lipoplexes (lipid nanoparticle-based RNA therapeutics) in tumor immunotherapy is to encode tumor-associated antigens and deliver this information to antigen-presenting cells (APCs). Besides the systemic application of RNA-LPX with the intention of targeting APCs in organs of the lymphatic system such as the spleen or lymph nodes, local applications in the direct tumor environment are also being studied.

The presented work describes the cell targeting of an RNA-lipoplex based therapeutic in different modalities. The focus is placed on *in vitro* and *in vivo* studies that reflect direct as well as systemic application. For data acquisition, microscopic analyses were used with a special focus on 3D microscopy. The studies revealed varying colocalizations with different cell types in the different study models.

In the described *in vitro* melanoma model, different cell type specific RNA reporter expression could be observed in classical 2D cell culture as well as in 3D mono and cocultures. The 2D cell cultures indicated an increased expression in the coculture compared to monocultures. In 3D monocultures, increased eGFP (RNA reporter) signal was detected in the SK-MEL 28 cells. In the 3D coculture system, a distribution within the spheroid could be depicted, where in addition to the CK 14 (basal keratinocytes) positive cells localised in the rim area, also eGFP was expressed in the spheroid nucleus.

Due to its central role in the secondary lymphatic system, the spleen was analysed as a target organ for systemic application, both in conventional 2D sections and in 3D whole mounts. Based on the results of the 2D sections, we found that both CD11c positive and CD169 positive cells show strong colocalizations with the RNA reporter signal. However, among APCs an increased colocalizations with CD169 positive cells could be detected.

For a comparison between classical 2D analyses and state-of-the-art 3D analyses, different techniques were tested and a method was adapted to the special

requirements of the target organ (spleen) and the detection of eGFP (RNA reporter). These studies have provided important insights into the strength of the tested tissue clearing techniques. Furthermore, colocalization between eGFP and CD169-positive cells in 3D provided a first insight into quantitative analyses like those from 2D tissue sections. The described method can be implemented using standard tools and thereby opens the way for future 3D studies of lipid nanoparticle-based RNA therapeutics.

6 ZUSAMMENFASSUNG

Moderne RNA-Therapeutika sind nicht nur als Impfstoffe von besonderem Interesse, sondern werden auch für die Krebstherapie untersucht. RNA-Lipoplexe (RNA-Therapeutika auf der Basis von Lipid-Nanopartikeln) sollen in der Tumor-Immuntherapie für tumorassoziierte Antigene kodieren und diese Information an Antigen-präsentierende Zellen (APCs) weitergeben. Neben der systemischen Anwendung von RNA-Lipoplexen um APCs in Organen des lymphatischen Systems wie der Milz oder den Lymphknoten anzusprechen, werden auch lokale Anwendungen in der direkten Tumorumgebung untersucht.

Die vorliegende Arbeit beschreibt das Zell-Targeting eines RNA-Lipoplex-basierten Therapeutikums in verschiedenen Modalitäten. Die mRNA kodiert dabei nicht für einen Arzneistoff, sondern für einen mikroskopisch gut nachweisbaren Fluoreszenzfarbstoff (Reporter; hier enhanced Green Fluorescent Protein eGFP oder Luciferase). In vitro und in vivo Studien sollen die direkte und die systemische Anwendung widerspiegeln. Zur Datenerfassung wurden mikroskopische Analysen mit besonderem Fokus auf 3D-Mikroskopie eingesetzt. Die Ergebnisse zeigen Kollokalisierungen des Reporters mit verschiedenen Zelltypen abhängig vom Studienmodell.

Im beschriebenen in vitro Melanommodell konnten verschiedene zelltypspezifische RNA-Reporterexpressionen sowohl in klassischer 2D-Zellkultur als auch in 3D-Mono- und Kokulturen verglichen werden. Die 2D-Zellkulturen zeigten eine erhöhte Reporterexpression in der Kokultur von Fibroblasten (CCD-1137Sk), Keratinozyten (HaCaT) und Melanozyten (SK-MEL 28) im Vergleich zu den Monokulturen mit den jeweiligen Zellen. In 3D-Monokulturen wurde das höchste Reportersignal in den SK-MEL 28-Zellen nachgewiesen. Im 3D-Kokultursystem konnte sowohl in den CK 14 (basale Keratinozyten) positiven Randsaumbereichen als auch im Sphäroidkern eine Expression des Reporters beobachtet werden.

Aufgrund ihrer zentralen Rolle im sekundären Lymphsystem wurde die Milz als Zielorgan für die systemische Anwendung sowohl in konventionellen 2D-Schnitten als auch im Ganzen als optisch geklärt Gewebe analysiert. Anhand der Ergebnisse der 2D-Schnitte konnte festgestellt werden, dass sowohl CD11c-positive dendritische Zelle

als auch CD169-positive Makrophagen starke Kollokationen mit dem Reportersignal aufweisen. Unter den untersuchten Markern für APC konnte jedoch eine verstärkte Kollokation mit CD169-positiven Zellen festgestellt werden.

Um einen Vergleich zwischen klassischen 2D-Analysen und modernen 3D-Analysen zu ermöglichen wurden verschiedene Gewebe-Clearing-Techniken getestet und eine Methode speziell an die Anforderungen des Zielorgans Milz und den Nachweis des RNA-Reporters angepasst. Diese Studien lieferten wichtige Erkenntnisse über die Vor- und Nachteile der getesteten Gewebe-Clearing-Techniken. Darüber hinaus gab die Kollokalisierung zwischen Reporter und CD169-positiven Zellen einen ersten Einblick in die Vergleichbarkeit mit Daten aus 2D-Gewebeschnitten.

Diese Methode, die mit Standardwerkzeugen umgesetzt werden kann, eröffnet somit den Weg für künftige 3D-Studien zur Lokalisation von RNA-Lipoplexen in größeren, strukturell intakten Gewebeproben.

7 REFERENCES

- Aarntzen, E. H. J. G., Schreibelt, G., Bol, K., Lesterhuis, W. J., Croockewit, A. J., Wilt, J. H. W. de, van Rossum, M. M., Blokk, W. A. M., Jacobs, J. F. M., Duiveman-de Boer, T., Schuurhuis, D. H., Mus, R., Thielemans, K., Vries, I. J. M. de, Figdor, C. G., Punt, C. J. A., & Adema, G. J. (2012). Vaccination with mRNA-electroporated dendritic cells induces robust tumor antigen-specific CD4⁺ and CD8⁺ T cells responses in stage III and IV melanoma patients. *Clinical Cancer Research : An Official Journal of the American Association for Cancer Research*, *18*(19), 5460–5470. <https://doi.org/10.1158/1078-0432.CCR-11-3368>
- Affandi, A. J., Grabowska, J., Olesek, K., Lopez Venegas, M., Barbaria, A., Rodríguez, E., Mulder, P. P. G., Pijffers, H. J., Ambrosini, M., Kalay, H., O'Toole, T., Zwart, E. S., Kazemier, G., Nazmi, K., Bikker, F. J., Stöckl, J., van den Eertwegh, A. J. M., Gruijl, T. D. de, Storm, G., . . . Haan, J. M. M. den (2020). Selective tumor antigen vaccine delivery to human CD169⁺ antigen-presenting cells using ganglioside-liposomes. *Proceedings of the National Academy of Sciences of the United States of America*, *117*(44), 27528–27539. <https://doi.org/10.1073/pnas.2006186117>
- A-Gonzalez, N., & Castrillo, A. (2018). Origin and specialization of splenic macrophages. *Cellular Immunology*, *330*, 151–158. <https://doi.org/10.1016/j.cellimm.2018.05.005>
- Alculumbre, S., Raieli, S., Hoffmann, C., Chelbi, R., Danlos, F.-X., & Soumelis, V. (2019). Plasmacytoid pre-dendritic cells (pDC): From molecular pathways to function and disease association. *Seminars in Cell & Developmental Biology*, *86*, 24–35. <https://doi.org/10.1016/j.semcdb.2018.02.014>
- Amreddy, N., Babu, A., Muralidharan, R., Panneerselvam, J., Srivastava, A., Ahmed, R., Mehta, M., Munshi, A., & Ramesh, R. (2018). Recent Advances in Nanoparticle-Based Cancer Drug and Gene Delivery. *Advances in Cancer Research*, *137*, 115–170. <https://doi.org/10.1016/bs.acr.2017.11.003>

- Ariel, P. (2017). A beginner's guide to tissue clearing. *The International Journal of Biochemistry & Cell Biology*, *84*, 35–39. <https://doi.org/10.1016/j.biocel.2016.12.009>
- Backer, R. A., Diener, N., & Clausen, B. E. (2019). Langerin+cd8+ Dendritic Cells in the Splenic Marginal Zone: Not So Marginal After All. *Frontiers in Immunology*, *10*, 741. <https://doi.org/10.3389/fimmu.2019.00741>
- Bahrami, B., Hojjat-Farsangi, M., Mohammadi, H., Anvari, E., Ghalamfarsa, G., Yousefi, M., & Jadidi-Niaragh, F. (2017). Nanoparticles and targeted drug delivery in cancer therapy. *Immunology Letters*, *190*, 64–83. <https://doi.org/10.1016/j.imlet.2017.07.015>
- Bartel, D. P. (2004). MicroRNAs. *Cell*, *116*(2), 281–297. [https://doi.org/10.1016/S0092-8674\(04\)00045-5](https://doi.org/10.1016/S0092-8674(04)00045-5)
- Beck, J. D., Reidenbach, D., Salomon, N., Sahin, U [Ugur], Türeci, Ö [Özlem], Vormehr, M., & Kranz, L. M. (2021). Mrna therapeutics in cancer immunotherapy. *Molecular Cancer*, *20*(1), 69. <https://doi.org/10.1186/s12943-021-01348-0>
- Becker, K., Saghafi, S., Pende, M., Hahn, C., & Dodt, H. U. (2022). Visualizing minute details in light-sheet and confocal microscopy data by combining 3D rolling ball filtering and deconvolution. *Journal of Biophotonics*, *15*(2), e202100290. <https://doi.org/10.1002/jbio.202100290>
- Black, K. C. L., Wang, Y [Yucai], Luehmann, H. P., Cai, X., Xing, W., Pang, B., Zhao, Y., Cutler, C. S., Wang, L. V., Liu, Y [Yongjian], & Xia, Y. (2014). Radioactive ¹⁹⁸Au-doped nanostructures with different shapes for in vivo analyses of their biodistribution, tumor uptake, and intratumoral distribution. *ACS Nano*, *8*(5), 4385–4394. <https://doi.org/10.1021/nn406258m>
- Blanco, E., Shen, H [Haifa], & Ferrari, M. (2015). Principles of nanoparticle design for overcoming biological barriers to drug delivery. *Nature Biotechnology*, *33*(9), 941–951. <https://doi.org/10.1038/nbt.3330>
- Bronte, V., & Pittet, M. J. (2013). The spleen in local and systemic regulation of immunity. *Immunity*, *39*(5), 806–818. <https://doi.org/10.1016/j.immuni.2013.10.010>

- Burnett, J. C., & Rossi, J. J. (2012). Rna-based therapeutics: Current progress and future prospects. *Chemistry & Biology*, 19(1), 60–71. <https://doi.org/10.1016/j.chembiol.2011.12.008>
- Carita, A. C., Eloy, J. O., Chorilli, M., Lee, R. J., & Leonardi, G. R. (2018). Recent Advances and Perspectives in Liposomes for Cutaneous Drug Delivery. *Current Medicinal Chemistry*, 25(5), 606–635. <https://doi.org/10.2174/0929867324666171009120154>
- Carmeliet, P., & Jain, R. K. (2000). Angiogenesis in cancer and other diseases. *Nature*, 407(6801), 249–257. <https://doi.org/10.1038/35025220>
- Cerutti, A., Cols, M., & Puga, I. (2013). Marginal zone B cells: Virtues of innate-like antibody-producing lymphocytes. *Nature Reviews. Immunology*, 13(2), 118–132. <https://doi.org/10.1038/nri3383>
- Chabner, B. A., & Roberts, T. G. (2005). Timeline: Chemotherapy and the war on cancer. *Nature Reviews. Cancer*, 5(1), 65–72. <https://doi.org/10.1038/nrc1529>
- Chatterjee, K., Pratiwi, F. W., Wu, F. C. M., Chen, P., & Chen, B.-C. (2018). Recent Progress in Light Sheet Microscopy for Biological Applications. *Applied Spectroscopy*, 72(8), 1137–1169. <https://doi.org/10.1177/0003702818778851>
- Chen, B., Dragomir, M. P., Yang, C., Li, Q., Horst, D., & Calin, G. A. (2022). Targeting non-coding RNAs to overcome cancer therapy resistance. *Signal Transduction and Targeted Therapy*, 7(1), 121. <https://doi.org/10.1038/s41392-022-00975-3>
- Chung, K., & Deisseroth, K. (2013). Clarity for mapping the nervous system. *Nature Methods*, 10(6), 508–513. <https://doi.org/10.1038/nmeth.2481>
- Coulie, P. G., van den Eynde, B. J., van der Bruggen, P., & Boon, T. (2014). Tumour antigens recognized by T lymphocytes: At the core of cancer immunotherapy. *Nature Reviews Cancer*, 14(2), 135–146. <https://doi.org/10.1038/nrc3670>
- Damase, T. R., Sukhovshin, R., Boada, C., Taraballi, F., Pettigrew, R. I., & Cooke, J. P. (2021). The Limitless Future of RNA Therapeutics. *Frontiers in Bioengineering and Biotechnology*, 9, 628137. <https://doi.org/10.3389/fbioe.2021.628137>
- Danhier, F., Feron, O., & Préat, V. (2010). To exploit the tumor microenvironment: Passive and active tumor targeting of nanocarriers for anti-cancer drug delivery.

- Journal of Controlled Release : Official Journal of the Controlled Release Society*, 148(2), 135–146. <https://doi.org/10.1016/j.jconrel.2010.08.027>
- Deng, Y [Yudi], Zhang, X., Shen, H [Haibin], He, Q., Wu, Z., Liao, W., & Yuan, M. (2019). Application of the Nano-Drug Delivery System in Treatment of Cardiovascular Diseases. *Frontiers in Bioengineering and Biotechnology*, 7, 489. <https://doi.org/10.3389/fbioe.2019.00489>
- Dey, A. K., Nougarede, A., Clément, F., Fournier, C., Jouvin-Marche, E., Escudé, M., Jary, D., Navarro, F. P., & Marche, P. N. (2021). Tuning the Immunostimulation Properties of Cationic Lipid Nanocarriers for Nucleic Acid Delivery. *Frontiers in Immunology*, 12, 722411. <https://doi.org/10.3389/fimmu.2021.722411>
- Dhungel, P., Cantu, F., Hernandez, C., & Yang, Z [Zhilong] (2019). In Vitro Transcribed RNA-based Luciferase Reporter Assay to Study Translation Regulation in Poxvirus-infected Cells. *Journal of Visualized Experiments : JoVE*. Advance online publication. <https://doi.org/10.3791/59626>
- Diken, M [M.], Kreiter, S [S.], Selmi, A [A.], Britten, C. M [C. M.], Huber, C [C.], Türeci, Ö [Ö.], & Sahin, U [U.] (2011). Selective uptake of naked vaccine RNA by dendritic cells is driven by macropinocytosis and abrogated upon DC maturation. *Gene Therapy*, 18(7), 702–708. <https://doi.org/10.1038/gt.2011.17>
- Diken, M [Mustafa], Kranz, L. M., Kreiter, S [Sebastian], & Sahin, U [Ugur] (2017). Mrna: A Versatile Molecule for Cancer Vaccines. *Current Issues in Molecular Biology*, 22, 113–128. <https://doi.org/10.21775/cimb.022.113>
- Dorsett, Y., & Tuschl, T. (2004). Sirnas: Applications in functional genomics and potential as therapeutics. *Nature Reviews. Drug Discovery*, 3(4), 318–329. <https://doi.org/10.1038/nrd1345>
- Dunne, L. W., Huang, Z., Meng, W., Fan, X., Zhang, N., Zhang, Q., & An, Z. (2014). Human decellularized adipose tissue scaffold as a model for breast cancer cell growth and drug treatments. *Biomaterials*, 35(18), 4940–4949. <https://doi.org/10.1016/j.biomaterials.2014.03.003>
- Duval, K., Grover, H., Han, L.-H., Mou, Y., Pegoraro, A. F., Fredberg, J., & Chen, Z. (2017). Modeling Physiological Events in 2D vs. 3d Cell Culture. *Physiology (Bethesda, Md.)*, 32(4), 266–277. <https://doi.org/10.1152/physiol.00036.2016>

- Ertürk, A., Becker, K., Jährling, N., Mauch, C. P., Hojer, C. D., Egen, J. G., Hellal, F., Bradke, F., Sheng, M., & Dodt, H.-U. (2012). Three-dimensional imaging of solvent-cleared organs using 3DISCO. *Nature Protocols*, 7(11), 1983–1995. <https://doi.org/10.1038/nprot.2012.119>
- Esch, E. W., Bahinski, A., & Huh, D. (2015). Organs-on-chips at the frontiers of drug discovery. *Nature Reviews. Drug Discovery*, 14(4), 248–260. <https://doi.org/10.1038/nrd4539>
- Fang, R. H., Kroll, A. V., Gao, W., & Zhang, L [Liangfang] (2018). Cell Membrane Coating Nanotechnology. *Advanced Materials (Deerfield Beach, Fla.)*, 30(23), e1706759. <https://doi.org/10.1002/adma.201706759>
- Fellmann, C., & Lowe, S. W. (2014). Stable RNA interference rules for silencing. *Nature Cell Biology*, 16(1), 10–18. <https://doi.org/10.1038/ncb2895>
- Fire, A., Xu, S., Montgomery, M. K., Kostas, S. A., Driver, S. E., & Mello, C. C. (1998). Potent and specific genetic interference by double-stranded RNA in *Caenorhabditis elegans*. *Nature*, 391(6669), 806–811. <https://doi.org/10.1038/35888>
- Fischer, R. S., Wu, Y., Kanchanawong, P., Shroff, H., & Waterman, C. M. (2011). Microscopy in 3D: A biologist's toolbox. *Trends in Cell Biology*, 21(12), 682–691. <https://doi.org/10.1016/j.tcb.2011.09.008>
- Fonseca-Santos, B., Gremião, M. P. D., & Chorilli, M. (2015). Nanotechnology-based drug delivery systems for the treatment of Alzheimer's disease. *International Journal of Nanomedicine*, 10, 4981–5003. <https://doi.org/10.2147/IJN.S87148>
- Gary E. Carver, Sarah A. Locknar, William A. Morrison, & Daniel L. Farkas (2013). High-speed multispectral confocal imaging. In (pp. 142–149). SPIE. <https://doi.org/10.1117/12.2001883>
- Gaspar, R., Coelho, F., & Silva, B. F. B. (2020). Lipid-Nucleic Acid Complexes: Physicochemical Aspects and Prospects for Cancer Treatment. *Molecules (Basel, Switzerland)*, 25(21). <https://doi.org/10.3390/molecules25215006>
- Gentric, G., & Mehta-Grigoriou, F. (2021). Tumor Cells and Cancer-Associated Fibroblasts: An Updated Metabolic Perspective. *Cancers*, 13(3). <https://doi.org/10.3390/cancers13030399>

- Gibbs, H. C., Mota, S. M., Hart, N. A., Min, S. W., Vernino, A. O., Pritchard, A. L., Sen, A., Vitha, S., Sarasamma, S., McIntosh, A. L., Yeh, A. T., Lekven, A. C., McCreedy, D. A., Maitland, K. C., & Perez, L. M. (2021). Navigating the Light-Sheet Image Analysis Software Landscape: Concepts for Driving Cohesion From Data Acquisition to Analysis. *Frontiers in Cell and Developmental Biology*, 9, 739079. <https://doi.org/10.3389/fcell.2021.739079>
- Grabbe, S., Haas, H., Diken, M [Mustafa], Kranz, L. M., Langguth, P., & Sahin, U [Ugur] (2016). Translating nanoparticulate-personalized cancer vaccines into clinical applications: Case study with RNA-lipoplexes for the treatment of melanoma. *Nanomedicine (London, England)*, 11(20), 2723–2734. <https://doi.org/10.2217/nnm-2016-0275>
- Grabowska, J., Lopez-Venegas, M. A., Affandi, A. J., & Haan, J. M. M. den (2018). Cd169+ Macrophages Capture and Dendritic Cells Instruct: The Interplay of the Gatekeeper and the General of the Immune System. *Frontiers in Immunology*, 9, 2472. <https://doi.org/10.3389/fimmu.2018.02472>
- Groot, A. M. de, Thanki, K., Gangloff, M., Falkenberg, E., Zeng, X., van Bijnen, D. C. J., van Eden, W., Franzyk, H., Nielsen, H. M., Broere, F., Gay, N. J., Foged, C., & Sijts, A. J. A. M. (2018). Immunogenicity Testing of Lipidoids In Vitro and In Silico: Modulating Lipidoid-Mediated TLR4 Activation by Nanoparticle Design. *Molecular Therapy. Nucleic Acids*, 11, 159–169. <https://doi.org/10.1016/j.omtn.2018.02.003>
- Guerrier-Takada, C., Gardiner, K., Marsh, T., Pace, N., & Altman, S. (1983). The RNA moiety of ribonuclease P is the catalytic subunit of the enzyme. *Cell*, 35(3), 849–857. [https://doi.org/10.1016/0092-8674\(83\)90117-4](https://doi.org/10.1016/0092-8674(83)90117-4)
- Guevara, M. L., Persano, F., & Persano, S. (2020). Advances in Lipid Nanoparticles for mRNA-Based Cancer Immunotherapy. *Frontiers in Chemistry*, 8, 589959. <https://doi.org/10.3389/fchem.2020.589959>
- Gupta, P., Garcia, E., Sarkar, A., Kapoor, S., Rafiq, K., Chand, H. S., & Jayant, R. D. (2019). Nanoparticle Based Treatment for Cardiovascular Diseases. *Cardiovascular & Hematological Disorders Drug Targets*, 19(1), 33–44. <https://doi.org/10.2174/1871529X18666180508113253>

- Haan, J. M. M. den, Arens, R., & van Zelm, M. C. (2014). The activation of the adaptive immune system: Cross-talk between antigen-presenting cells, T cells and B cells. *Immunology Letters*, *162*(2 Pt B), 103–112. <https://doi.org/10.1016/j.imlet.2014.10.011>
- Habbeddine, M., Verthuy, C., Rastoin, O., Chasson, L., Bebien, M., Bajenoff, M., Adriouch, S., Haan, J. M. M. den, Penninger, J. M., & Lawrence, T. (2017). Receptor Activator of NF- κ B Orchestrates Activation of Antiviral Memory CD8 T Cells in the Spleen Marginal Zone. *Cell Reports*, *21*(9), 2515–2527. <https://doi.org/10.1016/j.celrep.2017.10.111>
- Hama, H., Hioki, H., Namiki, K., Hoshida, T., Kurokawa, H., Ishidate, F., Kaneko, T., Akagi, T., Saito, T., Saido, T., & Miyawaki, A. (2015). Scales: An optical clearing palette for biological imaging. *Nature Neuroscience*, *18*(10), 1518–1529. <https://doi.org/10.1038/nn.4107>
- Hensel, J. A., Khattar, V., Ashton, R., & Ponnazhagan, S. (2019). Characterization of immune cell subtypes in three commonly used mouse strains reveals gender and strain-specific variations. *Laboratory Investigation*, *99*(1), 93–106. <https://doi.org/10.1038/s41374-018-0137-1>
- Hillion, S., Arleevskaya, M. I., Blanco, P., Bordron, A., Brooks, W. H., Cesbron, J. Y., Kaveri, S., Vivier, E., & Renaudineau, Y. (2020). The Innate Part of the Adaptive Immune System. *Clinical Reviews in Allergy & Immunology*, *58*(2), 151–154. <https://doi.org/10.1007/s12016-019-08740-1>
- Hirano, T., Satow, R., Kato, A., Tamura, M., Murayama, Y., Saya, H., Kojima, H., Nagano, T., Okabe, T., & Fukami, K. (2013). Identification of novel small compounds that restore E-cadherin expression and inhibit tumor cell motility and invasiveness. *Biochemical Pharmacology*, *86*(10), 1419–1429. <https://doi.org/10.1016/j.bcp.2013.09.001>
- Hofmann, J., Gadjalova, I., Mishra, R., Ruland, J., & Keppler, S. J. (2020). Efficient Tissue Clearing and Multi-Organ Volumetric Imaging Enable Quantitative Visualization of Sparse Immune Cell Populations During Inflammation. *Frontiers in Immunology*, *11*, 599495. <https://doi.org/10.3389/fimmu.2020.599495>

- Hou, X., Zaks, T., Langer, R., & Dong, Y. (2021). Lipid nanoparticles for mRNA delivery. *Nature Reviews. Materials*, 6(12), 1078–1094. <https://doi.org/10.1038/s41578-021-00358-0>
- Huisken, J., Swoger, J., Del Bene, F., Wittbrodt, J., & Stelzer, E. H. K. (2004). Optical sectioning deep inside live embryos by selective plane illumination microscopy. *Science (New York, N.Y.)*, 305(5686), 1007–1009. <https://doi.org/10.1126/science.1100035>
- Hüpfel, M., Yu Kobitski, A., Zhang, W., & Nienhaus, G. U. (2021). Wavelet-based background and noise subtraction for fluorescence microscopy images. *Biomedical Optics Express*, 12(2), 969–980. <https://doi.org/10.1364/BOE.413181>
- Imamura, Y., Mukohara, T., Shimono, Y., Funakoshi, Y., Chayahara, N., Toyoda, M., Kiyota, N., Takao, S., Kono, S., Nakatsura, T., & Minami, H. (2015). Comparison of 2D- and 3D-culture models as drug-testing platforms in breast cancer. *Oncology Reports*, 33(4), 1837–1843. <https://doi.org/10.3892/or.2015.3767>
- Immig, K., Gericke, M., Menzel, F., Merz, F., Krueger, M., Schiefenhövel, F., Lösche, A., Jäger, K., Hanisch, U.-K., Biber, K., & Bechmann, I. (2015). Cd11c-positive cells from brain, spleen, lung, and liver exhibit site-specific immune phenotypes and plastically adapt to new environments. *Glia*, 63(4), 611–625. <https://doi.org/10.1002/glia.22771>
- Jayasena, S. D. (1999). Aptamers: An emerging class of molecules that rival antibodies in diagnostics. *Clinical Chemistry*, 45(9), 1628–1650.
- Jensen, C., & Teng, Y. (2020). Is It Time to Start Transitioning From 2D to 3D Cell Culture? *Frontiers in Molecular Biosciences*, 7, 33. <https://doi.org/10.3389/fmolb.2020.00033>
- Jiang, Y., Huo, S., Hardie, J., Liang, X.-J., & Rotello, V. M. (2016). Progress and perspective of inorganic nanoparticle-based siRNA delivery systems. *Expert Opinion on Drug Delivery*, 13(4), 547–559. <https://doi.org/10.1517/17425247.2016.1134486>

- Johnsen, & Widder (1999). The physical basis of transparency in biological tissue: Ultrastructure and the minimization of light scattering. *Journal of Theoretical Biology*, 199(2), 181–198. <https://doi.org/10.1006/jtbi.1999.0948>
- Junt, T., Moseman, E. A., Iannacone, M., Massberg, S., Lang, P. A., Boes, M., Fink, K., Henrickson, S. E., Shayakhmetov, D. M., Di Paolo, N. C., van Rooijen, N., Mempel, T. R., Whelan, S. P., & Andrian, U. H. von (2007). Subcapsular sinus macrophages in lymph nodes clear lymph-borne viruses and present them to antiviral B cells. *Nature*, 450(7166), 110–114. <https://doi.org/10.1038/nature06287>
- Kamaly, N., Xiao, Z., Valencia, P. M., Radovic-Moreno, A. F., & Farokhzad, O. C. (2012). Targeted polymeric therapeutic nanoparticles: Design, development and clinical translation. *Chemical Society Reviews*, 41(7), 2971–3010. <https://doi.org/10.1039/c2cs15344k>
- Kambayashi, T., & Laufer, T. M. (2014). Atypical MHC class II-expressing antigen-presenting cells: Can anything replace a dendritic cell? *Nature Reviews Immunology*, 14(11), 719–730. <https://doi.org/10.1038/nri3754>
- Keller, P. J., Schmidt, A. D., Santella, A., Khairy, K., Bao, Z., Wittbrodt, J., & Stelzer, E. H. K. (2010). Fast, high-contrast imaging of animal development with scanned light sheet-based structured-illumination microscopy. *Nature Methods*, 7(8), 637–642. <https://doi.org/10.1038/nmeth.1476>
- Keller, P. J., Schmidt, A. D., Wittbrodt, J., & Stelzer, E. H. K. (2008). Reconstruction of zebrafish early embryonic development by scanned light sheet microscopy. *Science (New York, N.Y.)*, 322(5904), 1065–1069. <https://doi.org/10.1126/science.1162493>
- Keller, P. J., & Stelzer, E. H. K. (2008). Quantitative in vivo imaging of entire embryos with Digital Scanned Laser Light Sheet Fluorescence Microscopy. *Current Opinion in Neurobiology*, 18(6), 624–632. <https://doi.org/10.1016/j.conb.2009.03.008>
- Khafaji, M., Zamani, M., Golizadeh, M., & Bavi, O. (2019). Inorganic nanomaterials for chemo/photothermal therapy: A promising horizon on effective cancer treatment. *Biophysical Reviews*, 11(3), 335–352. <https://doi.org/10.1007/s12551-019-00532-3>

- Klicks, J., Maßlo, C., Kluth, A., Rudolf, R., & Hafner, M. (2019). A novel spheroid-based co-culture model mimics loss of keratinocyte differentiation, melanoma cell invasion, and drug-induced selection of ABCB5-expressing cells. *BMC Cancer*, *19*(1), 402. <https://doi.org/10.1186/s12885-019-5606-4>
- Köster, I., & Haas, P. (2015). Light Sheet Microscopy Turned Vertically. *Optik & Photonik*, *10*(4), 39–43. <https://doi.org/10.1002/opph.201500028>
- Kranz, L. M., Diken, M [Mustafa], Haas, H., Kreiter, S [Sebastian], Loquai, C., Reuter, K. C., Meng, M., Fritz, D., Vascotto, F., Hefesha, H., Grunwitz, C., Vormehr, M., Hüsemann, Y., Selmi, A [Abderraouf], Kuhn, A. N., Buck, J., Derhovannessian, E., Rae, R., Attig, S., . . . Sahin, U [Ugur] (2016). Systemic RNA delivery to dendritic cells exploits antiviral defence for cancer immunotherapy. *Nature*, *534*(7607), 396–401. <https://doi.org/10.1038/nature18300>
- Kreiter, S [Sebastian], Selmi, A [Abderraouf], Diken, M [Mustafa], Koslowski, M., Britten, C. M [Cedrik M.], Huber, C [Christoph], Türeci, O., & Sahin, U [Ugur] (2010). Intranodal vaccination with naked antigen-encoding RNA elicits potent prophylactic and therapeutic antitumoral immunity. *Cancer Research*, *70*(22), 9031–9040. <https://doi.org/10.1158/0008-5472.CAN-10-0699>
- Kruger, K., Grabowski, P. J., Zaug, A. J., Sands, J., Gottschling, D. E., & Cech, T. R. (1982). Self-splicing RNA: Autoexcision and autocyclization of the ribosomal RNA intervening sequence of tetrahymena. *Cell*, *31*(1), 147–157. [https://doi.org/10.1016/0092-8674\(82\)90414-7](https://doi.org/10.1016/0092-8674(82)90414-7)
- Langhans, S. A. (2018). Three-Dimensional in Vitro Cell Culture Models in Drug Discovery and Drug Repositioning. *Frontiers in Pharmacology*, *9*, 6. <https://doi.org/10.3389/fphar.2018.00006>
- Lewis, S. M., Williams, A., & Eisenbarth, S. C. (2019). Structure and function of the immune system in the spleen. *Science Immunology*, *4*(33). <https://doi.org/10.1126/sciimmunol.aau6085>
- Li, Y., & Kiledjian, M. (2010). Regulation of mRNA decapping. *Wiley Interdisciplinary Reviews. RNA*, *1*(2), 253–265. <https://doi.org/10.1002/wrna.15>
- Lim, E.-K., Chung, B. H., & Chung, S. J. (2018). Recent Advances in pH-Sensitive Polymeric Nanoparticles for Smart Drug Delivery in Cancer Therapy. *Current*

- Drug Targets*, 19(4), 300–317.
<https://doi.org/10.2174/1389450117666160602202339>
- Lin, X. P., Mintern, J. D., & Gleeson, P. A. (2020). Macropinocytosis in Different Cell Types: Similarities and Differences. *Membranes*, 10(8).
<https://doi.org/10.3390/membranes10080177>
- Liu, F.-S. (2009). Mechanisms of Chemotherapeutic Drug Resistance in Cancer Therapy—A Quick Review. *Taiwanese Journal of Obstetrics and Gynecology*, 48(3), 239–244. [https://doi.org/10.1016/S1028-4559\(09\)60296-5](https://doi.org/10.1016/S1028-4559(09)60296-5)
- Lv, D., Hu, Z., Lu, L., Lu, H., & Xu, X. (2017). Three-dimensional cell culture: A powerful tool in tumor research and drug discovery. *Oncology Letters*, 14(6), 6999–7010. <https://doi.org/10.3892/ol.2017.7134>
- Maeda, H. (2001). The enhanced permeability and retention (EPR) effect in tumor vasculature: the key role of tumor-selective macromolecular drug targeting. *Advances in Enzyme Regulation*, 41(1), 189–207.
[https://doi.org/10.1016/S0065-2571\(00\)00013-3](https://doi.org/10.1016/S0065-2571(00)00013-3)
- Mandal, S., Zhou, Y [You], Shibata, A., & Destache, C. J. (2015). Confocal fluorescence microscopy: An ultra-sensitive tool used to evaluate intracellular antiretroviral nano-drug delivery in HeLa cells. *AIP Advances*, 5(8), 84803.
<https://doi.org/10.1063/1.4926584>
- Maria, O. M., Maria, O., Liu, Y [Younan], Komarova, S. V., & Tran, S. D. (2011). Matrigel improves functional properties of human submandibular salivary gland cell line. *The International Journal of Biochemistry & Cell Biology*, 43(4), 622–631. <https://doi.org/10.1016/j.biocel.2011.01.001>
- Mauger, D. M., Cabral, B. J., Presnyak, V., Su, S. V., Reid, D. W., Goodman, B., Link, K., Khatwani, N., Reynders, J., Moore, M. J., & McFadyen, I. J. (2019). Mrna structure regulates protein expression through changes in functional half-life. *Proceedings of the National Academy of Sciences of the United States of America*, 116(48), 24075–24083. <https://doi.org/10.1073/pnas.1908052116>
- Mebius, R. E., & Kraal, G. (2005). Structure and function of the spleen. *Nature Reviews. Immunology*, 5(8), 606–616. <https://doi.org/10.1038/nri1669>
- Melnikova, I. (2007). Rna-based therapies. *Nature Reviews. Drug Discovery*, 6(11), 863–864. <https://doi.org/10.1038/nrd2443>

- Miao, L., Zhang, Y., & Huang, L. (2021). Mrna vaccine for cancer immunotherapy. *Molecular Cancer*, *20*(1), 41. <https://doi.org/10.1186/s12943-021-01335-5>
- Mitchell, M. J., Billingsley, M. M., Haley, R. M., Wechsler, M. E., Peppas, N. A., & Langer, R. (2021). Engineering precision nanoparticles for drug delivery. *Nature Reviews. Drug Discovery*, *20*(2), 101–124. <https://doi.org/10.1038/s41573-020-0090-8>
- Mottaghitlab, F., Farokhi, M., Fatahi, Y., Atyabi, F., & Dinarvand, R. (2019). New insights into designing hybrid nanoparticles for lung cancer: Diagnosis and treatment. *Journal of Controlled Release : Official Journal of the Controlled Release Society*, *295*, 250–267. <https://doi.org/10.1016/j.jconrel.2019.01.009>
- Neri, L. M., Martelli, A. M., Previati, M., Valmori, A., & Capitani, S. (1992). From two dimensional (2D) to three dimensional (3D) analysis by confocal microscopy. *Liver*, *12*(4 Pt 2), 268–279. <https://doi.org/10.1111/j.1600-0676.1992.tb01060.x>
- Nolte, M. A., Hoen, E. N. M. 't, van Stijn, A., Kraal, G., & Mebius, R. E. (2000). Isolation of the intact white pulp. Quantitative and qualitative analysis of the cellular composition of the splenic compartments. *European Journal of Immunology*, *30*(2), 626–634. [https://doi.org/10.1002/1521-4141\(200002\)30:2<626::AID-IMMU626>3.0.CO;2-H](https://doi.org/10.1002/1521-4141(200002)30:2<626::AID-IMMU626>3.0.CO;2-H)
- Norbury, C. C., Hewlett, L. J., Prescott, A. R., Shastri, N., & Watts, C. (1995). Class I MHC presentation of exogenous soluble antigen via macropinocytosis in bone marrow macrophages. *Immunity*, *3*(6), 783–791. [https://doi.org/10.1016/1074-7613\(95\)90067-5](https://doi.org/10.1016/1074-7613(95)90067-5)
- Nürnberg, E., Vitacolonna, M., Klicks, J., Molitor, E. von, Cesetti, T., Keller, F., Bruch, R., Ertongur-Fauth, T., Riedel, K., Scholz, P., Lau, T., Schneider, R., Meier, J., Hafner, M., & Rudolf, R. (2020). Routine Optical Clearing of 3D-Cell Cultures: Simplicity Forward. *Frontiers in Molecular Biosciences*, *7*, 20. <https://doi.org/10.3389/fmolb.2020.00020>
- Pageau, S. C., Sazonova, O. V., Wong, J. Y., Soto, A. M., & Sonnenschein, C. (2011). The effect of stromal components on the modulation of the phenotype of human bronchial epithelial cells in 3D culture. *Biomaterials*, *32*(29), 7169–7180. <https://doi.org/10.1016/j.biomaterials.2011.06.017>

- Paknezhad, M., Loh, S. Y. M., Choudhury, Y., Koh, V. K. C., Yong, T. T. K., Tan, H. S., Kaneshvaran, R., Tan, P. H., Peng, J. Y. S., Yu, W., Tan, Y. B., Loy, Y. Z., Tan, M.-H., & Lee, H. K. (2020). Regional registration of whole slide image stacks containing major histological artifacts. *BMC Bioinformatics*, *21*(1), 558. <https://doi.org/10.1186/s12859-020-03907-6>
- Pandey, S. K., Paul, A., Shteinifer-Kuzmine, A., Zalk, R., Bunz, U., & Shoshan-Barmatz, V. (2021). Smac/diablo controls proliferation of cancer cells by regulating phosphatidylethanolamine synthesis. *Molecular Oncology*. Advance online publication. <https://doi.org/10.1002/1878-0261.12959>
- Paris, J. L., Coelho, F., Teixeira, A., Diéguez, L., Silva, B. F. B., & Abalde-Cela, S. (2020). In Vitro Evaluation of Lipopolyplexes for Gene Transfection: Comparing 2D, 3D and Microdroplet-Enabled Cell Culture. *Molecules (Basel, Switzerland)*, *25*(14). <https://doi.org/10.3390/molecules25143277>
- Park, H., Yang, J., Lee, J., Haam, S., Choi, I.-H., & Yoo, K.-H. (2009). Multifunctional nanoparticles for combined doxorubicin and photothermal treatments. *ACS Nano*, *3*(10), 2919–2926. <https://doi.org/10.1021/nn900215k>
- Park, Y.-G., Sohn, C. H., Chen, R., McCue, M., Yun, D. H., Drummond, G. T., Ku, T., Evans, N. B., Oak, H. C., Trieu, W., Choi, H., Jin, X., Lilascharoen, V., Wang, J., Truttman, M. C., Qi, H. W., Ploegh, H. L., Golub, T. R., Chen, S.-C., . . . Chung, K. (2018). Protection of tissue physicochemical properties using polyfunctional crosslinkers. *Nature Biotechnology*. Advance online publication. <https://doi.org/10.1038/nbt.4281>
- Parodi, A., Quattrocchi, N., van de Ven, A. L., Chiappini, C., Evangelopoulos, M., Martinez, J. O., Brown, B. S., Khaled, S. Z., Yazdi, I. K., Enzo, M. V., Isenhardt, L., Ferrari, M., & Tasciotti, E. (2013). Synthetic nanoparticles functionalized with biomimetic leukocyte membranes possess cell-like functions. *Nature Nanotechnology*, *8*(1), 61–68. <https://doi.org/10.1038/nnano.2012.212>
- Pastor, F., Berraondo, P., Etxeberria, I., Frederick, J., Sahin, U [Ugur], Gilboa, E., & Melero, I. (2018). An RNA toolbox for cancer immunotherapy. *Nature Reviews. Drug Discovery*, *17*(10), 751–767. <https://doi.org/10.1038/nrd.2018.132>

- Paunovska, K., Loughrey, D., & Dahlman, J. E. (2022). Drug delivery systems for RNA therapeutics. *Nature Reviews. Genetics*, 23(5), 265–280. <https://doi.org/10.1038/s41576-021-00439-4>
- Pereira-Nunes, A., Afonso, J., Granja, S., & Baltazar, F. (2020). Lactate and Lactate Transporters as Key Players in the Maintenance of the Warburg Effect. *Advances in Experimental Medicine and Biology*, 1219, 51–74. https://doi.org/10.1007/978-3-030-34025-4_3
- Pérez-Herrero, E., & Fernández-Medarde, A. (2015). Advanced targeted therapies in cancer: Drug nanocarriers, the future of chemotherapy. *European Journal of Pharmaceutics and Biopharmaceutics : Official Journal of Arbeitsgemeinschaft Fur Pharmazeutische Verfahrenstechnik E.V*, 93, 52–79. <https://doi.org/10.1016/j.ejpb.2015.03.018>
- Polack, F. P., Thomas, S. J., Kitchin, N., Absalon, J., Gurtman, A., Lockhart, S., Perez, J. L., Pérez Marc, G., Moreira, E. D., Zerbini, C., Bailey, R., Swanson, K. A., Roychoudhury, S., Koury, K., Li, P., Kalina, W. V., Cooper, D., Frenck, R. W., Hammitt, L. L., . . . Gruber, W. C. (2020). Safety and Efficacy of the BNT162b2 mRNA Covid-19 Vaccine. *The New England Journal of Medicine*, 383(27), 2603–2615. <https://doi.org/10.1056/NEJMoa2034577>
- Raina, M., & Ibbá, M. (2014). Trnas as regulators of biological processes. *Frontiers in Genetics*, 5, 171. <https://doi.org/10.3389/fgene.2014.00171>
- Ramachandran, S., Satapathy, S. R., & Dutta, T. (2022). Delivery Strategies for mRNA Vaccines. *Pharmaceutical Medicine*, 36(1), 11–20. <https://doi.org/10.1007/s40290-021-00417-5>
- Reynaud, E. G., Peychl, J., Huisken, J., & Tomancak, P. (2015). Guide to light-sheet microscopy for adventurous biologists. *Nature Methods*, 12(1), 30–34. <https://doi.org/10.1038/nmeth.3222>
- Ricci, P., Gavryusev, V., Müllenbroich, C., Turrini, L., Vito, G. de, Silvestri, L., Sancataldo, G., & Pavone, F. S. (2022). Removing striping artifacts in light-sheet fluorescence microscopy: A review. *Progress in Biophysics and Molecular Biology*, 168, 52–65. <https://doi.org/10.1016/j.pbiomolbio.2021.07.003>

- Rich, A., & Davies, D. R. (1956). A NEW TWO STRANDED HELICAL STRUCTURE: POLYADENYLIC ACID AND POLYURIDYLIC ACID. *Journal of the American Chemical Society*, *78*(14), 3548–3549. <https://doi.org/10.1021/ja01595a086>
- Richardson, D. S., Guan, W., Matsumoto, K., Pan, C., Chung, K., Ertürk, A., Ueda, H. R., & Lichtman, J. W. (2021). Tissue CLEARING. *Nature Reviews Methods Primers*, *1*(1), 1–24. <https://doi.org/10.1038/s43586-021-00080-9>
- Rosigkeit, S., Meng, M., Grunwitz, C., Gomes, P., Kreft, A., Hayduk, N., Heck, R., Pickert, G., Ziegler, K., Abassi, Y., Röder, J., Kaps, L., Vascotto, F., Beisert, T., Witzel, S., Kuhn, A., Diken, M [Mustafa], Schuppan, D., Sahin, U [Ugur], . . . Bockamp, E. (2018). Monitoring Translation Activity of mRNA-Loaded Nanoparticles in Mice. *Molecular Pharmaceutics*, *15*(9), 3909–3919. <https://doi.org/10.1021/acs.molpharmaceut.8b00370>
- Sahay, G., Alakhova, D. Y., & Kabanov, A. V. (2010). Endocytosis of nanomedicines. *Journal of Controlled Release : Official Journal of the Controlled Release Society*, *145*(3), 182–195. <https://doi.org/10.1016/j.jconrel.2010.01.036>
- Sahin, U [Ugur], Derhovanessian, E., Miller, M., Kloke, B.-P., Simon, P., Löwer, M., Bukur, V., Tadmor, A. D., Luxemburger, U., Schrörs, B., Omokoko, T., Vormehr, M., Albrecht, C., Paruzynski, A., Kuhn, A. N., Buck, J., Heesch, S., Schreeb, K. H., Müller, F., . . . Türeci, Ö [Özlem] (2017). Personalized RNA mutanome vaccines mobilize poly-specific therapeutic immunity against cancer. *Nature*, *547*(7662), 222–226. <https://doi.org/10.1038/nature23003>
- Sahin, U [Ugur], Karikó, K., & Türeci, Ö [Özlem] (2014). Mrna-based therapeutics--developing a new class of drugs. *Nature Reviews. Drug Discovery*, *13*(10), 759–780. <https://doi.org/10.1038/nrd4278>
- Sahin, U [Ugur], Oehm, P., Derhovanessian, E., Jabulowsky, R. A., Vormehr, M., Gold, M., Maurus, D., Schwarck-Kokarakis, D., Kuhn, A. N., Omokoko, T., Kranz, L. M., Diken, M [Mustafa], Kreiter, S [Sebastian], Haas, H., Attig, S., Rae, R., Cuk, K., Kemmer-Brück, A., Breitkreuz, A., . . . Türeci, Ö [Özlem] (2020). An RNA vaccine drives immunity in checkpoint-inhibitor-treated melanoma. *Nature*, *585*(7823), 107–112. <https://doi.org/10.1038/s41586-020-2537-9>

- Salahpour Anarjan, F. (2019). Active targeting drug delivery nanocarriers: Ligands. *Nano-Structures & Nano-Objects*, 19, 100370. <https://doi.org/10.1016/j.nanoso.2019.100370>
- Sallusto, F., Cella, M., Danieli, C., & Lanzavecchia, A. (1995). Dendritic cells use macropinocytosis and the mannose receptor to concentrate macromolecules in the major histocompatibility complex class II compartment: Downregulation by cytokines and bacterial products. *The Journal of Experimental Medicine*, 182(2), 389–400. <https://doi.org/10.1084/jem.182.2.389>
- Saneja, A., Kumar, R., Mintoo, M. J., Dubey, R. D., Sangwan, P. L., Mondhe, D. M., Panda, A. K., & Gupta, P. N. (2019). Gemcitabine and betulinic acid co-encapsulated PLGA-PEG polymer nanoparticles for improved efficacy of cancer chemotherapy. *Materials Science & Engineering. C, Materials for Biological Applications*, 98, 764–771. <https://doi.org/10.1016/j.msec.2019.01.026>
- Sanghvi, Y. S. (2011). A status update of modified oligonucleotides for chemotherapeutics applications. *Current Protocols in Nucleic Acid Chemistry*, Chapter 4, Unit 4.1.1-22. <https://doi.org/10.1002/0471142700.nc0401s46>
- Sarfraz, M., Afzal, A., Yang, T [Tan], Gai, Y., Raza, S. M., Khan, M. W., Cheng, Y., Ma, X., & Xiang, G. (2018). Development of Dual Drug Loaded Nanosized Liposomal Formulation by A Reengineered Ethanolic Injection Method and Its Pre-Clinical Pharmacokinetic Studies. *Pharmaceutics*, 10(3). <https://doi.org/10.3390/pharmaceutics10030151>
- Sato, J., Doi, T., Kanno, T., Wako, Y., Tsuchitani, M., & Narama, I. (2012). Histopathology of incidental findings in cynomolgus monkeys (*Macaca fascicularis*) used in toxicity studies. *Journal of Toxicologic Pathology*, 25(1), 63–101. <https://doi.org/10.1293/tox.25.63>
- Saulle, E., Spinello, I., Quaranta, M. T., Pasquini, L., Pelosi, E., Iorio, E., Castelli, G., Chirico, M., Pisanu, M. E., Ottone, T., Voso, M. T., Testa, U., & Labbaye, C. (2020). Targeting Lactate Metabolism by Inhibiting MCT1 or MCT4 Impairs Leukemic Cell Proliferation, Induces Two Different Related Death-Pathways and Increases Chemotherapeutic Sensitivity of Acute Myeloid Leukemia Cells. *Frontiers in Oncology*, 10, 621458. <https://doi.org/10.3389/fonc.2020.621458>

- Schäfer, M. E. A., Keller, F., Schumacher, J., Haas, H., Vascotto, F., Sahin, U [Ugur], Hafner, M., & Rudolf, R. (2022). 3d Melanoma Cocultures as Improved Models for Nanoparticle-Mediated Delivery of RNA to Tumors. *Cells*, *11*(6), 1026. <https://doi.org/10.3390/cells11061026>
- Schäfer, M. E. A., Klicks, J., Hafner, M., & Rudolf, R. (2021). Preparation, Drug Treatment, and Immunohistological Analysis of Tri-Culture Spheroid 3D Melanoma-Like Models. *Methods in Molecular Biology (Clifton, N.J.)*, *2265*, 173–183. https://doi.org/10.1007/978-1-0716-1205-7_13
- Schlitzer, A., McGovern, N., & Ginhoux, F. (2015). Dendritic cells and monocyte-derived cells: Two complementary and integrated functional systems. *Seminars in Cell & Developmental Biology*, *41*, 9–22. <https://doi.org/10.1016/j.semcd.2015.03.011>
- Sedighi, M., Sieber, S., Rahimi, F., Shahbazi, M.-A., Rezayan, A. H., Huwyler, J., & Witzigmann, D. (2019). Rapid optimization of liposome characteristics using a combined microfluidics and design-of-experiment approach. *Drug Delivery and Translational Research*, *9*(1), 404–413. <https://doi.org/10.1007/s13346-018-0587-4>
- Seo, J., Choe, M., & Kim, S.-Y. (2016). Clearing and Labeling Techniques for Large-Scale Biological Tissues. *Molecules and Cells*, *39*(6), 439–446. <https://doi.org/10.14348/molcells.2016.0088>
- Seth, P. P., Tanowitz, M., & Bennett, C. F. (2019). Selective tissue targeting of synthetic nucleic acid drugs. *The Journal of Clinical Investigation*, *129*(3), 915–925. <https://doi.org/10.1172/JCI125228>
- Sherje, A. P., Jadhav, M., Dravyakar, B. R., & Kadam, D. (2018). Dendrimers: A versatile nanocarrier for drug delivery and targeting. *International Journal of Pharmaceutics*, *548*(1), 707–720. <https://doi.org/10.1016/j.ijpharm.2018.07.030>
- Shukla, S., Sumaria, C. S., & Pradeepkumar, P. I. (2010). Exploring chemical modifications for siRNA therapeutics: A structural and functional outlook. *ChemMedChem*, *5*(3), 328–349. <https://doi.org/10.1002/cmdc.200900444>
- Sichien, D., Lambrecht, B. N., Guilliams, M., & Scott, C. L. (2017). Development of conventional dendritic cells: From common bone marrow progenitors to multiple

- subsets in peripheral tissues. *Mucosal Immunology*, 10(4), 831–844. <https://doi.org/10.1038/mi.2017.8>
- Siedentopf, H., & Zsigmondy, R. (1902). Über Sichtbarmachung und Größenbestimmung ultramikroskopischer Teilchen, mit besonderer Anwendung auf Goldrubingläser. *Annalen Der Physik*, 315(1), 1–39. <https://doi.org/10.1002/andp.19023150102>
- Silvestri, L., Costantini, I., Sacconi, L., & Pavone, F. S. (2016). Clearing of fixed tissue: A review from a microscopist's perspective. *Journal of Biomedical Optics*, 21(8), 81205. <https://doi.org/10.1117/1.JBO.21.8.081205>
- Soe, Z. C., Kwon, J. B., Thapa, R. K., Ou, W., Nguyen, H. T., Gautam, M., Oh, K. T., Choi, H.-G., Ku, S. K., Yong, C. S., & Kim, J. O. (2019). Transferrin-Conjugated Polymeric Nanoparticle for Receptor-Mediated Delivery of Doxorubicin in Doxorubicin-Resistant Breast Cancer Cells. *Pharmaceutics*, 11(2). <https://doi.org/10.3390/pharmaceutics11020063>
- Stein, C. A., & Castanotto, D. (2017). Fda-Approved Oligonucleotide Therapies in 2017. *Molecular Therapy*, 25(5), 1069–1075. <https://doi.org/10.1016/j.ymthe.2017.03.023>
- Stelzer, E. H., & Lindek, S. (1994). Fundamental reduction of the observation volume in far-field light microscopy by detection orthogonal to the illumination axis: Confocal theta microscopy. *Optics Communications*, 111(5-6), 536–547. [https://doi.org/10.1016/0030-4018\(94\)90533-9](https://doi.org/10.1016/0030-4018(94)90533-9)
- Susaki, E. A., Tainaka, K., Perrin, D., Yukinaga, H., Kuno, A., & Ueda, H. R. (2015). Advanced CUBIC protocols for whole-brain and whole-body clearing and imaging. *Nature Protocols*, 10(11), 1709–1727. <https://doi.org/10.1038/nprot.2015.085>
- Sykes, E. A., Chen, J., Zheng, G., & Chan, W. C. W. (2014). Investigating the impact of nanoparticle size on active and passive tumor targeting efficiency. *ACS Nano*, 8(6), 5696–5706. <https://doi.org/10.1021/nn500299p>
- Taina-González, L., & La Fuente, M. de (2022). The Potential of Nanomedicine to Unlock the Limitless Applications of mRNA. *Pharmaceutics*, 14(2), 460. <https://doi.org/10.3390/pharmaceutics14020460>

- Tainaka, K., Kubota, S. I., Suyama, T. Q., Susaki, E. A., Perrin, D., Ukai-Tadenuma, M., Ukai, H., & Ueda, H. R. (2014). Whole-body imaging with single-cell resolution by tissue decolorization. *Cell*, *159*(4), 911–924. <https://doi.org/10.1016/j.cell.2014.10.034>
- Tainaka, K., Kuno, A., Kubota, S. I., Murakami, T., & Ueda, H. R. (2016). Chemical Principles in Tissue Clearing and Staining Protocols for Whole-Body Cell Profiling. *Annual Review of Cell and Developmental Biology*, *32*, 713–741. <https://doi.org/10.1146/annurev-cellbio-111315-125001>
- Tainaka, K., Murakami, T. C., Susaki, E. A., Shimizu, C., Saito, R., Takahashi, K., Hayashi-Takagi, A., Sekiya, H., Arima, Y., Nojima, S., Ikemura, M., Ushiku, T., Shimizu, Y., Murakami, M., Tanaka, K. F., Iino, M., Kasai, H., Sasaoka, T., Kobayashi, K., . . . Ueda, H. R. (2018). Chemical Landscape for Tissue Clearing Based on Hydrophilic Reagents. *Cell Reports*, *24*(8), 2196–2210.e9. <https://doi.org/10.1016/j.celrep.2018.07.056>
- Thess, A., Hoerr, I., Panah, B. Y., Jung, G., & Dahm, R. (2021). Historic nucleic acids isolated by Friedrich Miescher contain RNA besides DNA. *Biological Chemistry*, *402*(10), 1179–1185. <https://doi.org/10.1515/hsz-2021-0226>
- Tian, T., Yang, Z [Zhaoyang], & Li, X. (2021). Tissue clearing technique: Recent progress and biomedical applications. *Journal of Anatomy*, *238*(2), 489–507. <https://doi.org/10.1111/joa.13309>
- Toh, W. H., Louber, J., Mahmoud, I. S., Chia, J., Bass, G. T., Dower, S. K., Verhagen, A. M., & Gleeson, P. A. (2019). Fc γ Rn mediates fast recycling of endocytosed albumin and IgG from early macropinosomes in primary macrophages. *Journal of Cell Science*, *133*(5). <https://doi.org/10.1242/jcs.235416>
- Tuchin, V. V. (2006). *Optical clearing of tissues and blood*. SPIE Press. <https://doi.org/10.1117/3.637760>
- Ueda, H. R., Ertürk, A., Chung, K., Gradinaru, V., Chédotal, A., Tomancak, P., & Keller, P. J. (2020). Tissue clearing and its applications in neuroscience. *Nature Reviews Neuroscience*, *21*(2), 61–79. <https://doi.org/10.1038/s41583-019-0250-1>

- Usman, N., & Blatt, L. M. (2000). Nuclease-resistant synthetic ribozymes: Developing a new class of therapeutics. *Journal of Clinical Investigation*, *106*(10), 1197–1202. <https://doi.org/10.1172/JCI111631>
- van der Heijden, A., van Dijk, J. E., Lemmens, A. G., & Beynen, A. C. (1995). Spleen pigmentation in young C57BL mice is caused by accumulation of melanin. *Laboratory Animals*, *29*(4), 459–463. <https://doi.org/10.1258/002367795780740113>
- van der Jeught, K., Koker, S. de, Bialkowski, L., Heirman, C., Tjok Joe, P., Perche, F., Maenhout, S., Bevers, S., Broos, K., Deswarte, K., Malard, V., Hammad, H., Baril, P., Benvegna, T., Jaffrès, P.-A., Kooijmans, S. A. A., Schiffelers, R., Lienenklaus, S., Midoux, P., . . . Thielemans, K. (2018). Dendritic Cell Targeting mRNA Lipopolyplexes Combine Strong Antitumor T-Cell Immunity with Improved Inflammatory Safety. *ACS Nano*, *12*(10), 9815–9829. <https://doi.org/10.1021/acsnano.8b00966>
- van Krieken, J. H., & te Velde, J. (1988). Normal histology of the human spleen. *The American Journal of Surgical Pathology*, *12*(10), 777–785. <https://doi.org/10.1097/00000478-198810000-00007>
- van Lint, S., Heirman, C., Thielemans, K., & Breckpot, K. (2013). Mrna: From a chemical blueprint for protein production to an off-the-shelf therapeutic. *Human Vaccines & Immunotherapeutics*, *9*(2), 265–274. <https://doi.org/10.4161/hv.22661>
- Vandyck, H. H., Hillen, L. M., Bosisio, F. M., van den Oord, J., zur Hausen, A., & Winnepenninckx, V. (2021). Rethinking the biology of metastatic melanoma: A holistic approach. *Cancer Metastasis Reviews*. Advance online publication. <https://doi.org/10.1007/s10555-021-09960-8>
- Vaupel, P., & Multhoff, G. (2021). Revisiting the Warburg effect: Historical dogma versus current understanding. *The Journal of Physiology*, *599*(6), 1745–1757. <https://doi.org/10.1113/JP278810>
- Veninga, H., Borg, E. G. F., Vreeman, K., Taylor, P. R., Kalay, H., van Kooyk, Y., Kraal, G., Martinez-Pomares, L., & Haan, J. M. M. den (2015). Antigen targeting reveals splenic CD169+ macrophages as promoters of germinal

- center B-cell responses. *European Journal of Immunology*, 45(3), 747–757. <https://doi.org/10.1002/eji.201444983>
- Voie, A. H., Burns, D. H., & Spelman, F. A. (1993). Orthogonal-plane fluorescence optical sectioning: Three-dimensional imaging of macroscopic biological specimens. *Journal of Microscopy*, 170(Pt 3), 229–236. <https://doi.org/10.1111/j.1365-2818.1993.tb03346.x>
- Wan, Y., McDole, K., & Keller, P. J. (2019). Light-Sheet Microscopy and Its Potential for Understanding Developmental Processes. *Annual Review of Cell and Developmental Biology*, 35, 655–681. <https://doi.org/10.1146/annurev-cellbio-100818-125311>
- Wang, D., & Farhana, A. (2022). *StatPearls: Biochemistry, RNA Structure*.
- Weiss, K. R., Voigt, F. F., Shepherd, D. P., & Huisken, J. (2021). Tutorial: Practical considerations for tissue clearing and imaging. *Nature Protocols*, 16(6), 2732–2748. <https://doi.org/10.1038/s41596-021-00502-8>
- Weng, Y., Li, C., Yang, T [Tongren], Hu, B., Zhang, M., Guo, S., Xiao, H., Liang, X.-J., & Huang, Y. (2020). The challenge and prospect of mRNA therapeutics landscape. *Biotechnology Advances*, 40, 107534. <https://doi.org/10.1016/j.biotechadv.2020.107534>
- Wilde, L., Roche, M., Domingo-Vidal, M., Tanson, K., Philp, N., Curry, J., & Martinez-Outschoorn, U. (2017). Metabolic coupling and the Reverse Warburg Effect in cancer: Implications for novel biomarker and anticancer agent development. *Seminars in Oncology*, 44(3), 198–203. <https://doi.org/10.1053/j.seminoncol.2017.10.004>
- Williams, M. P. I., Rigon, M., Straka, T., Hörner, S. J., Thiel, M., Gretz, N., Hafner, M., Reischl, M., & Rudolf, R. (2019). A Novel Optical Tissue Clearing Protocol for Mouse Skeletal Muscle to Visualize Endplates in Their Tissue Context. *Frontiers in Cellular Neuroscience*, 13, 49. <https://doi.org/10.3389/fncel.2019.00049>
- Wolff, J. A., Malone, R. W., Williams, P., Chong, W., Acsadi, G., Jani, A., & Felgner, P. L. (1990). Direct gene transfer into mouse muscle in vivo. *Science (New York, N.Y.)*, 247(4949 Pt 1), 1465–1468. <https://doi.org/10.1126/science.1690918>

- Wood, H. (2018). Fda approves patisiran to treat hereditary transthyretin amyloidosis. *Nature Reviews. Neurology*, 14(10), 570. <https://doi.org/10.1038/s41582-018-0065-0>
- Yao, Y., Zhou, Y [Yunxiang], Liu, L., Xu, Y., Chen, Q., Wang, Y [Yali], Wu, S., Deng, Y [Yongchuan], Zhang, J., & Shao, A. (2020). Nanoparticle-Based Drug Delivery in Cancer Therapy and Its Role in Overcoming Drug Resistance. *Frontiers in Molecular Biosciences*, 7, Article 193, 193. <https://doi.org/10.3389/fmolb.2020.00193>
- Yu, T., Zhu, J., Li, D., & Zhu, D. (2021). Physical and chemical mechanisms of tissue optical clearing. *IScience*, 24(3), 102178. <https://doi.org/10.1016/j.isci.2021.102178>
- Zhang, R. X., Ahmed, T., Li, L. Y., Li, J., Abbasi, A. Z., & Wu, X. Y. (2017). Design of nanocarriers for nanoscale drug delivery to enhance cancer treatment using hybrid polymer and lipid building blocks. *Nanoscale*, 9(4), 1334–1355. <https://doi.org/10.1039/c6nr08486a>
- Zhou, L.-Y., He, Z.-Y., Xu, T., & Wei, Y.-Q. (2018). Current Advances in Small Activating RNAs for Gene Therapy: Principles, Applications and Challenges. *Current Gene Therapy*, 18(3), 134–142. <https://doi.org/10.2174/1566523218666180619155018>
- Zhou, L.-Y., Qin, Z., Zhu, Y.-H., He, Z.-Y., & Xu, T. (2019). Current RNA-based Therapeutics in Clinical Trials. *Current Gene Therapy*, 19(3), 172–196. <https://doi.org/10.2174/1566523219666190719100526>
- Zhou, Q., Zhang, L [Li], Yang, T [TieHong], & Wu, H. (2018). Stimuli-responsive polymeric micelles for drug delivery and cancer therapy. *International Journal of Nanomedicine*, 13, 2921–2942. <https://doi.org/10.2147/IJN.S158696>
- Ziller, A., Nogueira, S. S., Hühn, E., Funari, S. S., Brezesinski, G., Hartmann, H., Sahin, U [Ugur], Haas, H., & Langguth, P. (2018). Incorporation of mRNA in Lamellar Lipid Matrices for Parenteral Administration. *Molecular Pharmaceutics*, 15(2), 642–651. <https://doi.org/10.1021/acs.molpharmaceut.7b01022>

8 PUBLICATIONS

Schäfer, Maximilian E. A.; Keller, Florian; Schumacher, Jens; Haas, Heinrich; Vascotto, Fulvia; Sahin, Ugur et al. (2022): 3D Melanoma Cocultures as Improved Models for Nanoparticle-Mediated Delivery of RNA to Tumors. In: *Cells* 11 (6), S. 1026. DOI: 10.3390/cells11061026.

Schäfer, Maximilian E. A.; Klicks, Julia; Hafner, Mathias; Rudolf, Rüdiger (2021): Preparation, Drug Treatment, and Immunohistological Analysis of Tri-Culture Spheroid 3D Melanoma-Like Models. In: *Methods in molecular biology* (Clifton, N.J.) 2265, S. 173–183. DOI: 10.1007/978-1-0716-1205-7_13.

9 LEBENS LAUF

PERSONALIEN

Name und Vorname: Schäfer, Maximilian Enrico Alexander

Geburtsdatum: 01.12.1987

Geburtsort: Herrenberg

SCHULISCHER WERDEGANG

1995-2008 Goetheschule, Pforzheim

UNIVERSITÄRER WERDEGANG

10/2009-08/2013 Bachelor of Applied Life Sciences, University of Applied Sciences Kaiserslautern, Zweibrücken.

03/2013 – 08/2013 Bachelorthesis: “Study of the effect of anti-inflammatory substances on cells of the enteric nervous system”.

09/2013 – 02/2016 Master of Applied Life Sciences, University of Applied Sciences Kaiserslautern, Zweibrücken.

04/2015 – 10/2015 Masterthesis: “Characterization of the melanocortin-4 receptor (MC4R) in enteroendocrine cells”.

10 ACKNOWLEDGEMENTS

For the opportunity to write this doctoral thesis, for the support and encouragement, as well as for the many stimulating discussions, I would like to express my sincere gratitude to Prof. Dr. Mathias Hafner.

I would also like to thank Prof. Dr. Rüdiger Rudolf for his support, the valuable exchange, the access to state of the art technologies and the experiences I gained because of him.

Special thanks also go to my colleagues in the MZB lab for their support and the really nice time we had together.

In particular, I would like to thank Tatjana Straka and Patrick Williams with whom I was happy to share the lab. They always supported me and scientific discussions with them always opened up a new perspective. Alexander Geisel, Elena von Molitor, Julia Klicks and Franziska Ebeling I thank for their technical and motivational support.

Most of all, I would like to thank my family and friends who always supported me, even in the most difficult times. My parents, who have always taken an interest in my work and always strengthened my back.

My lovely companion for her understanding and support during the whole time. She was my source of peace when I needed her the most. My family has always been a safe harbour for me even in the greatest storms. Their love enabled me to manoeuvre the ship through all the shallows and always bring it back on course.